PhD dissertation

Emel Razzouk

MSC in Materials Science

Miskolc, 2026

Antal Kerpely Doctoral School of Material Science and Technology

Plasma Surface Engineering Studies of Metal Coatings

Surface Conversion Treatment on HPDC Al-Si Alloy using Anodizing and Plasma Electrolytic Oxidation

PhD dissertation

By

Emel Razzouk

Supervisors

Prof. Tamás Török

Professor Emeritus

Dr. Dániel Koncz-Horváth

senior research fellow

Head of the Doctoral School

Prof. Dr. Valéria Mertinger

Institute of Metal Production and Foundry

Faculty of Materials and Chemical Engineering

University of Miskolc, Hungary

Miskolc, 2026

Acknowledgement

I would like to express my deepest gratitude to all those who have contributed, directly or indirectly, to the successful completion of this doctoral dissertation.

First and foremost, I wish to extend my sincere and profound appreciation to my supervisors, whose guidance, expertise, and continuous encouragement were fundamental to this research. I am especially grateful to **Prof. Tamás Török** for his invaluable academic leadership, insightful discussions, and unwavering support throughout my doctoral studies. His broad scientific vision, critical thinking, and commitment to high research standards significantly shaped the direction and quality of this work.

I would also like to express my heartfelt thanks to **Dr. Daniel Koncz-Horváth** for his constant support, constructive feedback, and practical guidance during the different phases of this research. His availability, patience, and thoughtful suggestions greatly contributed to overcoming both scientific and technical challenges encountered along the way.

I am deeply thankful to **Dr. Giulio Timelli** (Department of Management and Engineering, University of Padova) for his valuable assistance in facilitating the wear tests and chemical analyses. His expertise and willingness to share knowledge played a crucial role in strengthening the experimental part of this dissertation. I would also like to sincerely thank **Dr. Raúl Arrabal** (Department of Chemical and Materials Engineering, Faculty of Chemical Sciences, Complutense University of Madrid) for his essential support in enabling the implementation of the plasma electrolytic oxidation (PEO) experiments. His scientific input and collaboration were pivotal to the success of the related investigations.

Furthermore, I gratefully acknowledge **Dr. Ádám Rácz**, Associate Professor, and **Mr. Tamás Kurusta**, Assistant Research Fellow, from the Institute of Raw Materials Preparation and Environmental Technology, for their professional support and technical expertise in executing the grinding processes required for the production of micro-sized strontium aluminate particles. Their practical knowledge and cooperation were indispensable for this part of the research.

My sincere thanks go to the Head of the Institute of Chemical Metallurgy and Foundry Engineering, **Dr. János Péter Erdélyi**, for providing an encouraging academic environment and

institutional support. I am also grateful to the doctoral school **Antal Kerpely Doctoral School of Materials Science and Technology** for the structured framework and academic opportunities offered throughout my studies. I would like to thank my colleagues for their collaboration, stimulating discussions, and friendly atmosphere, which made the research journey both productive and enjoyable.

I gratefully acknowledge the **Tempus Public Foundation** for awarding me the Stipendium Hungaricum scholarship. This financial support was essential in enabling me to pursue my doctoral studies and focus fully on my research.

To the one who taught me to give without limits and who transformed the hardships of life into a path adorned with hope and perseverance—**my father**. I dedicate to you the fruits of the love, trust, and values you instilled in me throughout the years of my life.

To the ever-watchful source of care and compassion, whose spirit nurtured mine and whose presence has been a constant source of inspiration—**my mother**. I offer this work as a reflection of your enduring influence, guidance, and unconditional love.

To **my siblings**, the other part of my soul, whose presence brings warmth and balance to my life. From you, I draw strength, motivation, and the foundation of my success.

Emel Razzouk

Declaration

During the thesis preparation, I did not use artificial intelligence services, except for grammatical and stylistic corrections.

Emel Razzouk

TABLE OF CONTENTS

LIST OF FIGURES

LIST OF TABLES

Chapter 1: Introduction

Surface treatment of Al–Si casting alloys has become a critical post-processing step, as many components cannot be directly utilized in their as-cast condition. The necessity for such treatments is determined by component function, operating environment, and desired service life. Beyond their well-known low density and recyclability advantages, Al–Si casting alloys are widely used to produce mechanical parts such as pistons and cylinder heads. In particular, Al–Si–Cu alloys are extensively utilized in high-pressure die casting (HPDC) due to the advantageous influence of silicon in improving castability. Consequently, various surface technologies, including anodizing and plasma electrolytic oxidation (PEO), have been employed to enhance the surface properties, corrosion resistance, and wear resistance of cast Al-Si alloys.

Traditional anodizing, hard anodizing, and plasma electrolytic oxidation (PEO) have attracted significant attention among the available surface treatments. Aluminum anodizing is an electrochemical technique in which an applied current promotes the formation of an aluminum oxide layer on the aluminum surface. This oxide layer develops through the reaction between the aluminum anode and the electrolyte, leading to the progressive consumption of the aluminum substrate. Consequently, the growth of the anodic layer is strongly influenced by the microstructural characteristics of the substrate [1,2]. During the anodizing process, aluminum is the primary component that undergoes oxidation. Generally, all aluminum alloys can be treated to form a surface oxide layer through anodizing. The process efficiency is significantly affected by the presence of alloying elements, with higher concentrations often hindering oxide growth. Notably, cast aluminum alloys typically pose greater challenges to anodization than wrought alloys [2–4].

The mechanism of oxide formation in hard anodizing (HA) remains fundamentally the same as in conventional anodizing. The distinction lies in the processing parameters: HA typically employs higher current densities, elevated acid concentrations, and lower electrolyte temperatures. These conditions facilitate the development of a thicker and harder anodic layer [2].

PEO or micro arc oxidation (MAO) is an effective wear resistance improvement technique [5,6] which is derived from conventional anodizing but enhanced by spark discharge events when

the applied voltage exceeds the critical value of the insulator oxide film. It can generate thicker ceramic coatings with excellent properties, such as high hardness, good wear and corrosion properties, and excellent bonding strength with the substrate [7–9]. The process has significantly improved surface oxidation treatment of Mg, Al, and Ti alloys, replacing traditional acid-based anodizing processes and/or conversion treatments containing hexavalent chrome and other environmentally hazardous substances in critical service applications of high added value [9].

Chapter 2: Literature review

2.1. Aluminum cast alloys

Aluminum (Al) alloys are widely used across diverse industrial sectors owing to their low density, combined with favorable mechanical, corrosion-resistant, thermal, and electrical properties. Although their absolute strength is comparatively modest, their strength-to-weight ratio exceeds that of most conventional metals [10].

The automotive industry is the leading user of aluminum castings. The demand for aluminum parts in vehicles keeps growing, mainly replacing traditional iron castings. Although more expensive than ferrous alternatives, aluminum castings remain highly desirable due to the persistent industry requirement for vehicle lightweighting and enhanced fuel efficiency. This demand has driven the shift from ferrous to aluminum parts. In vehicles, aluminum castings are widely used in engine blocks, cylinder heads, pistons, rocker covers, intake manifolds, differential housings, steering systems, structural brackets, wheels, and many other components [11].

The properties of aluminum alloys can be customized by adding different elements, which affect the alloy's behavior through various mechanisms impacting its microstructure and performance. In cast aluminum alloys, the alloying elements can be divided into three categories depending on the purpose of presenting the elements in the alloy: basic elements, secondary additions, and impurities [12].

The basic elements are responsible for enhancing castability and the overall mechanical and physical behavior of the alloy, so that these elements are present in higher amounts among the three main categories. Silicon is the most significant element in improving fluidity during casting and the strength of the alloy [13,14]. The presence of magnesium enhances the strength of the alloy through precipitation hardening and corrosion resistance. However, Mg promotes Fe-rich intermetallic formation that may cause alloy embrittlement [15]. Increasing the hardness and tensile strength of the cast Al alloy can be achieved by adding a certain amount of copper [16–18], while zinc is commonly applied in high-strength series to regulate strength and castability [19].

Secondary elements are usually added in smaller amounts; their role is to refine the microstructure, such as titanium and boron [12,20], modify eutectic morphologies when strontium

is added to the alloy [21], and neutralize the effects of undesirable phases. For instance, Manganese and chromium neutralize Fe-rich intermetallic compounds that would embrittle the alloy [22–25]. Rare earth elements such as lanthanum, cerium, and yttrium have been reported to improve thermal stability, high-temperature strength, and corrosion resistance [26].

Impurities are difficult to control during alloy production, especially when recycled feedstock is used. Iron (Fe), lead (Pb), antimony (Sb), and tin (Sn) are of particular concern in industry, as they often degrade the physical, mechanical, and service performance of aluminum alloys in various applications [27–29].

2.1.1. Al-Si system

Cast Al-Si alloys are widely used to produce mechanical components such as pistons and cylinder heads [30]. The dominant Al-Si foundry alloys typically contain between 5 and 25 wt% Si, along with additions of elements such as Mg, Ni, and Cu. The Al-Si binary system exhibits a eutectic reaction at approximately 12.2 wt% Si and 577 °C with limited solubility of silicon in aluminum, as depicted in Figure 1. Compositions containing less than 12.2 wt% Si are hypoeutectic, characterized by primary α-Al phase and eutectic. Hypereutectic Al-Si alloys contain above 12.2 wt% Si, and the microstructure of these alloys is characterized by primary Si and eutectic (Figure 2) [31,32]. The secondary phase, rich in Mg, Fe, Ni, and Cu, is present in Al-Si alloys as hypo- or hypereutectic depending on the chemical composition.

2.2. HPDC Al-Si alloys

The Al alloys mainly used in HPDC are Al-Si, Al-Si-Cu and Al-Mg-Si casting alloys, and the respective secondary alloys are actually attractive in the transport industry [33].

High-pressure die casting, often called die casting, involves injecting molten alloy into a mold under high pressure. The mold has precise dimensions constructed using two die halves, one fixed and the other movable [11,34]. HPDC process is the most widely used method for aluminum alloys because it offers fast production and the possibility for full automation. Castings produced by HPDC usually show excellent dimensional accuracy and high-quality surface finishes. Additionally, the technique allows the creation of thin-walled parts, while minimizing or even eliminating the need for post-casting machining, Since intricate features such as recesses, grooves, and holes can be incorporated directly during the molding process [11].

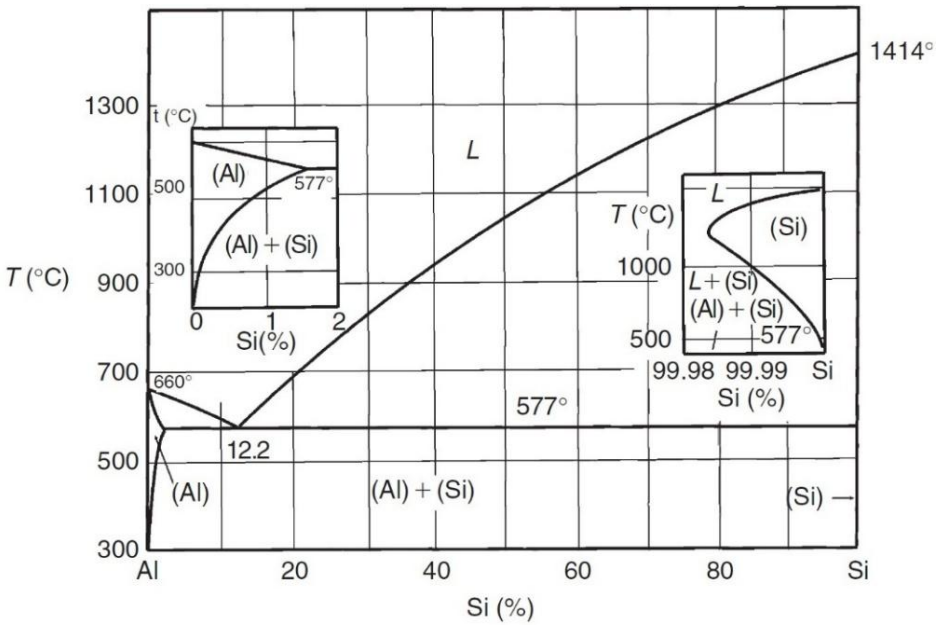

Figure 1. Binary Al-Si phase diagram [32]

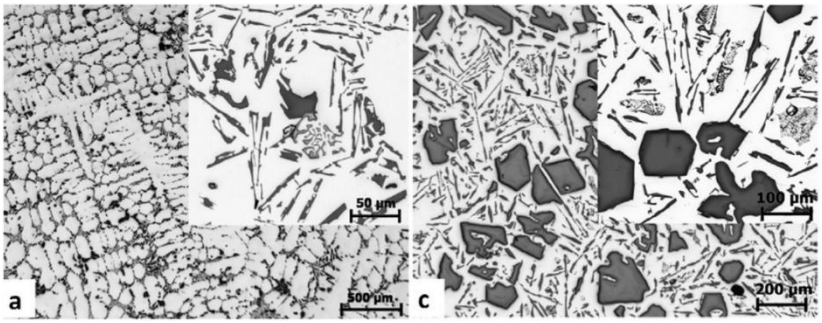

Figure 2. Optical micrographs of (a) hypoeutectic Al–7 wt.% Si alloy, and (b) hypereutectic Al–16 wt.% Si alloy [31].

HPDC has two main types: hot chamber and cold chamber. Hot chamber machines are normally used to cast alloys with relatively low melting points, such as zinc and magnesium alloys [34,35]. The molten metal is stored in an integrated furnace and injected into the die cavity through a gooseneck mechanism using a hydraulically driven plunger. This allows for fast cycle times and efficient production (Figure 3a). However, the direct contact between the pumping system and the molten metal restricts the process to low-temperature alloys, since higher melting point materials would damage the components. In contrast, cold chamber machines are designed to process alloys with higher melting points that cannot be cast in hot chamber machines because they would damage the pumping system, mostly aluminium alloy castings. The molten metal is prepared in a separate furnace and ladled into the shot chamber before being injected into the die under higher

pressures, typically ranging from 2000 to 20,000 psi (Figure 3b). The extra handling step lowers the production rate compared to hot chamber systems; the cold chamber method is essential for manufacturing components from alloys that cannot be processed in hot chamber machines because of thermal limits [34].

2.2.1. Influence of HPDC Process on Microstructure

The HPDC Al-Si alloy consists of three stages [35,36]:

(I) Low shot (slow shot): In this stage, the plunger slowly pushes the molten alloy from the shot sleeve toward the die cavity, ensuring the gate fills smoothly without turbulence. During this stage, externally solidification crystals (ESCs) begin to form [37].

(II) Fast shot: the plunger speed rapidly increases when the molten alloy reaches the gate. This ensures the cavity is filled with molten alloy before reaching the critical degree of solidification.

(III) Intensification pressure: extra pressure is applied at this stage to improve the mechanical properties and surface finish.

The microstructure of the HPDC alloys is affected by processing parameters [37,38], casting composition, and geometric complexity of the casting [39–41]. The typical microstructure of HPDC Al alloys changes from the surface into the central region [42,43] where skin formation in HPDC castings is controlled by the interplay of melt impingement, heat transfer, and applied pressure [43]. Jiao et al. [37] demonstrate the microstructure changes of HPDC AlSi10MnMg alloy as illustrated in Figure 4. At the surface region, the structure is dominated by massive fine $(\alpha\text{-Al})_{II}$ grains, accompanied by a few small globular ESCs. Moving toward about 625 from the surface, the fraction and size of ESCs increase. In the central region, larger dendritic ESCs become dominant, forming an ESC-rich zone.

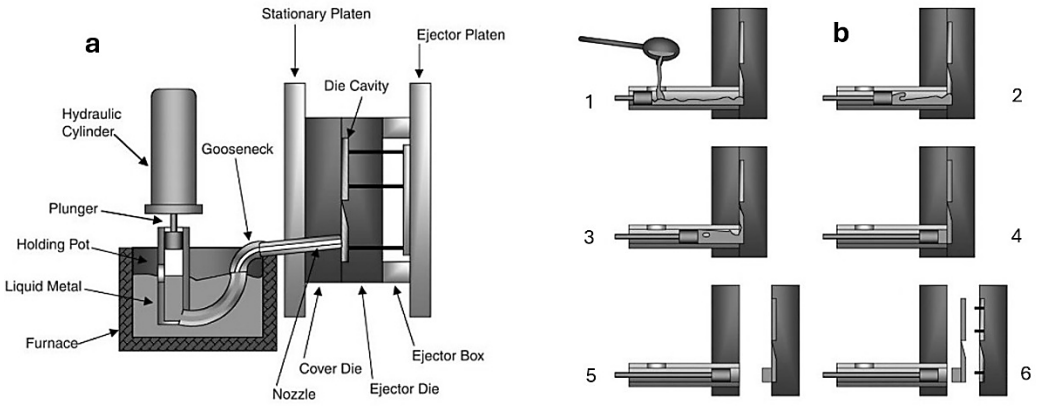

Figure 3. Graphical illustration of high-pressure die casting methods. (a) hot-chamber, and (b) cold chamber [44].

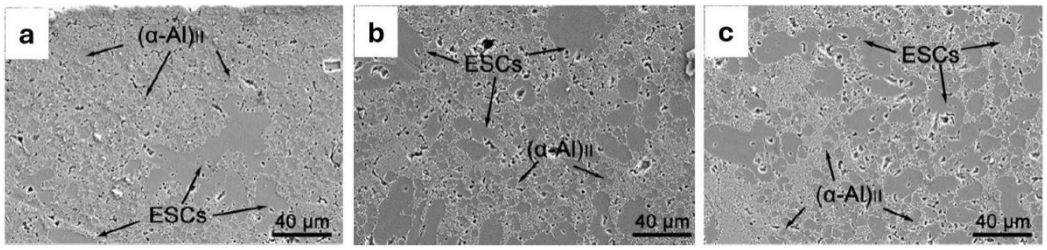

Figure 4. SEM results of HPDC AlSi10MnMg (a) surface, (b) middle (625 μm away from surface), (c) center [37].

2.3. Surface treatments of HPDC Al-Si alloys

The relatively low hardness and inadequate corrosion and abrasion resistance properties impose significant limitations on the durability of Al-Si alloy products [45,46]. Consequently, various surface technologies, including anodizing [47][10], laser remelting [48], plasma electrolytic oxidation (PEO) [49], and cathode plasma electrolytic deposition [50] have been employed to address these concerns.

2.3.1. Anodizing

The anodization of pure aluminum in aqueous solutions involves the migration of Al^{3+} cations and either O^{2-} or OH^- anions [2,51,52]. At the interface between aluminum and oxide, aluminum oxidation occurs, generating Al^{3+} cations. Simultaneously, at the oxide–solution interface, O^{2-} or OH^- species form through the removal of H^+ from H_2O [2]. The progression of the anodizing process, resulting in the formation of a porous oxide layer, can be succinctly outlined as follows:

1. Initially, aluminum cations (Al^{3+}) are generated from the aluminum substrate acting as the anode.

2. In the presence of a strong electric field, aluminum cations migrate toward the cathode, while anions in the aqueous solution (such as O^{2-}, OH^-, and electrolyte anions) move in the opposite direction. At the metal/oxide and oxide/electrolyte interfaces, the Al^{3+} cations react with the anions, forming aluminum oxide (Al_2O_3). $2Al^{3+} + 3O^{2-} = Al_2O_3$ (at the metal/oxide interface)

3. Simultaneously, at the oxide/electrolyte interface, the aluminum oxide has the potential to dissolve within the electrolyte, resulting in the creation of a porous layer. The following equation governs this chemical dissolution process: $Al_2O_3 + 6H^+ = 2Al^{3+} + 3H_2O$

Consequently, a meticulously organized hexagonal cellular structure, characterized by self-assembly, is formed. Each cell in this structure is enclosed at its base and has a central pore extending from the base to the apex. The oxide structure can be divided into two distinct regions: the barrier layer at the base and the porous layer (Figure 5). The size of the hexagonal cells and the internal pores, depends on various anodizing parameters such as the electrolyte type, current density, and anodizing time [53]. The careful selection of anodizing parameters dramatically influences the performance of an anodized component. The alloy's initial microstructure also plays a significant role in this performance. Additionally, any pre- and post-anodizing treatments can have a notable impact [2].

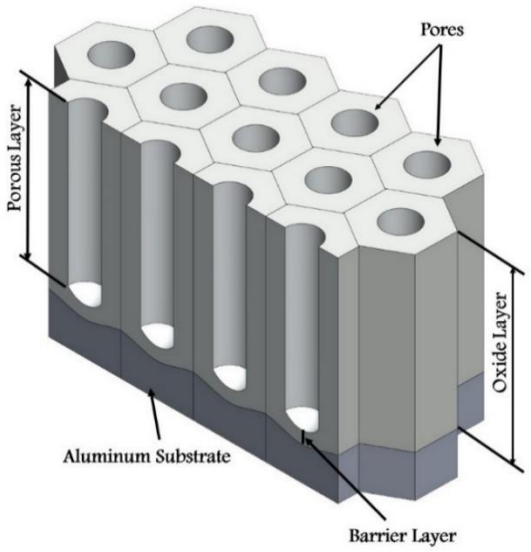

Figure 5. Ideal porous anodic oxide structure for pure aluminum [4].

Anodizing processes are categorized by their properties, making them suitable for various applications.

1. Chromic Acid Anodizing (Type I Anodizing): Also known as "chromic anodizing" or "anodizing in chromic acid," this process involves electrochemically converting aluminum in a chromic acid solution. It forms a protective oxide layer on the aluminum surface, providing corrosion protection, improved wear resistance, and a better appearance.

2. Sulfuric Acid Anodizing (Type II Anodizing): Also called "Technical Anodizing". This process involves the electrochemical conversion of aluminum in sulfuric acid. It forms a protective oxide layer, providing corrosion resistance, enhanced wear resistance, and improved aesthetics.

3. Hard Anodizing (Type III Anodizing): It is usually performed using sulfuric acid electrolytes, though other electrolytes like phosphoric acid, oxalic acid, or acid mixtures can also be employed. It creates a thicker, harder, and more durable protective oxide layer on the surface [2].

In developing Al-Si alloys, the suitability of the surface for anodization is often overlooked. The primary focus is on creating cast alloys that meet mechanical requirements like strength and fatigue while considering factors such as castability and structural integrity. Alloys are engineered to improve fluidity, minimize gas entrapment during melting, and make the casting process smoother upon solidification [54]. The mechanical properties depend heavily on casting quality, so the alloy formulation and processing methods are adjusted to reduce porosity. The mechanical properties of aluminum castings, such as strength, hardness, wear resistance, and fatigue resistance, are primarily achieved through two metallurgical mechanisms: solid-solution hardening and precipitation hardening. The evolution of microstructure, influenced by alloy composition, cooling rates, and tempering procedures, plays a crucial role in achieving these properties [2]. The microstructure of castings not only determines the component quality but also significantly impacts the quality of the resulting anodic oxide layer. Due to their higher alloy content, castings often have more complex surfaces and less free aluminum than wrought alloys. This difference results in a wider range of surface chemical potentials, creating challenges for the anodization process. The response to anodization is influenced by the composition, casting technique, and casting quality. Therefore, achieving a casting with a uniform microstructure and fine particle size becomes crucial when aiming for a specific anodized finish for a particular application [55–57].

2.3.1.1. Effect of the Alloy Second-Phase Particles

The anodization process of as-cast products can be affected by the structure and phases present in the substrate. Eutectic Si and intermetallic compounds, such as Mg_2Si, β-Al_5FeSi, α–Al(Fe, Mn, Cr)Si, and Al_2Cu phases, prove detrimental to the anodization process [33,58,59]. Also, some phases might decrease the hardness and thickness of the anodic layer [33,58]. The primary components of the as-cast microstructure in Al-Si alloys consist of primary α-Al, eutectic Si, coarse primary Si, and other harmful intermetallic phases such as needle-like β-Al_5FeSi. Furthermore, these alloys display uncontrolled and unevenly distributed porosities [60,61].

The interdendritic regions and grain boundaries may contain intermetallic compounds, depending on the alloy's chemical composition and the speed at which it solidifies [62]. The introduction of alloying elements into solid solution generally does not noticeably impact the anodizing behavior of Al alloys. Nonetheless, the creation of precipitates or intermetallic particles within the α-Al matrix or at grain boundaries may undermine the integrity of the oxide layer [63]. Intermetallic phases with redox standard potentials more positive (nobler) than the α-Al matrix exhibit slower oxidation rates and remain unanodized, appearing as residual inclusions within the oxide layer. In contrast, intermetallic compounds that are more active (with more negative potentials relative to α-A) tend to dissolve entirely during anodization, forming extra porosities within the oxide layer [2].

2.3.1.1.1. Silicon particles

During the anodization process, eutectic silicon particles may lead to the formation of several defects within the anodic layer, such as the following:

1. Formation of oxygen gas-filled voids: When the anodic oxide front reaches the silicon phase, oxidation of Si occurs through the formation of SiO_2. Because silicon is a semiconductor and SiO2 is an insulator, electron transport at the Si/SiO_2 interface becomes limited. This restriction in charge transfer can lead to local accumulation of oxygen species and the formation of oxygen gas-filled voids adjacent to Si particles [64–66], as shown in Figure 6.

2. Formation of un-anodized regions: Un-anodized regions form when the oxide layer does not completely surround the Si phase, potentially due to its morphology or reduced particle spacing. As a result, the eutectic silicon phase functions as a barrier, protecting the nearby Al matrix from

the oxide layer and thereby preserving it in an un-anodized state. Residual metallic Al phases are primarily observed under or among large, interconnected Si eutectic particles [65,66].

3. Influence on film cracking and intrinsic stress: Silicon particles can impede the volumetric expansion of the oxidizing matrix, causing the development of internal stress in localized areas and cracks forming within the film [65,67].

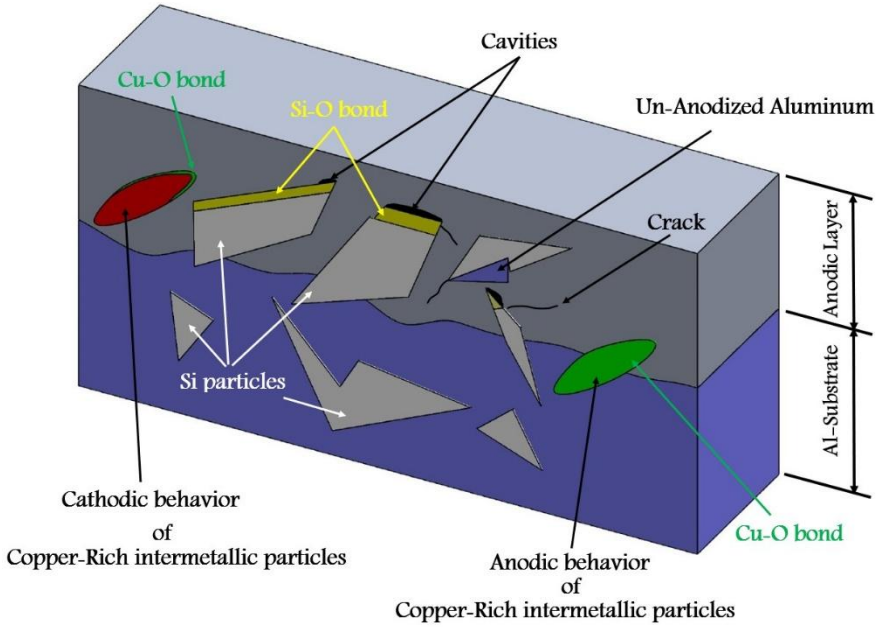

Figure 6. Sketch showing the emergence of major defects, denoted by arrows, during forming the anodic layer for Al-Si alloy *[4]*.

Aluminum in the eutectic phase is reported to exhibit primarily the same crystallographic characteristics as the primary α-Al dendrites found in unmodified alloys [68]. Heterogeneous nucleation is the primary method for grain refinement, where grains nucleate on foreign nuclei sites and grow slowly within the melt. Effective grain refiners, such as $TiAl_3$ and TiB_2, must have lattice structures that are perfectly coherent with the aluminum matrix to be effective. Conversely, particles with poor lattice matching have minimal impact on enhancing grain nucleation, leading to an unrefined grain structure [69]. Additives in the alloy can improve its ability to form a passive oxide layer, as demonstrated in a recent study by Shan-Liang Xu et al. [70].

Zhu et al. [65] investigated how the morphology of unmodified and Sr-modified eutectic silicon particles influences the anodizing behavior of Al-Si alloys. They analyzed different silicon content levels, ranging from 2.4 to 5.5 wt%. Silicon particles in polygonal flake shapes were observed in

the untreated alloys, creating a connected, branched network. The anodic oxide front expanded between the silicon particles during the anodizing process. However, due to the limited space between the particles, a significant portion of the aluminum matrix remained unanodized. Additionally, substantial localized intrinsic stresses were induced by the volumetric expansion of Al_2O_3, leading to the formation of cracks and cavities [64,71], as depicted in Figure 7.

Zhu et al. [3] studied the resistance of corrosion between the aluminum matrix and eutectic silicon particles. They subjected anodized AlSi7Mg0.4 samples to a corrosion test by immersing them in a 3 wt% NaCl solution for 72 h. The interaction between the aluminum and silicon phases formed a micro-galvanic cell, causing the anodic layer to corrode and form corrosion pits at the Al-Si interface. An increase in the defect content within the oxide layer was associated with a more intense galvanic corrosion underneath the oxide surface [72,73].

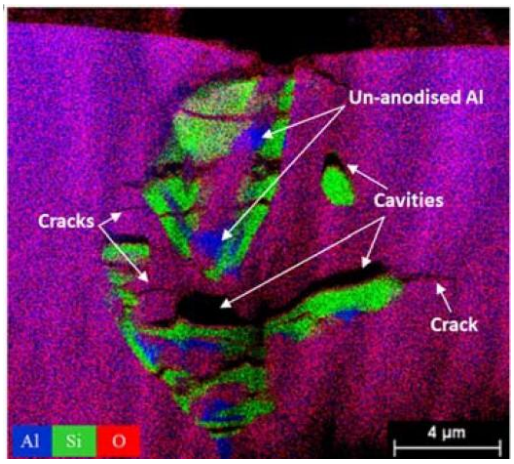

Figure 7. EDS elemental map of the anodized layer in Al–Si cast alloy *[65]*.

2.3.1.1.2. Iron-Rich Intermetallic Particles

Iron is frequently present in Al-Si alloys due to the recycling and casting processes. The presence of Fe is beneficial in preventing die soldering during high-pressure die casting (HPDC). However, Fe is an undesirable alloying element because it forms Fe-rich intermetallics like plate-like β-Al5FeSi particles, reducing ductility and corrosion resistance [61,74]. Based on the chemical composition of iron-rich intermetallic compounds, they can undergo partial or complete oxidation during the anodizing process [75]. Furthermore, they can be partially incorporated into the anodic layer, creating a wavy boundary with the unanodized aluminum substrate [76]. Specifically, the $Al_{12}(FeMn)_3Si$ and Al_6Fe phases impede the progress of the anodic layer growth due to their higher

oxidation energy [77]. While Al_3Fe particles oxidized at the same rate as the aluminum matrix and could not be entrapped in the oxide layer [76,78]. During anodizing, the partial or complete dissolution of iron-rich intermetallics creates voids and imperfections within the oxide layer [79,80]. Iron-rich intermetallic compounds form a galvanic cell with the adjacent Al-Si eutectic, thereby increasing and exacerbating pitting corrosion beneath the oxide layer [3].

2.3.1.1.3. Copper-Rich Intermetallic Particles

Copper forms an intermetallic phase with aluminum, precipitating during solidification as either blocky Al_2Cu or alternating lamellae of α-Al + Al_2Cu [81]. In the presence of iron during solidification, other copper-containing phases can form, such as β-Al_5FeSi [82]. The Al_2Cu phase may appear as blocky forms or finely scattered α-Al and Al_2Cu particles within the interdendritic areas. The anodizing behavior of copper-rich compounds is influenced by their chemical composition [83]. Fratila-Apachitei et al. [76] studied the anodizing response of the Al_2Cu phase in an AlSi10Cu3 alloy. This phase was observed as large globular compounds or irregular particles ranging from 3 to 20 μm. As the anodic front approached a particle rich in copper, the current distribution favored the copper phase because its oxidation energy was lower than that of the surrounding aluminum matrix. Consequently, this led to the development of a preferred path for oxide growth within the particle, which persisted until complete oxidation of the copper-rich compound occurred [76]. Additionally, the Cu-O bond exhibits semiconducting properties, resulting in the generation of gaseous oxygen during the oxidation reaction [64,84]. Film cracking may occur when the gas pressure is sufficiently high [64,85]. Another copper-rich phase that exhibits anodic behavior relative to the Al matrix is the S-phase (Al_2CuMg) [86]. In contrast, intermetallic phases like Al_7Cu_2Fe exhibit cathodic behavior, accelerating the oxidation of the adjacent aluminum matrix. Additionally, these compounds facilitate oxygen reduction reactions, leading to the dissolution of the neighboring aluminum phase, which is a phenomenon referred to as “trenching” [87,88]. The various behaviors of copper-rich intermetallic particles are depicted in Figure 6.

2.3.1.2. Influence of Processing Prior to the Anodizing Process

2.3.1.2.1. Casting technique

The formation of the oxide layer depends on the casting method used. Labisz et al. [89] compared the anodizing of Al-Si-based alloys produced by pressure die casting and sand casting. They found that the anodized layer is thicker for sand-cast materials than for pressure-die-cast materials. Ridder et al. [71] examined anodized aluminum surfaces produced by four manufacturing methods—extrusion, permanent mold casting, sand casting, and high-pressure die casting (HPDC). The aluminum foundry alloys used were AlSi7Mg for sand and permanent mold casting, AlSi1Mg for extrusion, and AlSi9Cu3 for high-pressure die casting, chosen for their typicality for their respective production processes. The research indicated that the uniformity of the oxide layer on the extruded sample could be attributed to the alloy's low silicon content and the specific fabrication method. In contrast, materials produced through casting processes exhibited oxide layers of non-uniform thickness on their surfaces. The HPDC sample showed the lowest average thickness and the highest variation due to the rapid cooling associated with the HPDC process. This is illustrated in Figure 8.

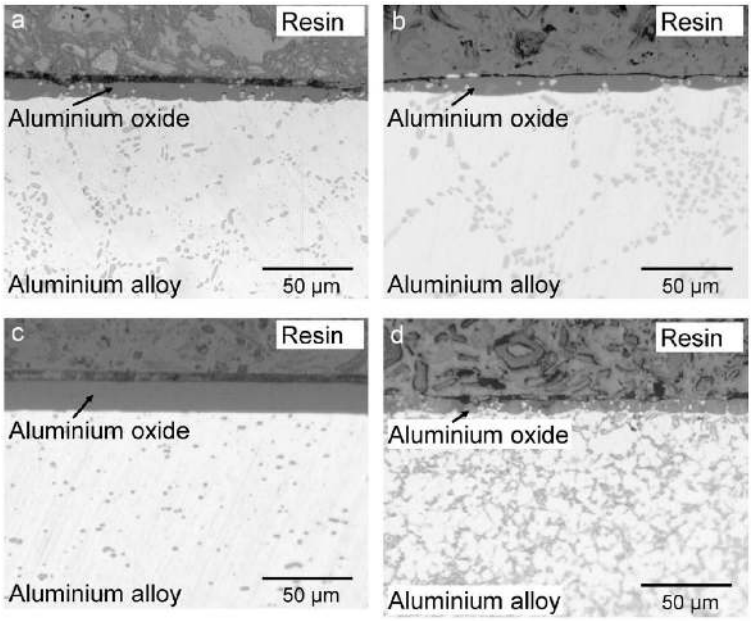

Figure 8. Optical micrographs of cross-section of anodized layer of the (a) permanent mold cast, (b) sand cast, (c) extruded, and (d) high-pressure die-cast surfaces [71].

2.3.1.2.2. Mechanical operation

The industry widely uses surface machining operations to shape products and achieve the required dimensions. The impact of machining on the anodizing process has been examined in various research studies involving hypoeutectic Al-Si alloys cast through rheocasting and die-casting methods, due to the alloy's heterogeneous microstructure and potential defects [90,91].

One advantage of the milling process was its ability to remove the oxide skin that naturally forms during high-pressure die casting (HPDC) at relatively high temperatures. When die castings are removed from the die at around 300 °C, a thicker surface oxide skin develops compared to the one that forms naturally at room temperature [92]. This oxide skin has a passivation effect that adversely impacts the thickness of the anodic oxide layer [92]. Before anodizing, chemical treatments are used to eliminate surface impurities of the casting, including oil, grime, and the oxide layer. However, alkaline cleaners might also strip away the aluminum phase from the surface, exposing the underlying intermetallic compounds [93].

Caliari et al. [90] demonstrated that milling operation before anodizing die-cast Al-Si alloys improves oxide growth. The machining step removes surface segregations and exposes areas with lower eutectic content and larger Si particles. An Al alloy substrate without elemental segregations generally shows thicker anodic oxide layers [65,92,94].

2.3.2. Plasma electrolytic oxidation (PEO)

2.3.2.1. PEO equipment setup

Figure 9 shows a typical arrangement of the PEO equipment. An electrolyser and a high-power electrical source make up the apparatus. The cathode (counter electrode) of the electrolyser is typically constructed of stainless steel. A cooling system is connected to the electrolyser to preserve the electrolyte temperature at the desired level. The stainless steel container is enclosed in a grounded case and set on an insulating base. For safety, the grounded case is joined to a ventilation setup. For PEO, a variety of power sources, including direct current (DC), pulsed DC, and alternating current (AC) sources, can be employed [6,95–100]. Samples, which act as the anode, are connected to the current supply and immersed in the electrolyte to produce coatings. After activating the electrolyte mixing and cooling system as well as the gas exhaust system, the current is applied to the workpiece in accordance with the treatment regime set [9].

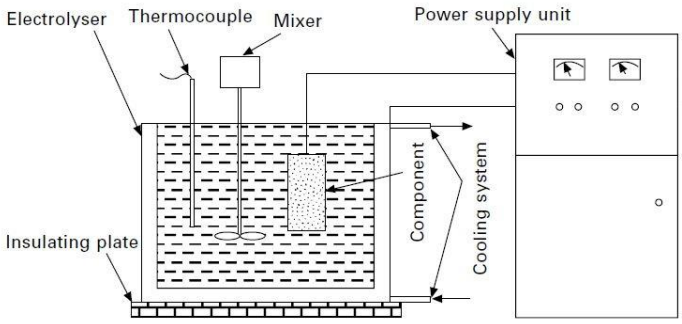

Figure 9. Typical arrangement of the equipment used for PEO technique[9].

2.3.2.2. PEO coating formation mechanism

The general mechanisms that occur during a PEO process are: (a) formation of an oxide layer on the interface between the metal and electrolyte, (b) increase in potential difference across two sides of the dielectric oxide layer, and (c) dielectric oxide layer breakdown [101]. Figure 10 shows the evolution of the coating layer.

The micro-discharge coating formation process can be broadly categorized into three steps: First, when the breakdown voltage is reached, a large number of dispersed discharge channels are produced because of micro-regional instability. Anionic components such as PO_4^{3-} and SiO_3^{2-} enter the channels via electrophoresis when subjected to a strong electric field force. At the same time, the alloying elements in the substrate melt or diffuse into the channels due to high temperature and high pressure. Second, the oxide products solidify as the proximity electrolyte rapidly cools, thus increasing the coating thickness in the local area near the discharge channels. The reaction products deposit on the channel walls as the discharge channels cool, leading to their closure. Finally, the gases produced are forced to escape from the discharge channels, maintaining the residual blind holes with 'volcano' shapes (Figure 11). As the oxidation process continues, the above process is repeated in the relatively weak regions of the entire coating surface, promoting an overall uniform coating thickness. Figure 12 describes the events that take place during a single discharge [9].

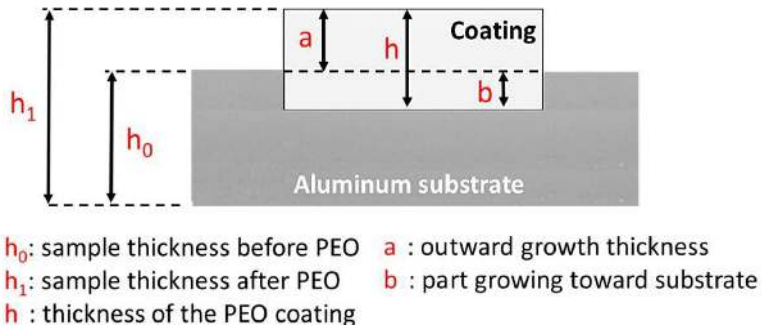

Figure 10. PEO coating formation on a 1060 Al substrate [102].

Under the rapid cooling effect of the cold proximity substrate, the generated melting oxide products near the coating–substrate interface solidify to form a fresh nanocrystalline layer with small, uniform nanograins. The nanograins in this layer are subject to gradual growth under the metallurgical process caused by repeated discharge. Nie et al.[103] also showed that the coating close to the interface exhibits a nanoscale polycrystalline microstructure with an amorphous + nanocrystalline inner layer (1.5 μm thick) and a nanocrystalline intermediate layer (50–60 nm) in the coating formed on the Al alloy. Therefore, it is believed that forming a very thin nanocrystalline layer is a universal characteristic of the PEO process, regardless of the substrate species. The nanocrystalline layer is continuously formed by 'consuming' the substrate and moves toward it; this is also regarded as the primary internal growth mechanism. [9].

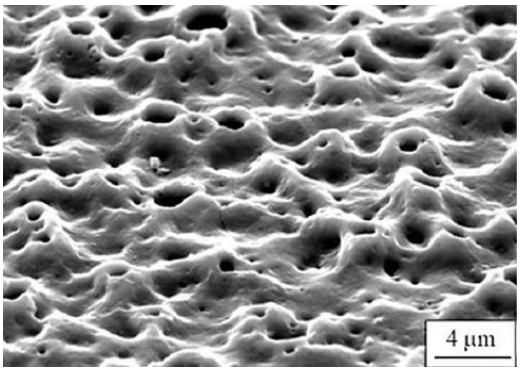

Figure 11. SEM image obtained after PEO process on a titanium sample in the presence of $K_4P_2O_7$ electrolyte shows "volcano" shaped discharge channels [104].

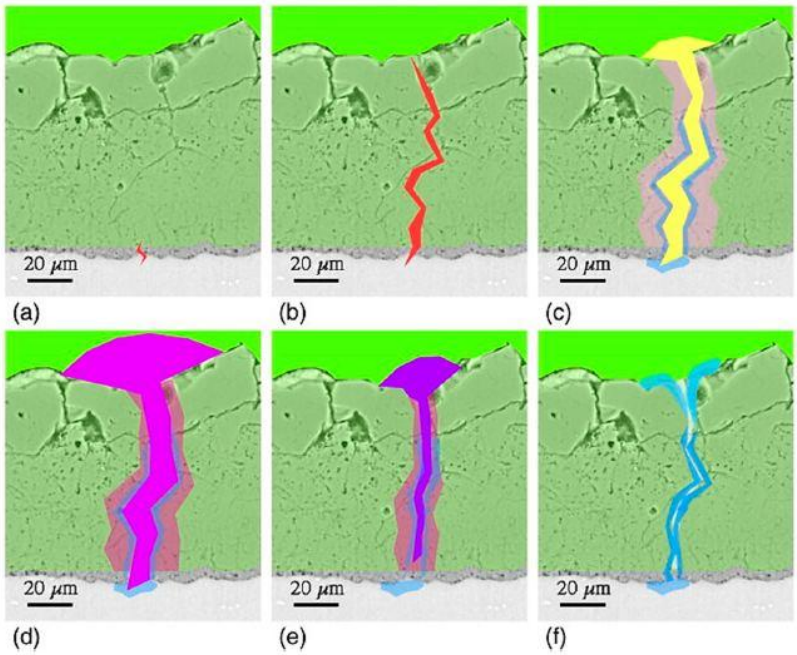

Figure 12. A description of the events that occur during a single discharge.: (a) break down at beginning, (b) formation of plasma channel through coating, (c) beginning of bubble growth and generation of oxide, (d) enlargement of bubble and heating of adjacent region, (e) decrease of bubble area due to cooling, and (f) last stage signifying quenching and removal of liquefied oxide from discharge channel *[105]*.

2.3.2.3. Parameters affecting the PEO process

Various parameters influence the coating's quality and its microstructure during the PEO process. These parameters are divided into intrinsic (e.g., electrolyte composition and substrate material) and extrinsic (e.g., process time, voltage, and current type, i.e., AC or DC). In addition to the parameters mentioned above, other factors influence the coating, such as gas bubbles formed and the development of soft plasma discharges at the later stages of the process [9,106].

2.3.2.3.1. Electrical conditions

A condition that significantly affects the PEO coating properties is the type of power supply. The different modes of electric current cause different morphologies of the PEO coating, rate of coating growth, and magnitude of porosity [107].

The power source plays a decisive role in achieving the high-quality PEO coating desired for industrial use. The development of energy sources has clearly improved PEO technology. Various sources for energy supply are used, such as DC, DC-Pulsed, AC and bipolar pulsed sources. The use of continuous current (DC) was limited before 1970, as its laboratory applications were

confined to preparing thin layers on simple parts due to difficulties in controlling the PEO process and adjusting the surface discharge. Following that, continuous pulse and alternating current were developed, enabling rapid development of PEO technology. DC-pulsed allows control of the discharge period via the work cycle, enabling more effective energy consumption. A higher current density is needed at the higher applied voltage (usually 800 V) due to polarization resulting from the formation of the double layer, which limits industrial use. Therefore, using an alternating current (AC) can overcome the polarization of the electrode and the ability to control the discharge period [9].

For aluminum anodizing in alkaline solutions, many processes of oxide formation, dissolution, and gas evolution may take place [108]. As shown in Figure 13, PEO coatings have been created using a variety of current modes. There are three distinct periods when various reactions might happen, depending on the current mode being used:

1- The period when there is no current pulse (t_{off}). The following chemical reactions can etch the aluminum substrate and release the aluminate ions AlO_2^- and $Al(OH)_4^-$ into the electrolyte, Figure 13c [109,110];

$2Al + 2H_2O + 2OH^- \rightarrow 2AlO_2^-(aq) + 3H_2$ .....(1)

$Al + 4OH^- \rightarrow Al(OH)_4^-$ (gel) ……..…(2)

Chemical dissolution can cause the alumina coating's thickness to decrease [110];

$Al_2O_3 + 2OH^- + 3H_2O \rightarrow 2Al(OH)_4^-$ (gel) $\rightarrow 2Al(OH)_3\downarrow + 2OH^-$ ……..(3)

Aluminum hydroxide can be redissolved, and aluminum oxidation might also take place. [111].

$Al(OH)_3 + OH^- \rightarrow Al(OH)_4^-$ (aq) ……(4)

$2Al + 3H_2O \rightarrow Al_2O_3 + 3H_2\uparrow$ …….(5)

2- The anodic on time (t_{on}^+) period. During this period (Figure 13c), the anode is the site of the electrochemical oxygen evolution and metal oxidation processes (Equations 6 and 7). Due to the high electric field during the process, oxygen anions (O^{2-}) move toward the anode, where they combine with the substrate to generate metal oxide. This could then result in either surface

dissolution or the production of an anodic oxide layer, depending on the substrate, electrolyte composition, and chemical activity [6,112,113].

$2H_2O \rightarrow O_2 + 4H^+ + 4e^-$ ……(6)

$2Al^{3+} + 3O^{2-} \rightarrow Al_2O_3$ ……(7)

3- The period of cathodic action on time (t_{on}^-). Cations are attracted to the negatively charged substrate at this period (Figure 13d), anions are repelled, and metal deposition could occur. Hydrogen evolution can also happen in electrolytes, which are neutral or alkaline [99,103].

$Al^{3+} + 3e^- \rightarrow Al$ ……(8)

$2H_2O + 2e^- \rightarrow H_2 + 2OH^-$ ……(9)

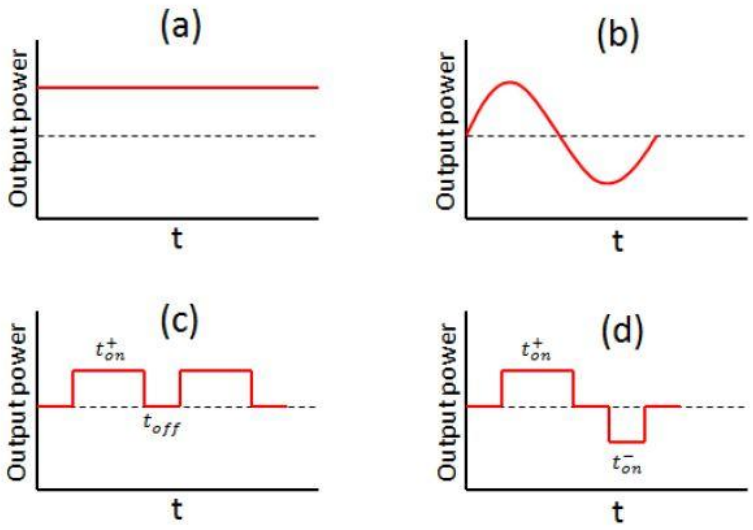

Figure 13. Various types of current modes used in PEO: (a) direct current (DC); (b) alternating current (AC); (c) unipolar pulsed current; (d) bipolar pulsed current *[99]*.

Zhang et al [114] investigated the influence of current density on the coating thickness, growth rate and growth mechanism. Three current density was applied to study the PEO coating: 2.2 A/dm^2, 4.4 A/dm^2, 8.8 A/dm^2. With increasing current density, the coating thickness increases, but the rate of growth is not linear. High current density PEO coatings have a thicker outer layer with more defects (large pores, cavities, and cracks) and a more curved Coating/Substrate (C/S) interface. All PEO coating layers have an approximately 1 µm-thick compact inner layer with many half-spherical objects measuring 0.5-1.0µm at the coating inner surface. The higher current

density makes it easier to cause type B "in-depth" discharges more than type A "surface" and type C "sub-surface" discharges. Stronger discharges (type B discharges) were produced by the high current density, resulting in a large amount of molten alumina being ejected from the C/S interface into the coating surface and rapidly solidified and re-crystallized by the electrolyte. Figure 14 shows the three types of plasma discharge that occur during the PEO process over the treated surface.

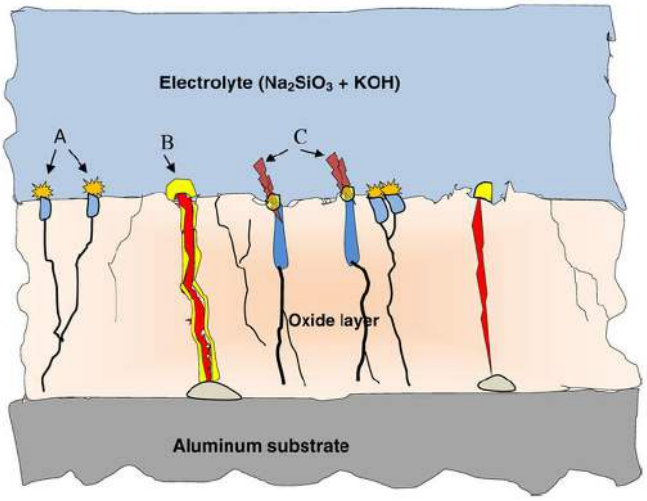

Figure 14. Schematic diagram of the discharge characteristics during the PEO of an aluminum substrate*[115]*.

The use of the pulsed DC current mode enables control of the discharge duration and pulse form, allowing for more effective use of available power by minimizing energy consumption caused by interval discharge [9,116]. In comparison to other current modes, bipolar pulsed mode has been shown to produce denser PEO coatings on aluminum and magnesium with fewer defects and a more uniform coating thickness [117,118]. Due to the enhanced characteristics of the coatings, the pulsed bipolar current mode has recently attracted significant attention.

2.3.2.3.2. Alloy composition

Alloy composition is the decisive factor in forming the oxide layer. Forming an oxide layer is difficult when the alloy contains high levels of Si or Cu, especially during traditional anodizing. This problem could be overcome by using plasma electrolytic oxidation. Silicon and copper are the main elements that cause irregular features in the PEO coating. Many researchers have investigated different Al-Si alloys to understand the behavior of the various alloys under the PEO process [9].

The presence of silicon, especially primary silicon grains, negatively affects the PEO process and the thickness of the PEO coating; the PEO coating thickness decreases with increasing Si content in the alloy. Also, selecting the power mode plays a vital role in the PEO coating's characteristics and converts SiO_2 and Al_2O_3 into Al-Si-O compounds, making the coating morphology more uniform. Pulsed bipolar voltage mode demonstrated better energy efficiency and PEO coating uniformity. The size of eutectic Si particles influences the PEO process and the properties of the coating layer. [119]. investigated the role of Si content in the PEO process of Al-Si alloys.

The method used to produce Al-Si alloy affects its microstructure, which plays an important role in the PEO process and the PEO coating. Si phase refinement through Sr modification in eutectic Al-Si alloys. It improves the efficiency of the PEO process, leading to thicker, more uniform coatings with better mechanical and anticorrosion properties [120]. The additively manufactured (AM) Al10Si1Mg alloy exhibited a more uniform coating morphology, thickness, and interface than the cast alloy; this behaviour is attributed primarily to the finer and more homogeneous Si distribution. However, the PEO coatings formed on Al10Si1Mg cast alloy exhibit higher hardness and elastic modulus, resulting in slightly lower wear rates [49].

2.3.2.3.3. Electrolyte composition and additives

The selection of the electrolyte composition significantly influences the nature of the discharges and the resulting coating. The specific compositions used are sometimes considered commercially sensitive, but in general, PEO electrolytes are alkaline, commonly containing species such as KOH and Na_2SiO_3, with pH values ranging up to about 13 [121].

To meet the prerequisite for dielectric breakdown, additives to promote strong metal passivation (such as silicates, aluminates and phosphates) are widely used as basic constituents of the electrolytes. It has been found through experiments and research that simple alkaline solutions are not suitable for commercial use due to the low growth rate of the coating and large energy consumption layer, so it is preferable to use complex electrolyte solutions for research and commercial uses.

Adding suspended particles to PEO electrolytes has become a successful approach to improve oxide coatings on lightweight metals such as aluminum [122], magnesium [123], and titanium

[124]. A large number of papers use PEO to create composite ceramic coatings on lightweight alloys [122–129], enhancing their resistance to wear and corrosion. Previous studies show that the coatings become more compact, with particles tending to locate in cavities and cracks [128–130]. Shokouhfar and Allahkaram [131] confirmed that agglomeration in micro-pores and electrophoretic effects are the most common mechanisms for incorporating nanoparticles into PEO coatings. Other studies have shown that particle size is a key factor in determining particle distribution throughout the PEO coatings, where smaller nanoparticles distribute more easily in the early stages, whereas larger particles remain near the outer surface[132].

O'Hara et al. [133] investigated the incorporation of suspended particles of Al_2O_3 (30 μm and 100 nm) and MgO (7 μm) into PEO coatings on Al and Ti substrates. The results indicate that the large Al_2O_3 particles (30 μm) were not incorporated, while MgO (7 μm) increased the mass gain of coatings, and Al_2O_3 nanoparticles had the best incorporation. Additionally, the XRD results revealed that MgO particles remain stable in the Al coating, whereas on the Ti substrate, the PEO coating contains a new phase of Mg_2TiO_4. Furthermore, Al_2O_3 particles react with Ti to form Al_2TiO_5. Lu et al. [134] demonstrated the effects of particle size on their reaction with Mg substrate to form new phases, whereby SiO_2 nanoparticles (12 nm) were reactively incorporated, consuming MgO and forming new glassy silicate-phosphate phases, while micro-sized SiO_2 particles (1-5 μm) were inertly incorporated into the PEO coating. Nadimi et al. [129] investigated the effect of incorporating SiO_2 nanoparticles into the PEO coatings on 7075 Al alloy. The study explored how varying SiO_2 concentrations affect the morphology, adhesion, corrosion, and wear resistance of PEO coatings. Lopez-Martinez et al. [128] investigated how adding α-Al_2O_3 particles to PEO processing of additively manufactured Al10SiMg alloy improved wear behavior and reduced energy consumption.

An important factor when using PEO is its substantially higher voltage and current density requirements compared to hard anodizing, which consequently increases energy consumption, as several studies have indicated [49,128]. Utilizing an anodic oxide layer as a precursor and employing appropriate current and frequency settings can help reduce energy consumption [4,118,135]. Lopez-Martinez et al. [128] quantified PEO energy consumption, reporting that particle incorporation alone reduced the energy consumption of PEO coatings by ~8% compared

with conventional PEO, while combining particle addition with a hard-anodized precursor layer achieved savings of up to ~60%.

The introduction of strontium aluminate particles into PEO coatings has mainly been studied to add long-lasting luminescence along with their aesthetic function. Strontium aluminate doped with Eu^{2+} and Dy^{3+} can be integrated into PEO coatings using two main strategies. First, by an ex-situ pore-filling technique, commercial $SrAl_2O_4:Eu^{2+},Dy^{3+}$ powders are infiltrated into the porous oxide layer formed by PEO, as reported by Auzins et al [136]. Second, by an in-situ synthesis approach, Sr, Eu, and Dy precursors are added directly into the electrolyte during the PEO process, leading to the formation of $SrAl_2O_4:Eu^{2+},Dy^{3+}$ phases that are distributed throughout the oxide layer, as demonstrated by Bite et al [137]. Nevertheless, thus far, no studies have systematically examined the behavior of undoped strontium aluminate particles suspended in the electrolyte during PEO, nor their impact on the coating structure and properties.

2.4. Knowledge gap

Despite the progress made in anodizing and Plasma Electrolytic Oxidation (PEO) techniques, several critical questions remain regarding HPDC alloys. First, the initial surface microstructure may be altered by machining and finishing processes after casting, or by inherent microstructural variations across different component regions arising from solidification rates. Therefore, a systematic investigation of these microstructural variations, in conjunction with anodizing parameters, is required. Second, although the wear resistance of anodized layers and PEO coatings has been studied, there is still limited understanding of how the initial surface condition of the HPDC alloys affects the wear behavior of hard anodized layers and PEO coatings.

In the present work, PEO was carried out in silicate-based electrolytes, one of which contained strontium aluminate particles. Under PEO conditions, strontium aluminate particles are reactively incorporated into the PEO coating, forming a new phase of strontium silicate, producing a composite ceramic coating (PEOp). Thus far, no studies have systematically examined the behavior of undoped strontium aluminate particles suspended in the electrolyte during PEO, nor their impact on the coating structure and properties.

This dissertation addresses these knowledge gaps through a comparative study on AlSi12Cu1(Fe) alloy surfaces in both as-diecast and ground conditions. The investigation focuses

on evaluating coating growth, microstructural integrity, wear behavior, and corrosion behavior for the following cases:

(i) Anodized samples (traditional anodizing) – examining the anodic layer properties and wear behavior, including the contribution of the anodic layer and the underlying substrate.

(ii) Hard anodized layers – assessing the properties of the anodic layer and its wear performance.

(iii) PEO coatings – characterizing the coating properties and wear behavior.

(iv) PEOp composite coatings – analyzing the mechanisms of composite layer formation and their associated wear behavior.

(v) Examine the corrosion behaviour of the PEO and PEOp coatings.

Chapter 3: Materials and Methods

3.1. Materials

The investigation was conducted on a die-cast AlSi12Cu1(Fe) alloy. The chemical composition of the experimental alloy measured by optical emission spectrometry is shown in Table 1. The samples were prepared from die-cast products. Two surfaces were examined to analyze the substrate properties: as-diecast and ground surfaces. The grinding process utilized silicon carbide (SiC) abrasive paper of grit size 80, targeting a 1 mm material removal.

Table 1. Chemical composition of the experimental alloy (wt.%).

Si	Fe	Cu	Mn	Mg	Zn	Cr	Ni	Ti	Al
11.6	0.738	0.818	0.247	0.104	0.308	0.0255	0.0323	0.0436	bal.

3.2. Surface treatment

3.2.1. Sample preparation

The surface preparation process includes the following steps: The samples were immersed in a moderately alkaline degreasing solution containing phosphates, borates, and potassium hydroxide, free of silicon compounds (the concentration of dissolved components is 5.4%; pH=8.7), using an ultrasonic cleaning device for 10 min at 65 ± 2 °C. The samples were then rinsed with distilled water. The subsequent pickling process involved immersing the samples in a pickling solution containing 181.4 $g \cdot L^{-1}$ sulfuric acid, 8.1 $g \cdot L^{-1}$ dissolved aluminum, and 7 $g \cdot L^{-1}$ hydrogen peroxide for 15 seconds (degreasing and pickling solution developed by Heiche Hungary Surface Technology Kft.). Finally, the samples were rinsed with distilled water.

A shielded copper wire (diameter of 1.5 mm) was used to achieve an electrical connection to the samples. A commercial resin (Lacquer 45, MacDermid plc.) was utilized to isolate the sample area, which measured 2.76 cm^2 (for hard anodizing and PEO). Figure 15 reveals this process. Thickness measurements were conducted using an eddy-current meter (ISOSCOPE FMP10 Fisher) equipped with an FTA3.3H probe, with the average derived from 10 measurements.

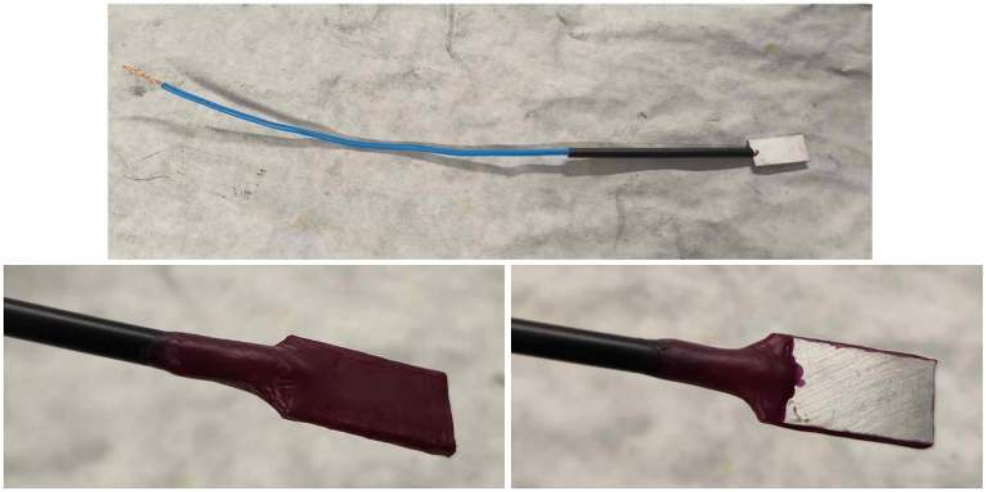

Figure 15. Preparing the sample surface for PEO treatment.

3.2.2. Traditional anodizing

Samples were anodized for 60 min in a sulfuric acid electrolyte under both potentiostatic and galvanostatic conditions. For potentiostatic anodization, voltage levels of 20 and 35 V were applied using a controlled 15-minute ramp to reach steady-state voltage. In galvanostatic anodizing, the maximum current density during the SSC phase was 1.6 $A \cdot dm^{-2}$.

Anodic layers were formed in an electrolyte solution containing 181.1 $g \cdot L^{-1}$ sulfuric acid, 10.6 $g \cdot L^{-1}$ aluminum, and 7.1 $g \cdot L^{-1}$ oxalic acid. The current was supplied by a DC power supply unit (QPX600 Dual 600 Watt). The electrolyte was continuously agitated throughout the process and kept at 18 ± 1 °C.

3.2.3. Hard anodizing

Hard anodizing layers (HA) were developed using a Delta Elektronika DC power supply, maintaining a constant current density of 25 $mA \cdot cm^{-2}$ within a 1 L double-walled glass cell. A pure aluminum cylindrical plate represented the cathode with a diameter of 9.5 cm. The electrolyte comprises a mixture of sulfuric acid (183 $g \cdot L^{-1}$, PanReac Applichem, 95-98%, CAS: 7664-93-9) and oxalic acid (7 $g \cdot L^{-1}$ of oxalic acid dihydrate $(COOH)_2 \cdot 2H_2O$, CAS: 6153-56-6). Throughout the process, the mixture was subjected to constant stirring at 300 rpm, and the temperature was controlled at 0 °C using a Huber mini-chiller Plus in conjunction with Huber SynOil fluid (M10.120.08). The treatment duration was adjusted to 10800 s to ensure sufficient oxide thickness, allowing for meaningful comparisons with PEO coatings. Following the hard anodizing treatment,

samples were rinsed with deionized water and dried with 2-isopropanol and hot air. Hard anodizing treatment was applied to two different initial surfaces: as-diecast (HA-C) and ground (HA-G).

3.2.4. Plasma electrolytic oxidation

The PEO treatment was performed in AC mode, applying a square waveform with a positive peak of +490 V and a negative peak of -110 V (50% duty cycle), utilizing a 2 kW AC power supply (EAC-S2000, ET Systems Electronic). The signals for root-mean-square (RMS) voltage and current were recorded. Table 2 presents the parameters and electrolytes employed in the PEO treatment, which included two types of electrolytes: one containing strontium aluminate particles (CAS: 12004-37-4) and the other without particles. The treatment was conducted at 400 Hz. The temperature was consistently maintained at 20 °C through the use of a closed-circuit cooling system, WK 120 LAUDA, along with a double-walled cell that has a capacity of 2 L. The counter electrode was a cylindrical mesh made of stainless steel (AISI 316L, Ø = 15 cm). Figure 16 shows the various components of the PEO apparatus. Following the PEO treatment, the samples were rinsed with deionized water and dried using 2-isopropanol and hot air. For the PEO coatings produced without particle addition, the PEO duration was fixed at 1400 s to ensure adequate coating thickness for wear resistance comparison, in addition to corrosion resistance test. 173 summarizes the details of the samples.

Using the HORIBA Laser Scattering Particle Size Distribution Analyzer LA-950, it was determined that the strontium aluminate particles exhibit a median diameter (D50) of 1.62 µm, a mean particle size of 2.40 µm, and a D90 value of 5.56 µm. The particle sizes range from approximately 0.1 µm to around 10 µm, and their specific surface area is 81,285 cm^2/cm^3.

Voltage-time and current density-time curves were integrated according to equation (1) to calculate the specific apparent energy consumption during the PEO process.

$$E = \left(\frac{\int_{t_0}^{t} V \cdot i}{S}\right) [Ws \cdot m^{-2}.\mu m^{-1}] \qquad (11)$$

Where: V is the rms voltage, i is the rms current density, t is the time of PEO process, and S is the oxide layer thickness.

Table 2. Electrical and chemical conditions for PEO treatments.

Electrolyte composition	
PEO (without particles)	10.5 g·L^{-1} $Na_2O(SiO_2)_x.xH_2O$, ≥27% SiO_2, d = 1.39 g·cm^{-3} (CAS: 13729). 2.8 g·L^{-1} KOH (CAS: 1310-58-3)
PEOp (with particles)	10.5 g·L^{-1} $Na_2O(SiO_2)_x.xH_2O$, ≥27% SiO_2, d = 1.39 g·cm^{-3} (CAS: 13729). 2.8 g·L^{-1} KOH (CAS: 1310-58-3) 10 g·L^{-1} strontium aluminate particles; Zeta potential ~ -16.4 mV
Electrical parameters	
Current density [mA·cm^{-2}]	500 mA·cm^{-2}
Frequency [Hz]	400
Voltage (V+/V-) [V]	+490/ -110
Time [s]	~700 s after the current drop
Slopes [s]	initial and final slopes, each 60 s

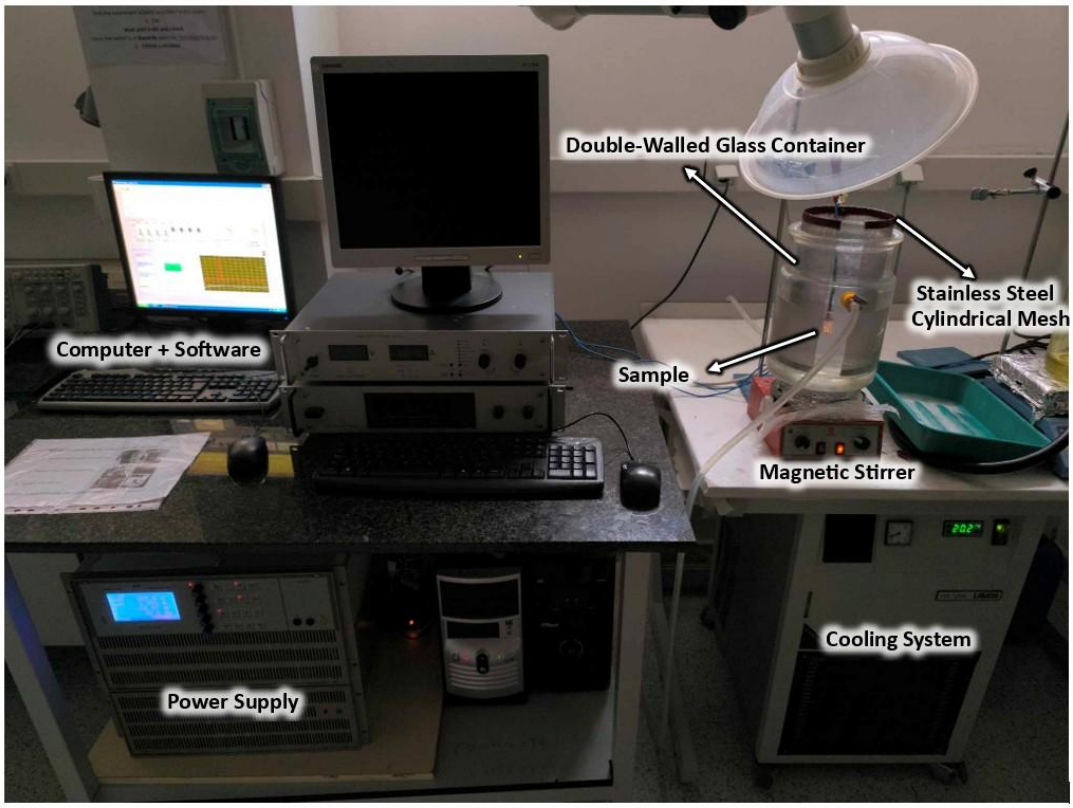

Figure 16. Components of the PEO apparatus.

Table 3. Description of test samples: surface condition, treatment type.

Sample	Surface condition before the surface treatment	Surface treatment type
PEO-C	As-Cast	PEO
PEO-G	Ground (1 mm)	PEO
PEOp-C	As-Cast	PEO (the electrolyte contains strontium aluminate particles)
PEOp-G	Ground (1 mm)	PEO (the electrolyte contains strontium aluminate particles)

3.3. Surface characteristics

3.3.1. Surface roughness and microstructure

The three-dimensional surface topography of the coatings was analyzed utilizing an optical profilometer equipped with a ×10 lens (InfiniteFocusSL, Burker, Alicona). The topographic data were analyzed utilizing the IF-Measure Suite software to extract key roughness parameters, including S_a, which represents the average height deviation of each point from the arithmetic mean of the surface, and S_{10z}, defined as the average of the five highest peaks and the five deepest valley depths. Plane view and cross-sectional micrographs of the coatings were analyzed using scanning electron microscopy with a JEOL JSM 6400 instrument equipped with Oxford Link energy dispersive X-ray microanalysis hardware with a resolution of 133 eV, and (Thermo Fisher Helios G4 PFIB SEM, Thermo Fisher, Waltham, MA, USA). High-resolution images of the microstructures were captured and processed using ImageJ, allowing the identification of various phases and features. The phase fraction was determined by identifying the distinct phases and measuring their respective areas.

3.3.2. Microhardness

Microhardness was measured in the cross-section of the oxide film and the underlying substrate using the AKASHI MVK-E3 Vickers micro-hardness tester, applying a load of 25 g for 20 s. The values presented are the averages of five measurements.

3.3.3. X-ray diffraction

Phase composition was examined by X-ray diffraction using a Philips X'Pert-MPD diffractometer (Cu Kα = 1.54056 Å) within a 2θ scanning range of 10°–90° (step size 0.04°; 2 s per step). The diffraction patterns were processed with the Panalytical X'Pert HighScore Plus software and the PDF5+ database to identify crystalline phases, and the crystallinity percentage was determined by peak integration tools within the software.

3.4. Wear test

Two dry wear tests were conducted: a unidirectional sliding wear test for traditional anodizing and a reciprocating sliding wear test for hard anodizing and PEO.

3.4.1. Unidirectional sliding wear test

Wear tests were carried out using a rotating ball-on-disc configuration at room temperature and dry conditions (Figure 17). The counter body was a 6 mm diameter alumina ball (99.8% purity, grade G16, hardness of 2100 HV, and roughness Ra of 0.025 µm). An applied load of 2 N was used, with a sliding distance of 400 m and a sliding speed of 0.1 m/s. The wear rate was calculated using the formula V / (L × N), where V is the wear volume, L is the sliding distance, and N is the applied load. The wear volume was determined by averaging the wear area along the perimeter of the circular wear track. It involved capturing profiles of 12 wear marks and calculating the average worn area.

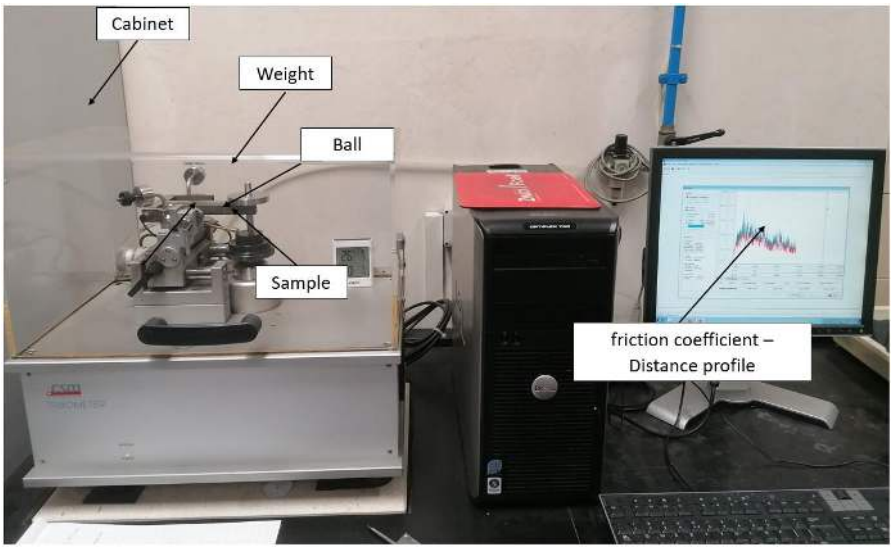

Figure 17. Unidirectional sliding pin-on-disc wear test.

The three-dimensional surface topography of the examined regions was meticulously reconstructed meticulously using a Leica DM6 M microscope equipped with the Leica Map DCM9 software, and the average surface roughness Sa was accurately measured.

SEM was used to characterize the worn surfaces of the tested samples to investigate the different wear mechanisms.

3.4.2. Reciprocating sliding wear test

The tribological properties of AlSi12Cu1(Fe) alloy, hard anodized layers, PEO coatings, and PEOp coatings were evaluated under dry conditions using an MT/60/NI ball-on-disc tester (Microtest) at room temperature (~295 K) and ~35% relative humidity (Figure 18). Tests were performed in ball-on-flat linear reciprocating mode. The tested surfaces served as the plates. The counter body was a 6-mm diameter alumina sphere with 99.8% purity, grade G28, a hardness of 2100 HV, and a roughness (Ra) of 0.05 µm. The choice of alumina as the counter body was intended to ensure that the wear test focuses on the material being tested rather than the counter material. The sliding speed during testing was 0.08 m/s over a sliding distance of 7 m with a stroke length of 10 mm. The 7 m distance was selected to maintain contact between the hard alumina ball and the coating, creating severe yet controlled conditions suitable for distinguishing the coatings' wear resistance. The experiments were performed under the normal load of 10 N. Three wear tests were performed for each specimen. The three-dimensional surface topography of the examined regions was reconstructed using an optical profilometer equipped with a ×10 lens (InfiniteFocusSL, Burker, Alicona). All profiles were first normalized to the same initial height to calculate the wear track volume. This processing was performed using the IF-Measure Suite software. The cumulative integral of profile height with respect to depth was then approximated by trapezoidal numerical integration. The resulting values were multiplied by the corresponding track length to obtain the wear track volume (mm^3). Finally, the calculated volumes were divided by the applied load to determine the total volume loss. Our investigation examined the worn surfaces of various samples using the SEM microscope (Thermo Fisher Helios G4 PFIB SEM, Thermo Fisher, Waltham, MA, USA).

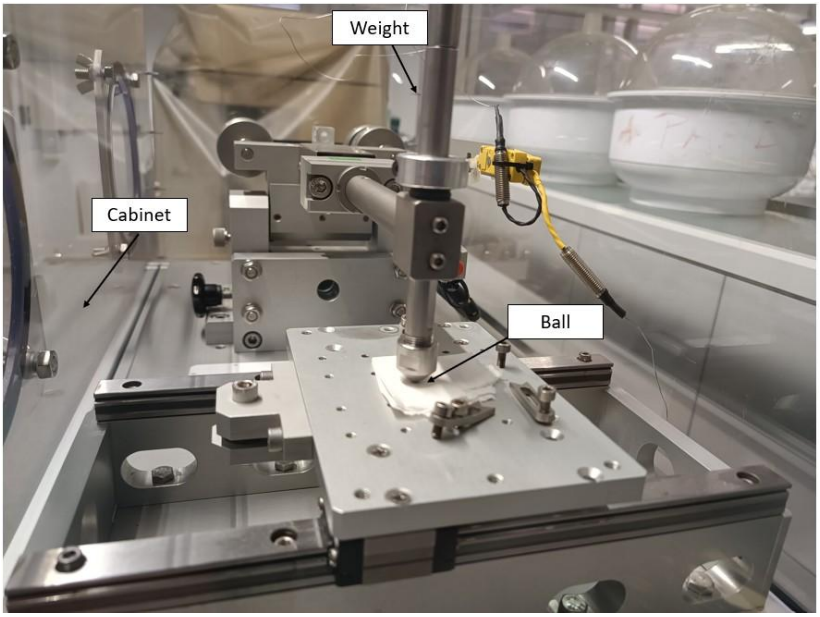

Figure 18. Reciprocating sliding pin-on-disc wear test.

3.5. Electrochemical corrosion experiments

In order to evaluate and compare the corrosion behavior of the uncoated Al–Si alloy and the different PEO coatings, electrochemical impedance spectroscopy (EIS) and potentiodynamic polarization (PDP) tests were performed using a Gamry Interface 1010E Potentiostat/Galzanostat/ZRA (Gamry Instruments, Warminster, PA, USA), and four specimens per condition were used. For these corrosion tests, an electrochemical cell of three electrodes was employed, where the reference electrode used was a commercial Ag/AgCl. The counter electrode was a graphite rod, and the working electrodes were the PEO-coated samples studied in the present work, with an exposed surface area of 1 cm^2. Figure 19 shows the electrochemical cell used for electrochemical corrosion tests. Corrosion tests were conducted in a 3.5% wt. NaCl solution, and tests were performed at ambient temperature and aerated conditions.

3.5.1. Electrochemical impedance spectroscopy (EIS)

EIS tests were performed after 1, 24, 72 h and 7 days, in order to evaluate the influence of time on the impedance. The range of frequency sweeping was between 10^5 and 0.01 Hz with 10 points/decade, and the amplitude of the sinusoidal potential signal was 10 mV with respect to the open circuit potential (OCP).

3.5.2. Potentiodynamic polarization (PDP)

PDP tests were carried out after 1 h and 7 days , once the system was stabilized, in a potential range from -0.25 V to +0.3 V (OCP vs Ag/AgCl) at a sweep rate of 0.3 mV/s. Tafel analysis was performed to obtain the potential and corrosion currents.

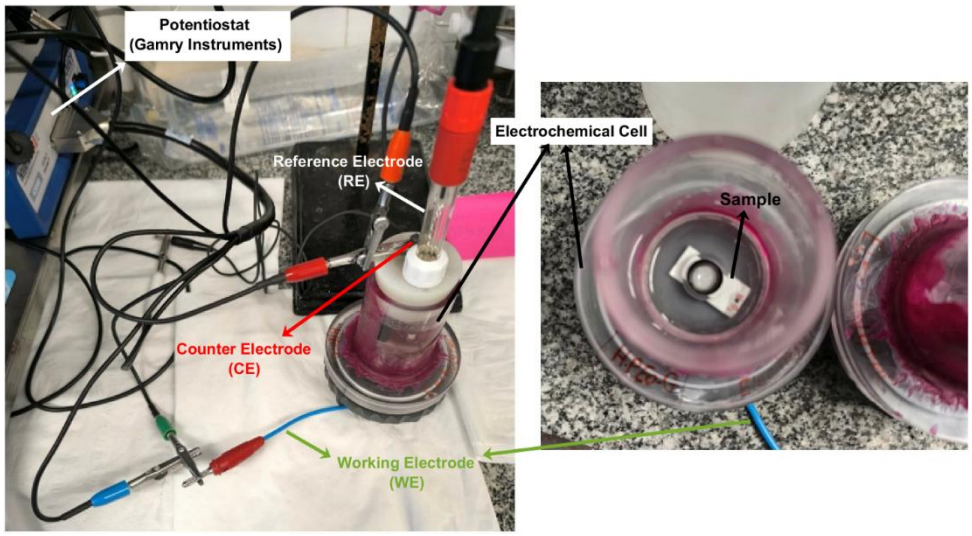

Figure 19. Electrochemical Cell Setup for EIS and PDP Corrosion Testing.

Chapter 4: Traditional anodizing- The behavior of anodized HPDC AlSi12Cu1(Fe)

4.1. Surface charge density

Surface charge density was calculated by integrating the area under the current curve in the voltage-current-time plot (Figure 20), then dividing by the sample's total surface area, as shown in Table 4.

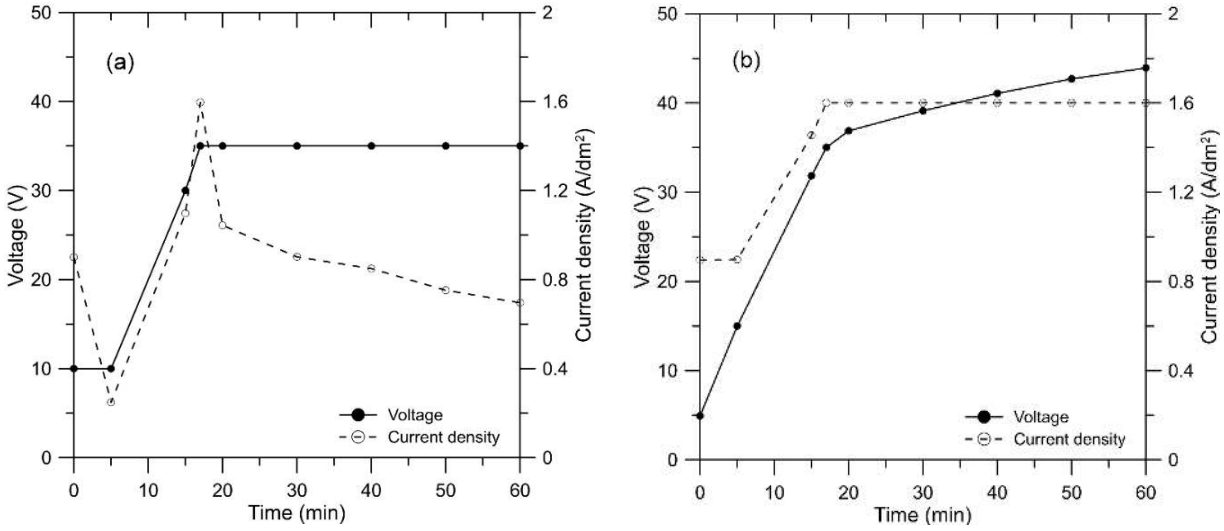

Figure 20. Voltage-current density profile of as-diecast samples as a function of anodization time at a steady-state (a) voltage of 35 V and (b) current of 1.6 A·dm^{-2}.

Table 4. Experimental parameters used during the anodizing process (SSV: steady-state voltage; SSC: steady-state current).

Anodizing process	Surface condition	Nominal current density$_{(max)}$ (A·dm^{-2})	Surface charge density (C·cm^{-2})
SSV (20V)	As-diecast	0.7	28.0
	Ground	0.9	37.0
SSV (35 V)	As-diecast	1.6	48.1
	Ground	2.8	73.8
SSC	As-diecast	1.6	89.8
	Ground	1.6	89.8

4.2. Substrate Microstructure

The as-diecast AlSi12Cu1(Fe) alloy exhibited a heterogeneous microstructure with a distinct phase distribution. The matrix consisted primarily of rosette-like α-Al grains interspersed with the eutectic Al-Si network. Because of their limited solubility in α-Al and relatively high concentrations, Fe and Cu were mainly present as secondary intermetallic compounds scattered throughout the microstructure, while Zn and Mg, owing to their higher solubility and lower levels, were dissolved in the α-Al matrix. Quantitative analysis of the surface revealed ~34 ± 1% α-Al, 61.9 ± 1.2% Al-Si eutectic, and 4.2 ± 1.2% intermetallics (Figure 21a). The α-Al grains in this region were fine and equiaxed.

After 1 mm of the surface was removed, significant microstructural variations were observed (Figure 21b). The fraction of α-Al increased to 54.0 ± 0.8%, while the eutectic component declined to 40.2 ± 0.6%, and the intermetallics rose slightly to 5.4 ± 0.5%. This shift reflects exposure to a more ductile matrix beneath the surface. In addition, the α-Al grains appeared coarser, consistent with regions that solidified under slower cooling conditions, as reduced cooling rates are known to promote grain coarsening.

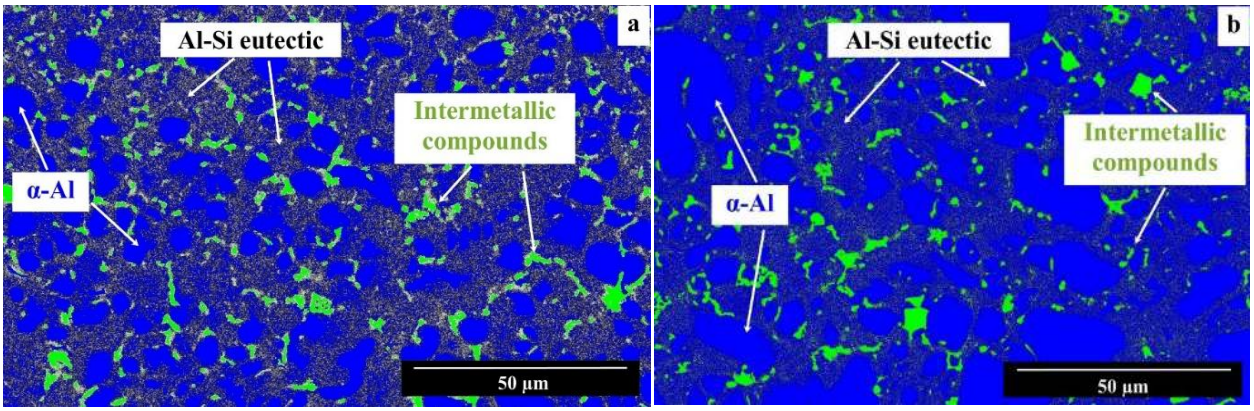

Figure 21. Typical SEM micrographs of diecast AlSi12Cu1(Fe) alloy. The images refer to (a) as-diecast and (b) 1mm ground substrates.

4.3. Surface roughness

The grinding process, which removed 1 mm of material from the surface, resulted in significant variations in surface topography. The as-diecast surface of the alloy exhibited relatively low roughness (Sa 0.926 ± 0.094 µm). This measurement reflected the minimal topographical variations present on the diecast surface (Figure 22a). In contrast, the ground sample surface

showed higher roughness (Sa 1.60 ± 0.38 µm). This increase in roughness was directly attributed to abrasive action during the grinding process, particularly from the use of SiC paper for surface preparation. The grinding process produced distinctive parallel grooves characteristic of the grinding marks, visible in Figure 22b.

After anodizing, the as-diecast surface showed a moderate increase in roughness (Sa 1.33 ± 0.63 µm). The anodized layer showed a strong correlation with the surface characteristics of the as-diecast alloy, as demonstrated in Figure 22c. After anodizing, the ground surface exhibited a higher level of roughness (Sa 1.96 ± 0.22 µm) (Figure 22d). In general, increased roughness significantly affects the wear performance of the material[138]. A more textured surface may increase friction and lead to more debris formation during wear.

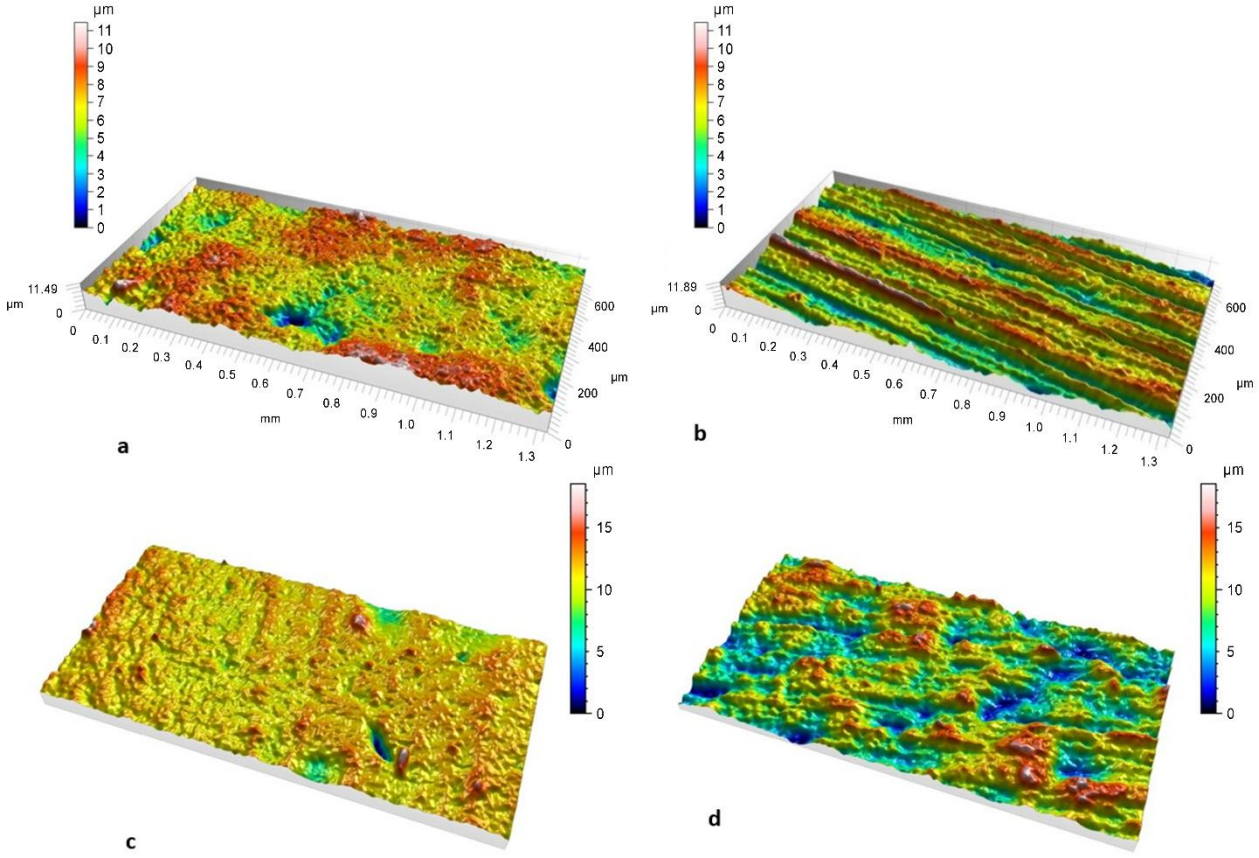

Figure 22. 3D surface topography of (a,c) as-diecast and (b,d) ground surfaces. The surface morphology is shown (a,b) before and (c,d) after anodizing. The scale is different between (a,b) and (c,d).

4.4. Microstructure of the anodic layer

The substrate's initial microstructure significantly influenced the anodic layer's microstructure and morphology. Figure 23 illustrates the different anodic layers formed under the applied modes and voltages; although the morphology of the anodic layer remained largely consistent, some variations could be attributed to microstructural differences between the as-diecast and ground substrates.

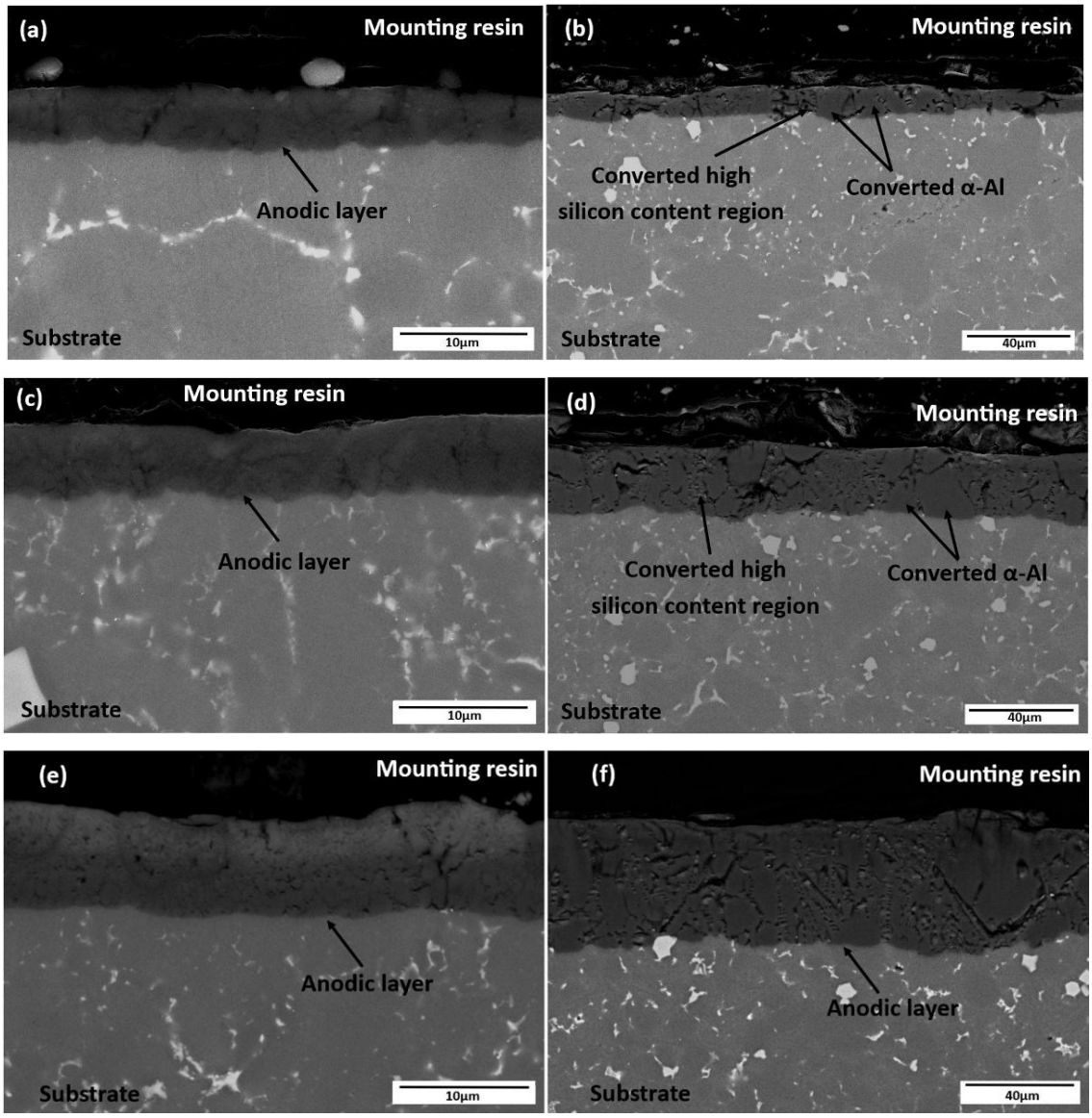

Figure 23. Microstructure of the anodized layers obtained with SSV of (a,b) 20 V and (c,d) 35 V, and with (e,f) SSC. (a,c,e) are as-diecast and (b,d,f) ground substrates.

The anodic layers showed standard features, which included anodized α-Al grains, embedded silicon particles, anodized Al-Si eutectic, and cavities. Notably, the size of the cavities in the anodized ground surface (Figure 23b,d,f) was greater than that in the anodized as-diecast surface (Figure 23a,c,d). In addition, cavities are primarily observed in the eutectic Al-Si regions. Although the number of voids remained almost constant in the different anodized as-diecast substrates, the percentage of cavities increased significantly on the anodized ground surfaces (Table 5). Among the different anodizing conditions investigated, the SSC mode resulted in the highest level of cavities in the anodic layer.

The converted α-Al grains appeared as uniform regions, while the eutectic areas with a high silicon concentration showed heterogeneous characteristics and reduced thickness compared to the converted α-Al zones.

Furthermore, the galvanostatic or potentiostatic anodizing modes yielded different anodic layer thicknesses, which appeared to be primarily correlated with the applied surface charge density.

Table 5. Area fraction of cavities within the anodic layer of as-diecast and ground surfaces processed with different anodizing conditions.

Anodizing condition	Cavity (%)	
	Anodized as-diecast substrate	Anodized ground substrate
SSV (20 V)	0.5 ± 0.2	1.1 ± 0.1
SSV (35 V)	0.3 ± 0.2	3.4 ± 0.6
SSC	0.4 ± 0.1	4.9 ± 1.5

Table 6 shows the microhardness of the anodic layer obtained under different anodizing conditions, compared with that achieved under the same testing conditions on the initial alloy substrate. The anodic layer exhibited a higher hardness than that of the AlSi12Cu1(Fe) alloy substrate. Furthermore, the anodic layer hardness appeared to be correlated with the initial surface condition prior to anodizing, with the as-diecast substrate showing higher microhardness. The initial surface and the anodizing parameters affected the structure of the anodic layer, and thus, the hardness of the anodic layer.

Table 6. Vickers microhardness of the alloy substrate and the anodic layers.

	Anodizing condition	As-diecast surface	Ground surface
Initial substrate	-	132 ± 7	123 ± 7
Anodic layer	SSV (20 V)	426 ± 73	326 ± 68
	SSV (35 V)	415 ± 65	320 ± 74
	SSC	423 ± 81	308 ± 62

4.5. Anodic layer thickness

Figure 24 shows how the thickness of the anodic layer was affected by both the anodization process parameters and the initial surface characteristics. Samples processed at steady-state current density showed the highest oxide layer thicknesses. This was in conjunction with samples anodized at a steady-state voltage, and the thinnest layers were observed at 20 V. A distinct trend emerged: grinding removed material, resulting in thicker anodizing layers. The maximum thickness 45 ± 8.3 µm was achieved in ground samples treated with current-controlled anodization. Higher standard deviation values in anodized ground substrates aligned with experimental observations, reflecting the scalloped morphology of the anodic layers.

In contrast, the limited thickness of the oxide layer formed on the as-diecast substrate was related to the presence of surface eutectic segregation, which negatively interacted with the growth of the anodic layer.

Figure 25 shows the thickness of the anodic layer as a function of the applied surface charge density. Both as-diecast and ground surfaces display an increasing trend, but the ground surfaces respond more strongly, leading to a thicker anodic layer.

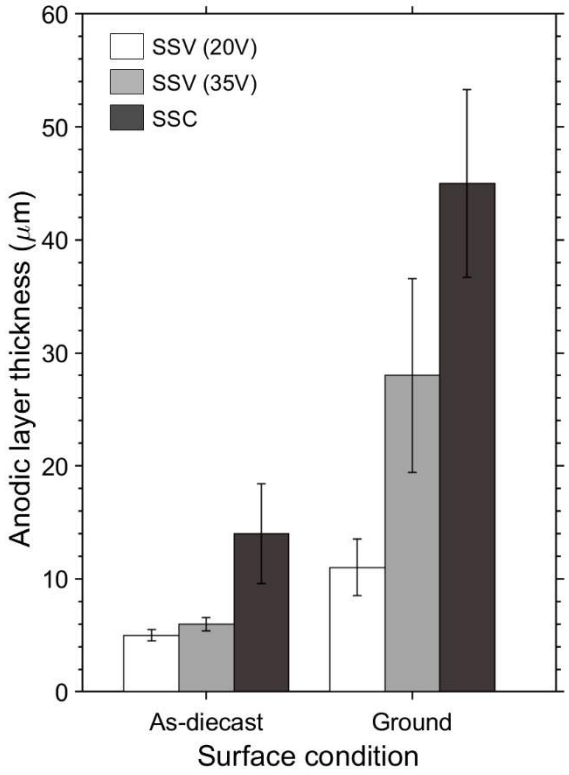

Figure 24. Variation of the thickness of the anodized layer in the different experimental configurations.

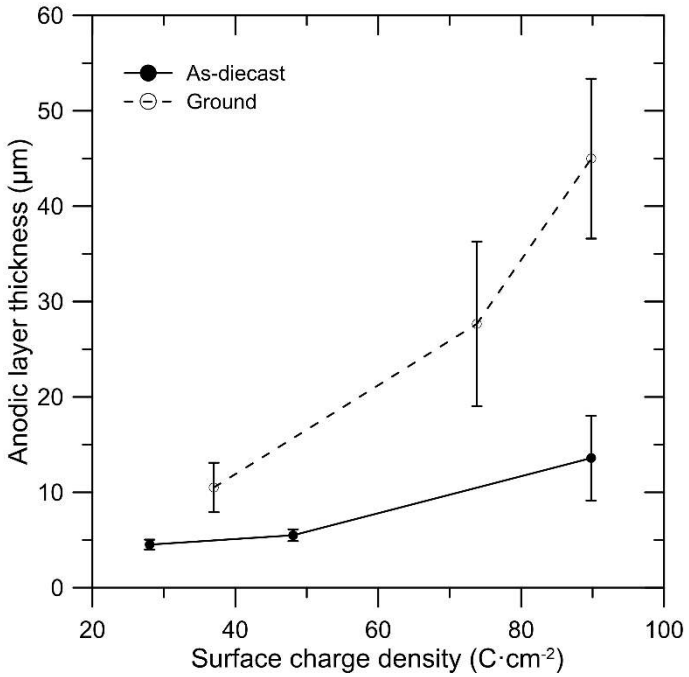

Figure 25. Anodic layer thickness of as-diecast and ground AlSi12Cu1(Fe) alloy substrates as a function of the surface charge density.

4.6. Wear rate

The analysis of the wear rate provided valuable insight into the complex relationship between the anodic layer's microstructure and the resulting material properties. This relationship revealed significant trends influenced by key factors, including the anodized layer and the substrate's initial surface condition. In a comprehensive examination of the anodic layer structure across all studied cases, notable differences in performance were identified between anodized samples originating from as-diecast surfaces and those processed from ground surfaces. Specifically, the wear rates in these two groups showed distinct patterns (Figure 26). The anodized samples from as-diecast surfaces showed a relatively consistent wear rate; however, the anodized ground samples produced under steady-state voltage showed a lower wear rate than those produced under steady-state current. For all SSV and SSC, the wear rate increases as the initial surface state changes from as-diecast to ground.

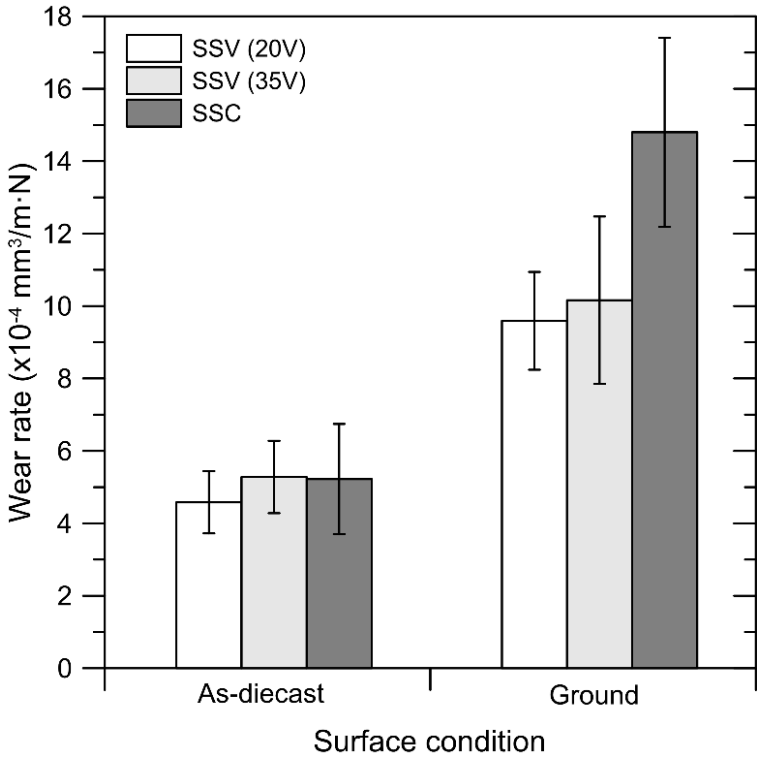

Figure 26. Variation of the wear rate on the as-diecast and ground AlSi12Cu1(Fe) alloy substrates processed with different anodizing modes as a function of the different conditions.

4.7. Discussion

The tests performed on anodized AlSi12Cu1(Fe) alloy samples revealed that several key factors affected wear behavior. These included the microstructure of the substrate, surface roughness, and the integrity and thickness of the anodic layer. To comprehensively explain the wear behavior of the anodized AlSi12Cu1(Fe) die-casting alloy, the relationships among the variables were analyzed and are discussed. Understanding the interaction among all variations is crucial to optimizing the alloy's performance and enhancing its durability in practical applications.

4.7.1. Effect of surface roughness

When studying a somewhat similar system, Scampone and Timelli [138] reported that the surface roughness of the anodized specimens affects the wear rate, a phenomenon also observed in the present work. To establish further correlations among the above-mentioned influencing parameters, the surface roughness Sa and the wear rate of anodized AlSi12Cu1(Fe) alloy samples prepared under different anodizing conditions are presented in Figure 27 as a function of anodized layer thickness. As shown in Figure 27, the ground surfaces after anodizing have higher surface roughness than the as-diecast surfaces. This increase in surface roughness correlates with an increase in wear rate; in all cases, SSV and SSC exhibit the same trend in surface roughness and wear rate, but the slope varies with anodic layer thickness, especially when the anodizing process is performed under steady-state current conditions. Although the anodized ground surfaces under SSC have surface roughness similar to or slightly lower than that under SSV, the thickness of the anodic layer increases by up to 300%, in addition to an increase in wear rate. These findings suggest that, while surface roughness contributes to a higher wear rate. These findings suggest that the effects of surface roughness on wear rate are also strongly correlated with the anodic layer microstructure.

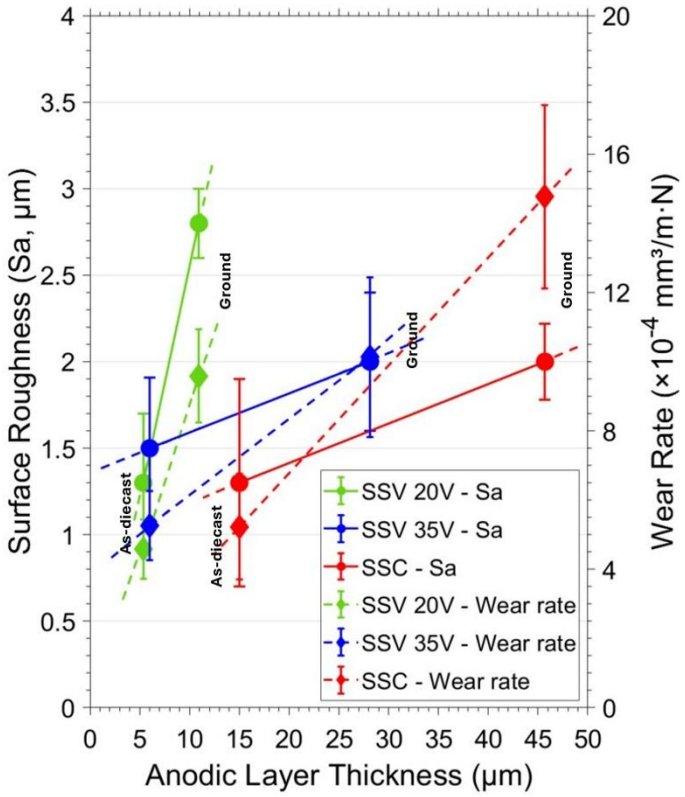

Figure 27. Correlation between the thickness of the anodic layer, the roughness of the surface area roughness (Sa), and wear rate of anodized samples.

4.7.2. Effect of substrate and anodic layer microstructure

The studied AlSi12Cu1(Fe) diecasting alloy consisted of three main structural features: α-Al phase, Al-Si eutectic and intermetallic compounds. The size and distribution of these components affect the growth of the anodic layer, as mentioned in many previous studies [58,59,139]. Silicon segregation within the substrate can create areas where the properties vary significantly [58,59]. This segregation typically appears in a surface region of up to approximately 1 mm thick, with a pronounced Al-Si eutectic concentration [140]. The concentration gradient can alter the electrochemical behavior of the surface, thereby affecting the uniformity and quality of the growing anodic oxide layer [33,140]. Unanodized Al regions may appear within the anodic layer in areas where aluminum is surrounded by oxidation-resistant Si particles [65,66]. This phenomenon results in a nonuniform anodic layer with variations in thickness.

The existence of the anodic SiO_2 film and these gas-filled voids contributes to creating regions that are characterized by high electrical resistance. This elevated resistance effectively serves as a barrier to the continued growth of the anodic layer, which slows the anodization process as the

film thickens within the α-Al regions. This variation in anodizing rates results in more cavities and defects in the anodic layer of the ground surface.

In contrast, the anodic layers formed on the diecast surfaces exhibit fewer and smaller cavities. The fine microstructural features and the even distribution of the eutectic phase on the as-diecast surfaces facilitate more uniform oxide-layer growth. Collectively, these factors undermine the integrity and protective qualities of the anodic layer. On anodized ground surfaces, both steady-state voltage and current modes result in increased anodic layer thickness and a higher percentage of cavities (Table 5) compared to the as-diecast condition. This trend indicates a correlation in which a thicker anodic layer corresponds to increased cavity formation, contributing to elevated wear rates. Aluminum oxide has various grades and allotropic forms, each with distinct physical properties [141]. The hardness of pure alumina ranges from approximately 560 to 2200 HV [142]. However, aluminum oxide produced by anodizing often exhibits lower hardness than pure aluminum oxide. Bononi et al. [143] recorded a hardness value of 370 HV for the anodic oxide layer formed on a hard anodized Al-Cu-Li wrought alloy. Additionally, Bozza et al. [144] reported that the hardness of the oxide layer, when produced under hard anodizing of AA 7075-T6 using pulse current anodizing, reached up to 420 HV. Makhlouf et al. [145] reported that silicon particles have a hardness of 1200 ± 120 HV, which is higher than that of anodized aluminum oxide. As a result, the eutectic silicon particles embedded in the anodic layer are expected to act as reinforcing elements, significantly influencing the wear behavior. The wear test setup used in this study was designed to wear down the anodic oxide layer and the underlying substrate. The anodized as-diecast surfaces showed high microhardness, reaching 426 ± 73 HV; however, the underlying substrate had lower hardness at 132 ± 7 HV. On the contrary, although the anodic layers on the ground surfaces were thicker, their hardness decreased significantly due to increased porosity, as indicated in Table 5 and Table 6. Figure 28 shows that some anodic layer's characteristics, specifically its hardness, directly affect the wear rate, whereas anodic layer thickness does not. The relationship between anodizing parameters and wear rate for this kind of inhomogeneous alloy is primarily governed by the anodic layer characteristics; a thicker and more cavitated layer leads to a higher wear rate.

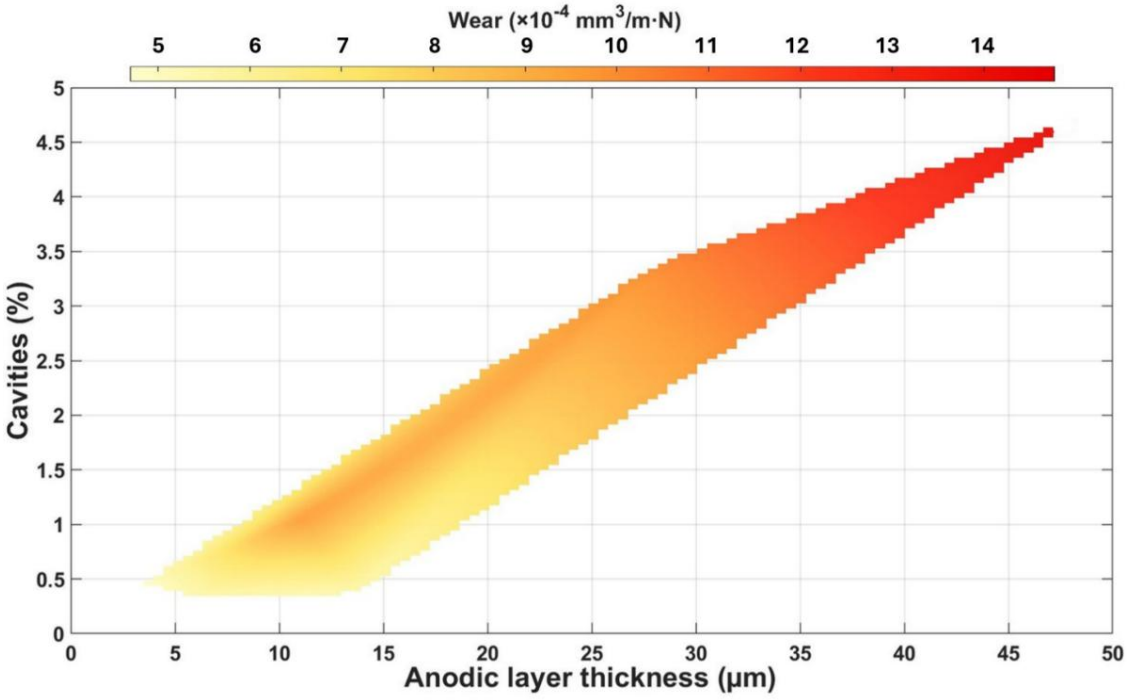

Figure 28. Correlation between cavities, wear rate, and thickness of the anodic layer for the anodized samples.

4.7.3. Wear behavior of the anodized sample

During the initial sliding stages, the anodized surfaces undergo abrasive wear accompanied by brittle fracture, leading to elevated friction coefficients, as illustrated in Figure 29. The surface roughness of the anodized layers significantly influences this early wear behavior; specifically, rougher surfaces tend to cause earlier localized oxide failures and breakdown. When the alumina ball completely removes the oxide layer, the friction coefficient drops, making the anodized as-diecast surfaces more stable in both SSV and SSC. This behavior is attributed to the microstructure of the substrate, as illustrated in Figure 29. The friction coefficient of the anodized ground surfaces reached higher values than the anodized as-diecast surfaces. This behavior was due to the greater volume loss (Figure 26), which led to an increase in the contact area between the ball and the counter body, as depicted in Figure 30. It shows the wear depth profile for anodized as-diecast and ground samples. The differences in the width and depth of the worn scar between anodized as-diecast and ground surfaces are statistically significant under SSV and SSC conditions (student's t-test, $p < 0.05$), as shown in Figure 31.

The severity of wear increased due to a three-body abrasion mechanism. This is due to the entrapment of debris between the counter body and the worn surface. Observations presented in

Figure 32 confirm the existence of ploughing marks and plastic deformation on the exposed substrate after complete removal of the anodic layer, particularly evident on anodized ground surfaces (Figure 32b,d). In contrast, the as-diecast samples (Figure 32a,c) displayed minimal debris accumulation, a result of the effective distribution of Si particles within the eutectic network, which improves their wear resistance and stabilizes the friction coefficient after anodic layer removal, as shown in Figure 10 for anodized as-diecast samples anodized under steady-state voltage or current modes.

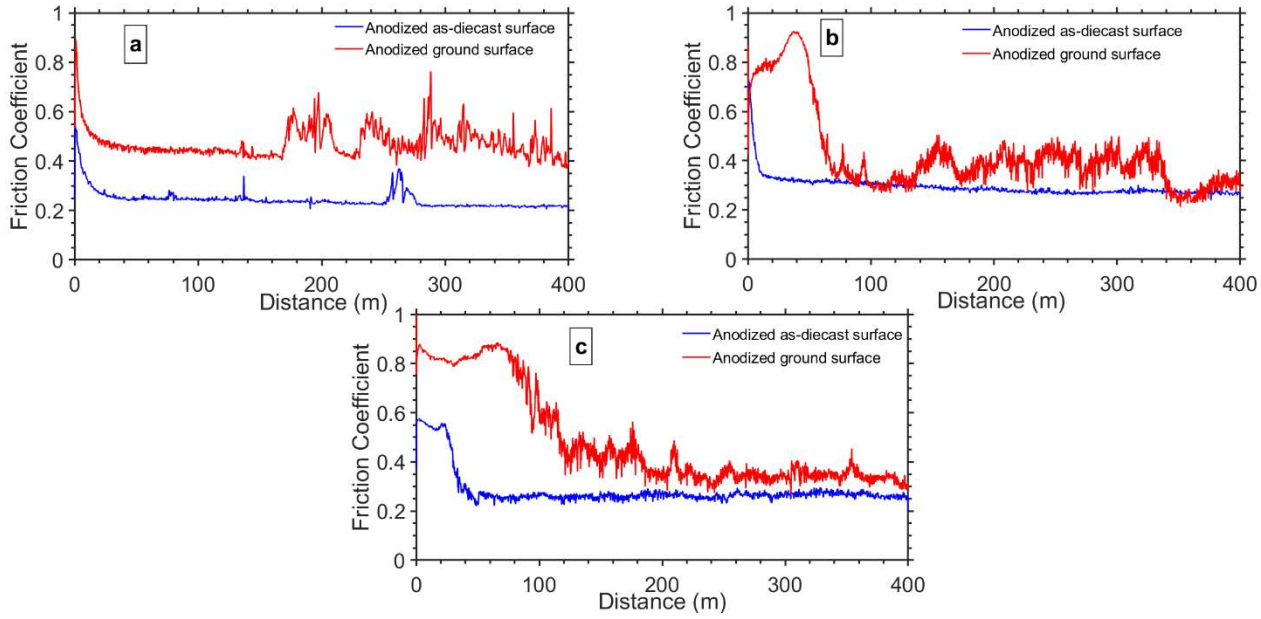

Figure 29. Friction coefficient as a function of distance for the anodized samples under (a) steady state voltage 20 V (b) steady state voltage 35 V and (c) steady state current 1.6 A·dm^{-2}.

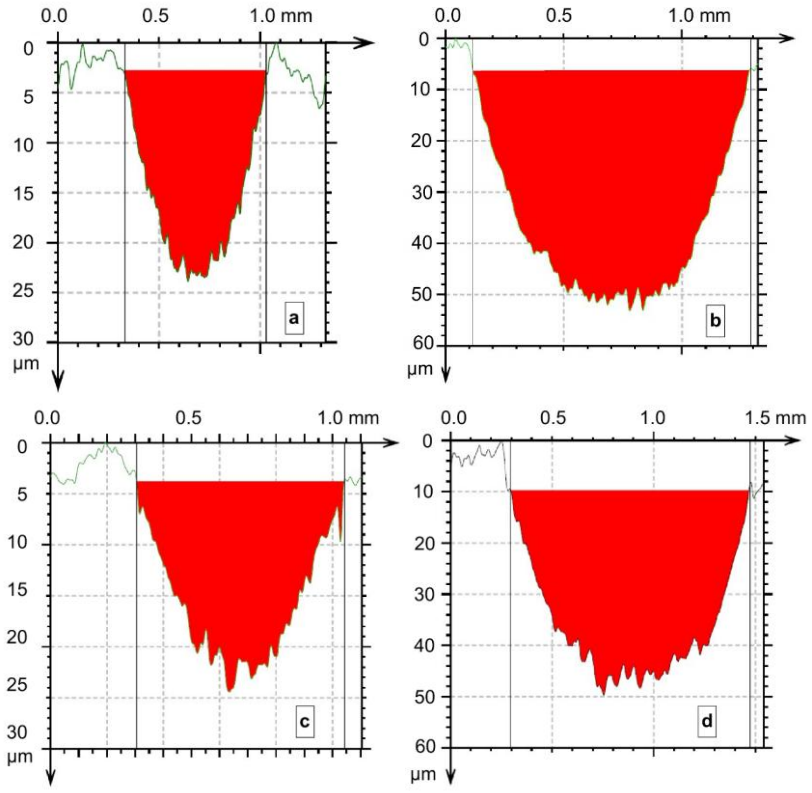

Figure 30. The wear depth profiles for (a,c) anodized as-diecast surfaces (b,d) anodized ground surfaces. The anodizing process is under (a,b) steady state voltage 35 V (c,d) steady state current 1.6 $A \cdot dm^{-2}$.

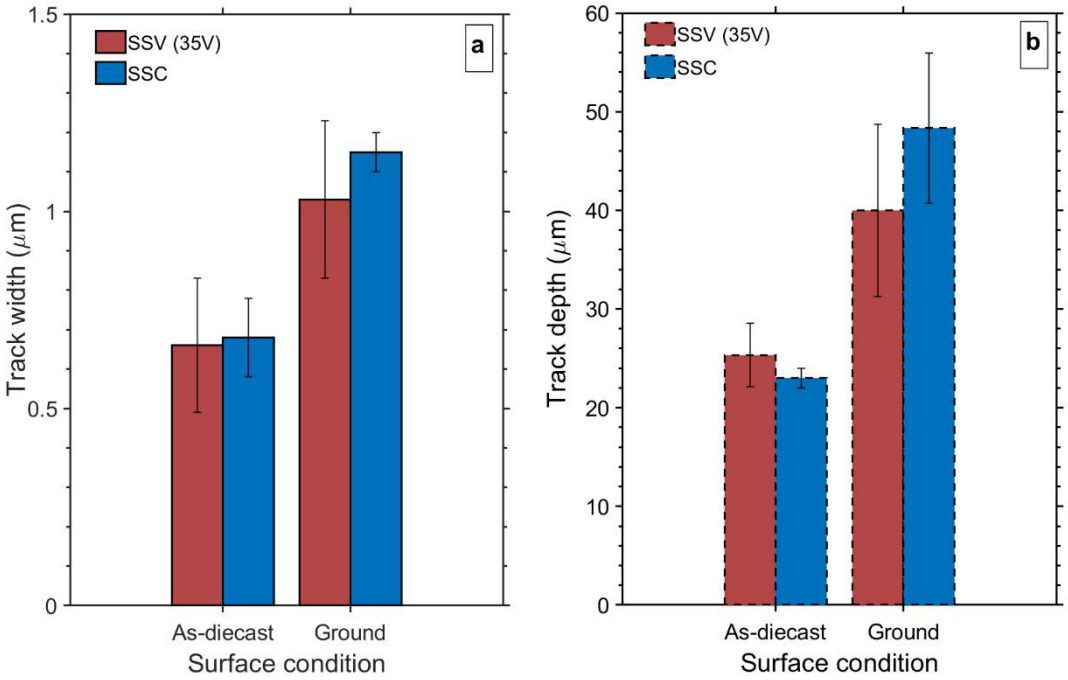

Figure 31. Variation of the (a) width and (b) depth of the worn scar in the different anodizing processes under SSV and SSC.

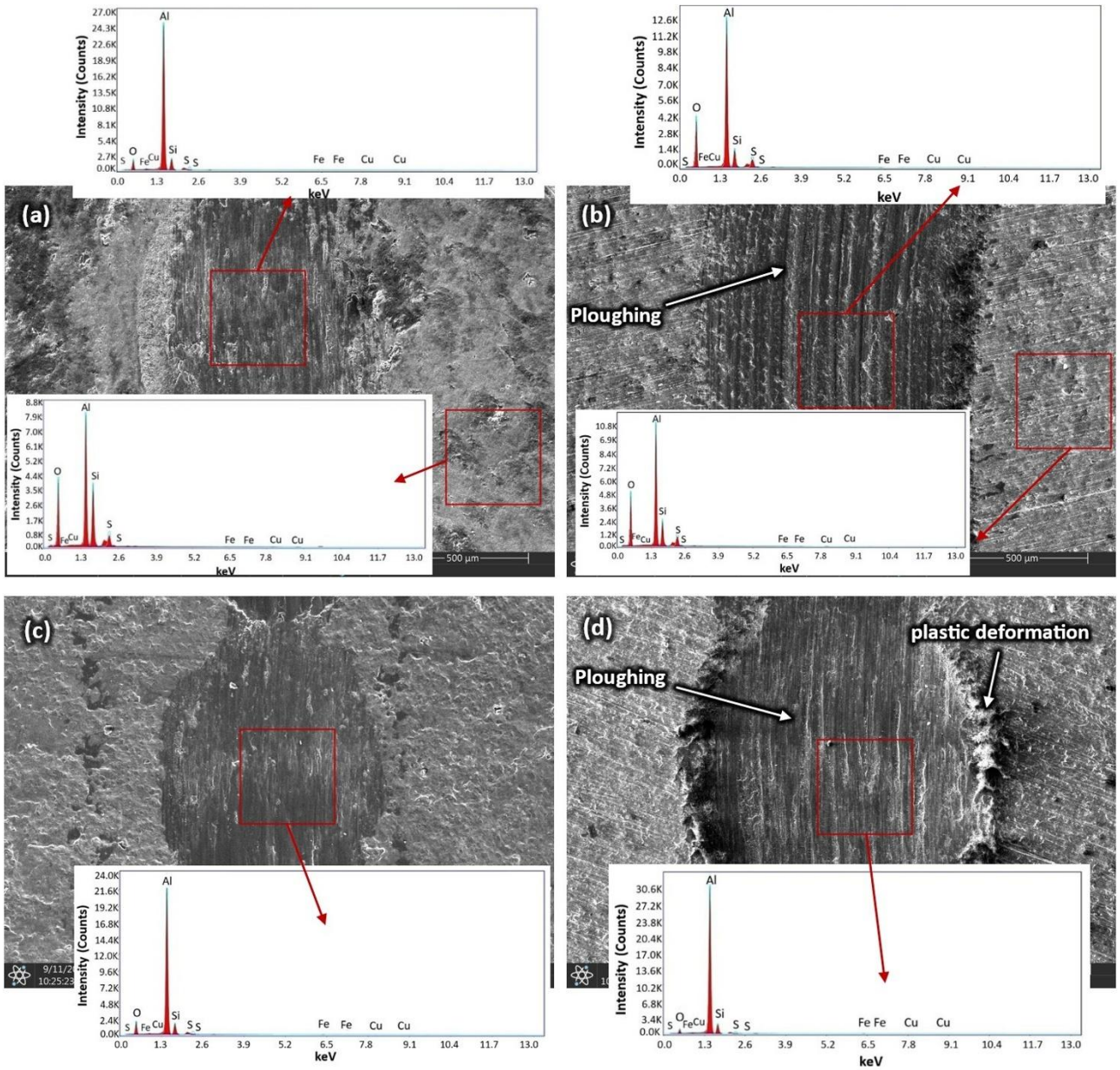

Figure 32. Typical surface appearance of wear tracks on (a,c) anodized as-diecast surfaces (b,d) anodized ground surfaces. The anodizing process is under (a,b) steady state voltage 35 V (c,d) steady state current 1.6 A·dm^{-2}.

4.8. Summary

This study presents new results from extensive wear experimental studies conducted on anodized surfaces prepared under both as-diecast and ground conditions of the Al-Si alloy substrate. In addition, another key objective was to provide new insights into the correlation among the anodic layer, its thickness, the alloy substrate microstructure, and their collective influence on the observed wear resistance. The anodizing was conducted on HPDC AlSi12Cu1(Fe) alloy under

both potentiostatic (20 and 35 V) and galvanostatic (1.6 $A \cdot dm^{-2}$) conditions using electrolyte solution containing 181.1 $g \cdot L^{-1}$ sulfuric acid, 10.6 $g \cdot L^{-1}$ aluminum, and 7.1 $g \cdot L^{-1}$ oxalic acid. The findings demonstrate that the applied electrical surface charge density is the primary factor influencing the growth and final thickness of the anodic oxide layer. In order to highlight the heterogeneous microstructure of this kind of alloy and the alteration associated with the machining process in the produced anodic layer and its properties, 1mm of material was removed prior to anodizing process. Removal of up to 1 mm exposes a subsurface region with a microstructure, marked by an increased volume fraction of the α-Al matrix and a reduced eutectic Al-Si content. This alteration facilitates enhanced oxide growth and results in thicker anodic layers. However, thicker oxide layers formed on anodized ground surfaces exhibit a higher density of cavities and defects than those on anodized as-diecast surfaces; these defects negatively impact tribological performance. The greater defect density in the anodic layer corresponds to lower microhardness values in anodized ground samples, while anodized as-diecast samples, despite having thinner anodic layers, display a more uniform oxide structure and higher hardness. The effect of surface roughness on wear resistance is comparatively minor, indicating that the intrinsic properties of the anodic layer, such as thickness uniformity, defect density, and substrate characteristics, are more influential in determining wear behavior of the anodized samples. Analysis of wear mechanisms shows that material degradation begins with brittle fracture and localized abrasive interactions at defect sites within the anodic layer, and gradually transitions to a three-body abrasion mechanism as wear debris accumulates and becomes involved in the sliding contact.

Chapter 5: Enhancing wear resistance through plasma electrolytic oxidation

5.1. Electrical response

Figure 33 illustrates the electrical response of the PEO coatings produced under different conditions, including the initial surface state (as-diecast, ground) and the electrolyte composition. The current density-time response is illustrated in Figure 33a,b, and the voltage-time response is illustrated in Figure 33c,d. The initial stage in the voltage-time response for the PEO and PEOp coatings is similar to many previous studies [9,146,147], where there is a rapid voltage increase until the corresponding breakdown voltage (~70s), which is higher for PEO than PEOp.

After breakdown, PEOp coatings took longer to reach a stable voltage, likely due to interfacial resistance or localized charge trapping caused by the strontium aluminate particles. The voltage stabilizes when the process enters the soft sparking regime, which is marked by a current drop as shown in Figure 33a,b.

During the PEO process, three distinct types of micro discharges contribute to coating growth: (1) Type-A “surface” discharges, which occur at or near the surface pores of the coating; (2) Type-B “in-depth” discharges, the most intense, originate at the coating/substrate interface; and (3) Type-C “sub-surface” discharges, which take place deeper than type-A within the micropores of the coating [102,114,115]. The balance among these discharge types is a critical determinant of coating quality, influenced by both the electrical parameters applied and the electrolyte composition [9,115]. The particles in the electrolyte affect the time required to reach the soft sparking regime [128,148]. When using a suspension containing strontium aluminate, it is noticeable that the PEO coating reaches the current drop point earlier than the PEOp coating for the two initial surface states. The transition to the soft-sparking regime typically occurs rapidly once Type B discharges evolve into smaller, more uniformly distributed events. In contrast, when particles are suspended in the electrolyte (PEOp), their interaction with the plasma and molten oxide prolongs the activity of Type B discharges. Particle entrapment and the associated local modification of dielectric properties help sustain energetic discharge channels for a longer duration, thereby delaying the onset of the soft-sparking regime compared with particle-free PEO.

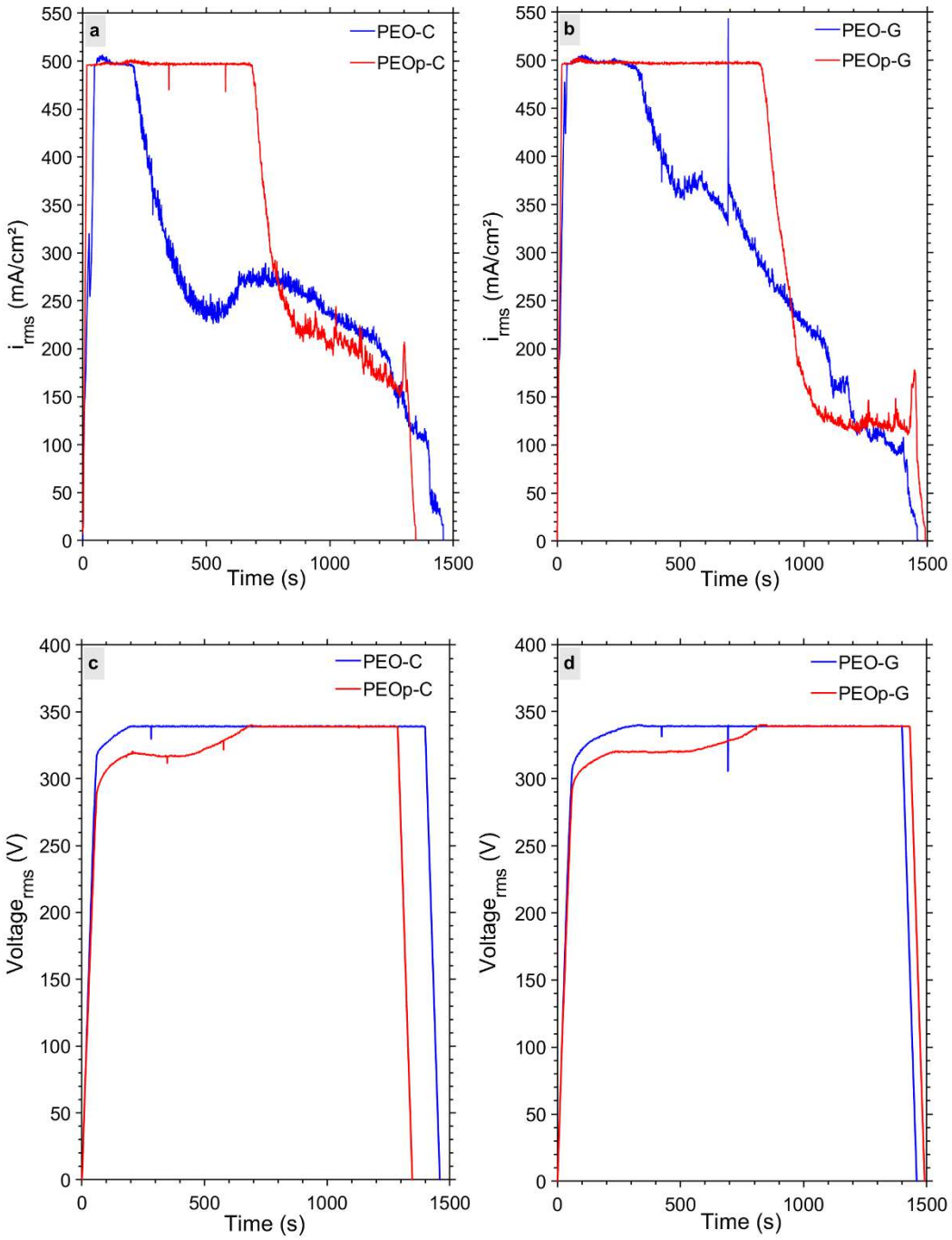

Figure 33. Current density-time response (a,b) and voltage-time response (c,d) for PEO coatings produced on as-diecast surfaces (a,c) and ground surfaces (b,d).

The microdischarges forming the PEO coating occur during the anodic half-cycle. The cathodic half is characterized by shifting the current density to negative values (Figure 34). Cathodic discharges have been reported to produce local microdischarges, but less extensively than anodic microdischarges [149,150]. From the instantaneous current density recorded at 500 s and 1000 s

for the PEO and PEOp processes, we can confirm the transition to the soft sparking regime by observing a reduction in current density. However, the instantaneous current density recorded at 500 s for PEOp is higher than that of the PEO process.

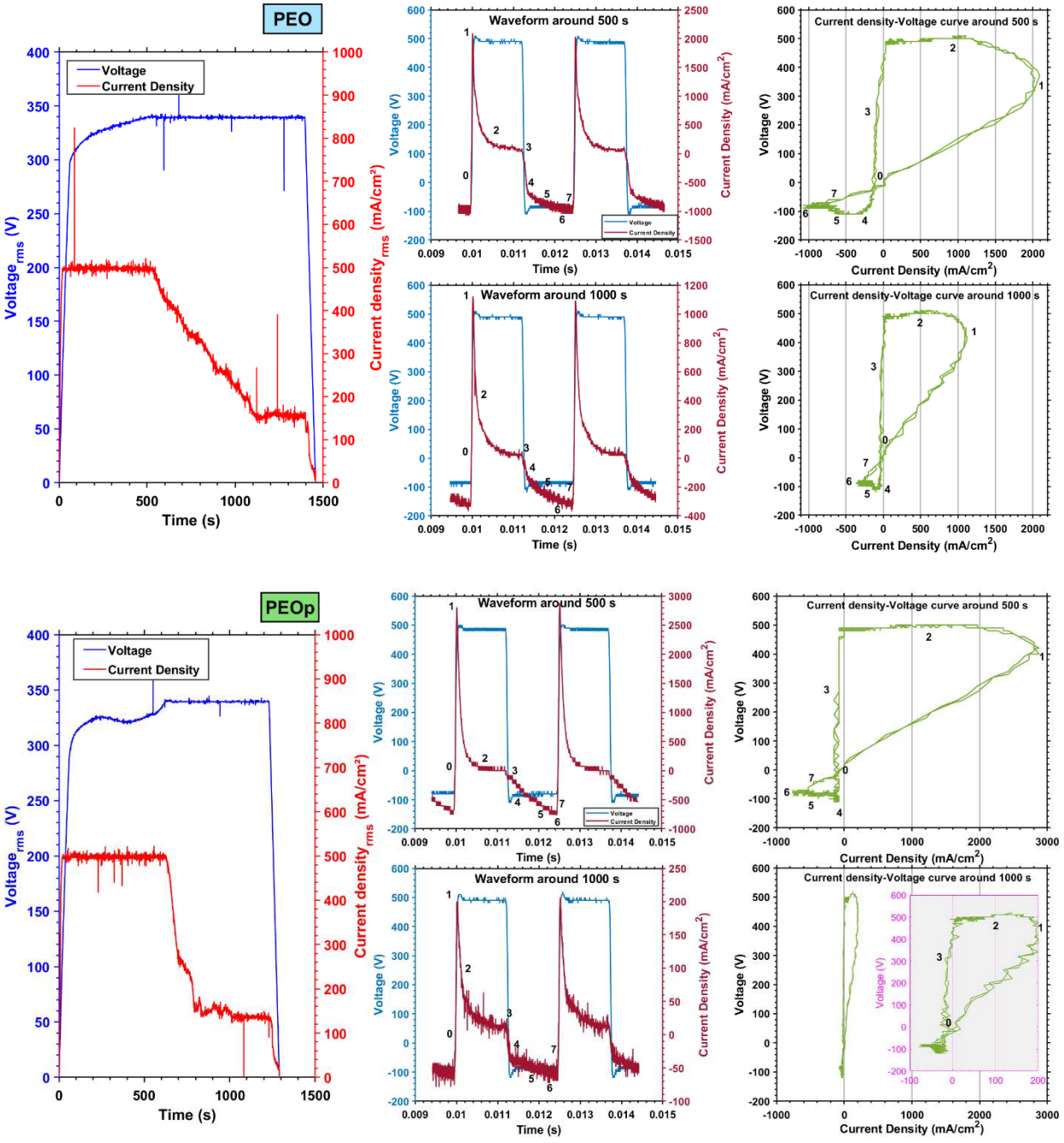

Figure 34. RMS and instantaneous voltage and current density for PEO and PEOp coatings.

The specific energy consumption during the PEO process varies with electrolyte composition [118], substrate [148,151], and electrical parameters [135]. Figure 35 compares the specific energy consumption for PEO coatings and HA layers, considering the initial surface condition (as-diecast, ground) and electrolyte composition. PEO coatings exhibit higher specific energy consumption than PEOp. For the as-diecast surface, specific energy consumption decreased from ~ 6.9 kWh·m^{-2} to ~5.5 kWh·m^{-2}, corresponding to energy savings of ~ 20%. For the ground surface, specific energy consumption decreased from ~ 7 kWh·m^{-2} to ~5.4 kWh·m^{-2}, corresponding to energy savings of ~ 23%. The reduction in specific energy consumption is attributed to improved coating growth efficiency when using suspension electrolyte. Delaying soft sparking promotes the formation of a thicker coating and greater particle incorporation. As expected, the HA has the lowest specific energy consumption. The change in specific energy consumption between HA-C and HA-G samples is not statistically significant.

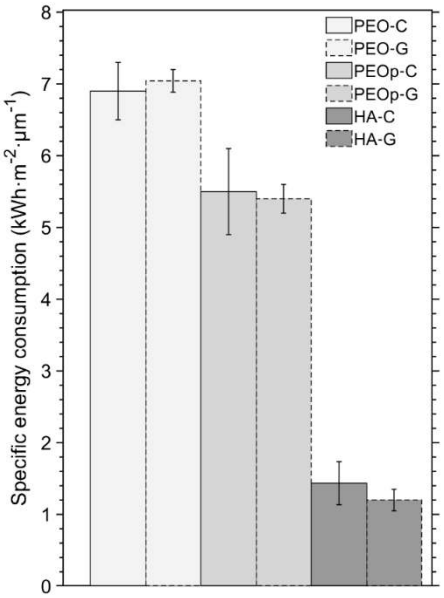

Figure 35. Specific energy consumption for hard anodizing and plasma electrolytic oxidation surface treatments.

5.2. Oxide layer thickness

HA shows the influence of the surface condition. In contrast, PEO and PEOp maintain a relatively consistent thickness regardless of the initial surface state, as shown in Figure 36.

The specific type of substrate significantly influences the anodizing process. Silicon segregation within the substrate can generate areas where the properties of the anodic layer vary considerably

[140]. This segregation usually appears in a surface region up to approximately 1 mm thick, with a high concentration of Al-Si eutectic [94]. Changes in microstructure can lead to differences in the electrochemical behavior of the surface, which then impacts the uniformity and quality of the growing anodic oxide layer [33,140]. Non-anodized Al regions may be present within the anodic layer, where oxidation-resistant Si particles surround aluminum [64–66]. This phenomenon results in a non-uniform anodic layer with variable thickness. In the PEO process, dielectric breakdown tends to occur on the SiO_2 film rather than the Al_2O_3, because the resistance of Al_2O_3 is four orders of magnitude higher than that of SiO_2 [152]. Therefore, when the PEO process has enough time for SiO_2 to reach the resistance level of Al_2O_3, microdischarges also occur on the Al_2O_3 layer [151]. At this point, the effect of SiO_2 on coating growth diminishes, as indicated in Table 7, where the average coating growth ($\mu m \cdot min^{-1}$) for PEO is similar regardless of whether the initial surface is as-diecast or ground. The same pattern is observed for PEOp coatings, although the coating growth rate is further enhanced in PEOp. HA-G shows about a 36% higher average coating growth rate than HA-C (Table 7), emphasizing the significant role of eutectic silicon in controlling oxide growth. During hard anodizing, when the advancing oxidation front reaches a eutectic Si region, it forms only a thin SiO_2 layer on the eutectic Si surface. Since further oxidation of Si requires significantly more energy than oxidizing the surrounding Al matrix, the oxide front bypasses the eutectic Si and continues through the adjacent aluminum [65,76]. Because oxide growth in HA occurs by consuming Al, a surface with more interconnected α-Al regions offers more anodizable material, thereby boosting the growth rate.

Table 7. Average oxide layer thickness, treatment time, and coating growth rate for PEO and hard anodizing samples.

Sample	Average thickness (µm)	Treatment time (s)	Average coating growth rate ($\mu m \cdot min^{-1}$)
PEO-C	50 ± 5	1400	2.10
PEO-G	52 ± 4	1400	2.20
PEOp-C	74 ± 4	1346	3.20
PEOp-G	76 ± 4	1490	3.10
HA-C	102 ± 3	10800	0.55
HA-G	135 ± 6	10800	0.75

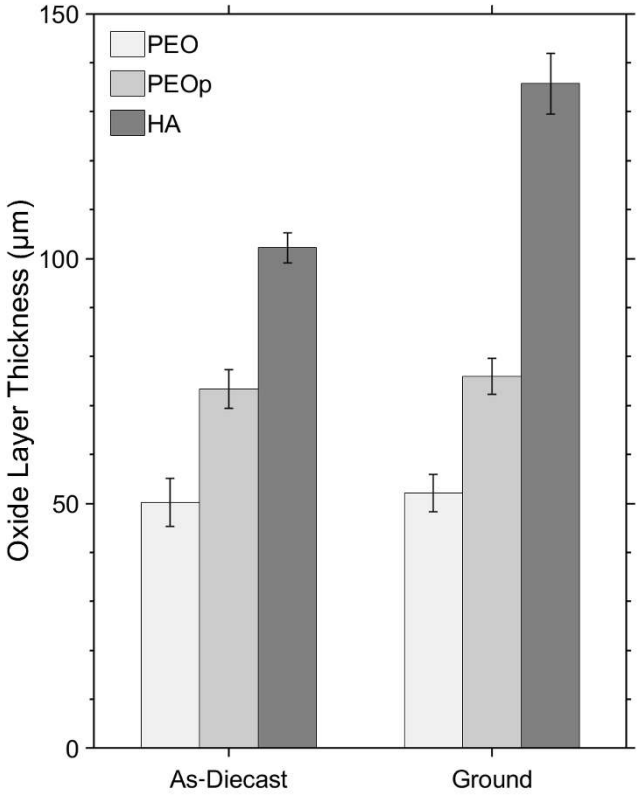

Figure 36. Oxide layer thickness variations for the studied surface treatments.

5.3. Surface roughness

Table 8 reveals the roughness variation for the studied surfaces, starting from the original surfaces (as-diecast and ground) and after applying various surface treatments (HA, PEO, and PEOp). We can observe that after HA, the as-cast surface becomes rougher, while the roughness of the anodized ground surface remains relatively unchanged compared to its condition before hard anodizing. The surface roughness for as-cast and ground surfaces increases after PEO. The increase in S_a values results from the melting and rapid solidification of the coating material in the discharge channels. The role of particles in surface roughness is significant, as both surfaces have the same surface roughness value after PEOp due to the incorporation of strontium particles in the PEO coating. The as-diecast sample has the lowest value of both S_a and S_{10z}. PEO coatings (PEO-C, PEO-G, PEOp-C, and PEOp-C) have the highest S_{10z} values. The distinct grooves from the grinding operation are visible on the ground surface (**Figure *37***b). These grooves remain noticeable even after hard anodizing (HA) (**Figure *37***d), despite the anodic layer being about 135 µm thick;

these results reflect the nature of anodic layer growth, mainly inwardly, consuming the substrate. In contrast, after the PEO process, the grinding groove features disappeared (Figure 37f,h).

Table 8. Surface roughness parameters (S_a and S_{10z}) for the studied surfaces.

Sample	S_a (µm)	S_{10z} (µm)
As-diecast	0.8 ± 0.2	10.8 ± 0.2
Ground	3.7 ± 0.5	32.0 ± 2.1
PEO-C	5.4 ± 0.4	46.1 ± 1.6
PEO-G	5.8 ± 0.5	53.3 ± 4.7
PEOp-C	3.6 ± 0.2	43.5 ± 4.2
PEOp-G	3.7 ± 0.2	41.4 ± 2.8
HA-C	1.7 ± 0.1	17.0 ± 0.5
HA-G	3.3 ± 0.2	31.0 ± 4.0

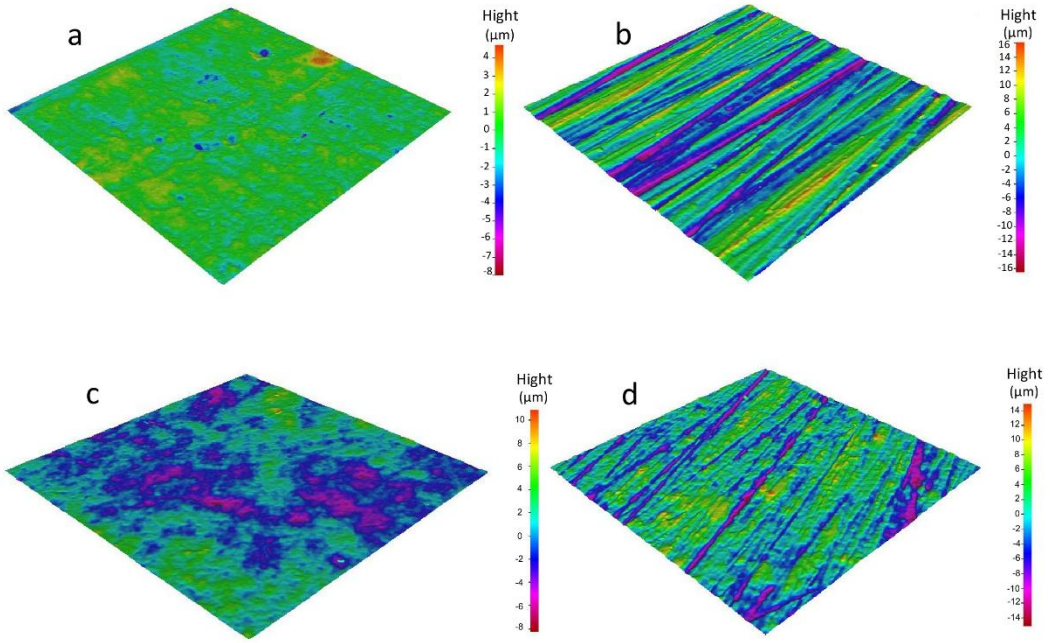

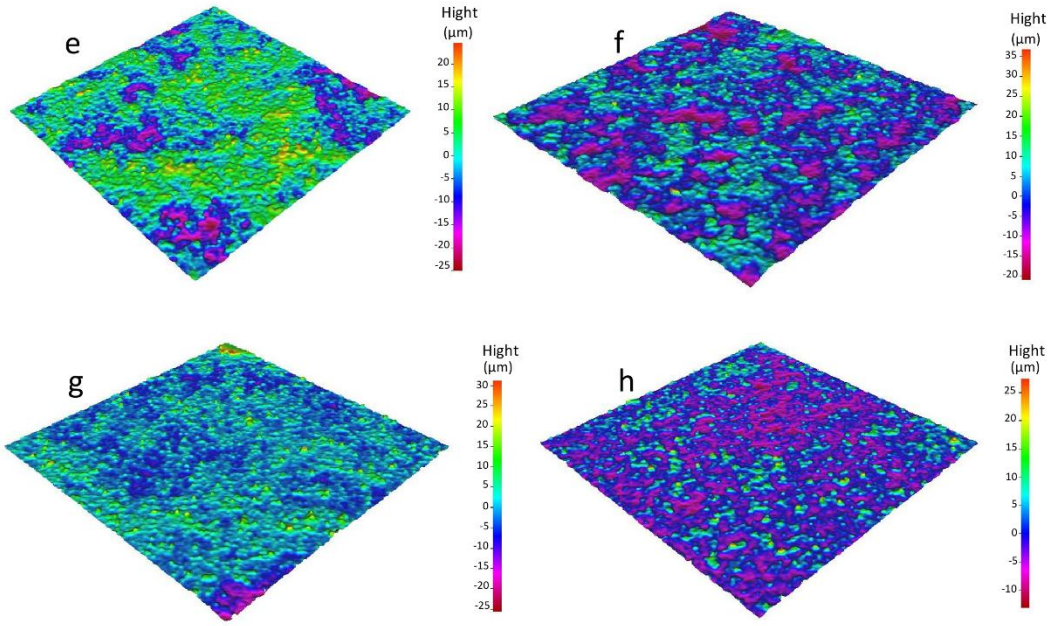

Figure 37. 3D surface topography maps of (a) as-diecast, (b) ground surfaces, and the treated samples (c) HA-C, (d) HA-G, (e) PEO-C 1400s, (f) PEO-G 1400s, (g) PEOp-C, (h) PEOp-G.

5.4. XRD and SEM analysis

XRD patterns for PEO and PEOp coatings (Figure 38) show peaks corresponding to Al and Si, indicating that the X-ray beam reached the substrate. Distinct Al peaks were observed in both HA, PEO and PEOp samples, whereas Si peaks were evident only in the PEO coating. The absence of Si in the PEOp samples may be attributed to overlapping oxide peaks or weak intensity. Several peaks corresponding to SiO_2 were clearly identified in the PEO coatings, as illustrated in Figure 38. PEO and PEOp samples also showed the presence of γ-Al_2O_3 and amorphous phases, as indicated by the characteristic bump between 20° and 35° (2θ). It is well established that the formation of α-Al_2O_3 requires specific conditions: (I) crystalline anodic oxide regions provide optimal temperature distribution and appropriately sized γ grains, allowing these grains to remain relatively free from impurities; and (II) sufficient time for mobility at the α/γ grain boundaries [153]. However, under PEO at high frequency (400 Hz), γ-Al_2O_3 is the dominant aluminum oxide phase [135,153].

In the PEO coatings, an additional phase corresponding to $Al_{4.95}Si_{1.05}O_{9.52}$ was detected. $Al_{4.95}Si_{1.05}O_{9.52}$ phase is best described as a non-stoichiometric or Al-rich mullite. It retains the same orthorhombic crystal framework as stoichiometric mullite ($3Al_2O_3 \cdot 2SiO_2$) [154,155], but

with an increased Al/Si ratio (~ 4.7). In contrast, PEOp coatings do not contain Al-rich mullite; instead, we find strontium silicate rather than strontium aluminate.

To explain this observation, the ternary oxide system Al_2O_3-SiO_2-SrO must be considered [156]. In this PEOp treatment, the electrolyte used is a suspension silicate type, and the strontium aluminate particles in the micro-arc plasma region will decompose under high-energy microdischarges that can raise the instantaneous plasma core pressure and temperature to 10^2 MPa and 10^4 K, respectively [6]. In this case, $SrAl_2O_4$ will undergo thermal decomposition, and due to the process in the silicate electrolyte, SrO will rapidly react with the silicate, as illustrated in the reactions:

$$2SrAl_2O_4 = 2SrO + 2Al_2O_3 \qquad (12)$$

$$2SrO + SiO_2 = Sr_2SiO_4 \qquad (13)$$

After combining Eqs. (12) and (13), the overall reaction is:

$$2SrAl_2O_4 + SiO_2 = Sr_2SiO_4 + 2Al_2O_3 \qquad (14)$$

It should be noted that $SrAl_2O_4$ is unstable at elevated temperatures, as confirmed by its liquidus temperatures, which indicate melting occurs at approximately 1500–1600 °C [156]. Meanwhile, the circumferential area of the microdischarges can reach temperatures over 3000 °C. This explains the formation of Sr_2SiO_4 because it is the thermodynamically stable phase when SrO reacts with SiO_2 at high PEO temperatures.

It is important to realize that the chemical reactions during the PEO process in the soft sparking region are very complex and do not follow the equilibrium phase diagram. However, ternary oxide system Al_2O_3-SiO_2-SrO still offers valuable insights into the phases likely to form under these conditions. To further validate the hypothesis, the thermodynamic stability of the reaction products was evaluated using Gibbs free energy (ΔG) values at 1000 °C [157]. The formation of strontium aluminate ($SrO{\cdot}Al_2O_3$) from SrO and Al_2O_3 shows a negative value of $\Delta G_{1000°C}$ = -59.8 kJ, indicating that the reaction is thermodynamically possible under high-temperature conditions. However, when SrO is exposed to SiO_2 present in the silicate-based electrolyte, more favorable reactions occur. The formation of $SrSiO_3$ has a $\Delta G_{1000°C}$ = -132.2 kJ, while the formation of Sr_2SiO_4, the main phase identified by XRD in the current study, exhibits an even more negative

value of $\Delta G_{1000°C}$ = -221.9 kJ. Additionally, Sr_3SiO_5 formation, although not detected by XRD, is thermodynamically the most stable ($\Delta G_{1000°C}$ = -274.7 kJ), but it may require a higher concentration of SrO. The latter data clearly indicate that under the extreme local temperatures generated during PEO, strontium preferentially reacts with silicate species rather than alumina.

$$SrO + Al_2O_3 \rightarrow SrO{\cdot}Al_2O_3 \quad \Delta G_{1000°C} = -59.8\ kJ \qquad (15)$$

$$SrO + SiO_2 \rightarrow SrSiO_3 \quad \Delta G_{1000°C} = -132.2\ kJ \qquad (16)$$

$$2SrO + SiO_2 \rightarrow Sr_2SiO_4 \quad \Delta G_{1000°C} = -221.9\ kJ \qquad (17)$$

$$3SrO + SiO_2 \rightarrow Sr_3SiO_5 \quad \Delta G_{1000°C} = -274.7\ kJ \qquad (18)$$

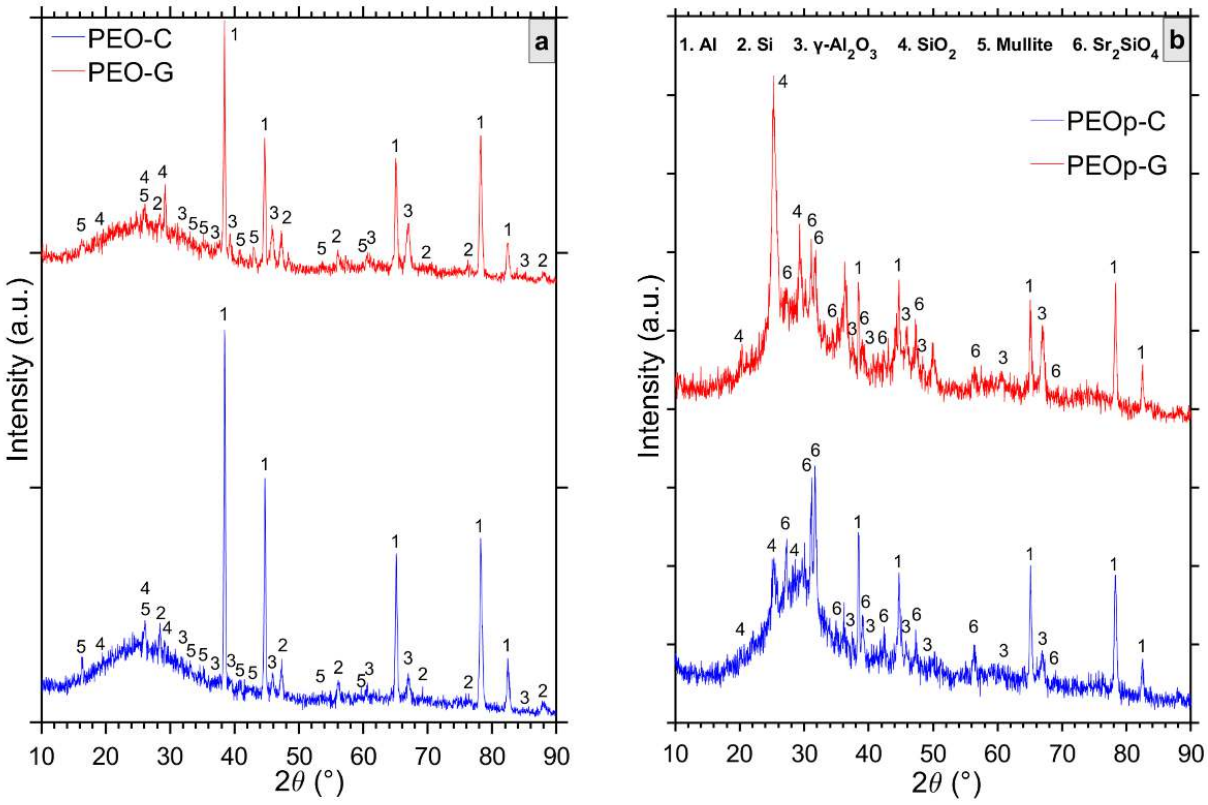

Figure 38. X-ray diffraction (XRD) patterns of (a) PEO and (b) PEOp coatings.

Figure 39 presents the backscattered SEM images of the samples' top surface, highlighting the differences between the as-diecast and ground states before and after hard anodizing and PEO treatments. The as-diecast surface exhibits irregular morphology that is preserved after HA (**Figure 39**a,c). Grinding introduces distinct grooves on the surface, thereby increasing the roughness of the

surface, as previously discussed in Section 5.3. These grooves remain visible after HA (Figure 39b,d).

The typical surface morphology associated with plasma electrolytic oxidation is observed when PEO coatings are produced in particle-free electrolytes. The morphology reflects the dynamic nature of the PEO process, where electrical discharges induce localized melting followed by rapid solidification of the created oxide. The surface morphology of the PEO coating reveals a mixture of pancake-like structure surrounded by a sponge-like morphology [158,159] (Figure 39e,f). The features that look like pancakes appear flattened, round shapes similar to tiny "craters" or discs. These are formed by micro-arc discharges that eject molten material, which then solidifies rapidly on the surface. The large pores in the middle of the pancake indicated that there were intense discharges, and these pores might extend deeply into the thickness of the coating. These intense discharges have been referred to as B-type discharges [114,115,160] . The sponge-like structure incorporates elements from the electrolyte (e.g., Si, Na, K). This region develops through repeated discharges that partially melt and vaporize the oxide material, resulting in voids and fine-scale porosity [159]. It indicates less intense thermal exposure compared to pancake zones. The previously mentioned features of PEO coating vary when a suspension electrolyte solution is used, as shown in Figure 39g,h, due to incorporating the particles into the porous layer.

Figure 40a,b shows the cross-section micrographs of the anodic layer formed on as-diecast and ground surfaces. The anodic layers exhibit typical features, including anodized α-Al grains, anodized Al-Si eutectic, and cavities. Notably, the cavity size in the anodized ground surface (**Figure 40Figure 40**b) is larger than in the anodized as-diecast surface (**Figure 40**a). Cavities are preferentially located within the eutectic Al-Si regions [66]. Additionally, cracks are present in both anodized as-diecast and ground surfaces, but these cracks are more pronounced and intense in the anodized ground surfaces. Furthermore, the cavity percentage in the anodic layer increases by approximately 260% when the initial surface is ground. The fine microstructural features and the uniform distribution of the eutectic phase on the as-diecast surfaces promote more consistent oxide layer growth with finer cavities, which are crucial for the integrity and protective qualities of the anodic layer.

The cross-section micrographs reveal that the PEO coatings are characterized by forming two distinguishable layers: porous and dense (**Figure 40**). Additionally, a thin barrier layer is formed near the coating/substrate interface due to the inner growth of the coating. This barrier layer is usually thin, amorphous and difficult to distinguish at the present magnification. PEO coatings formed on as-cast and ground surfaces have the same features. The differences between (PEOp-C, PEOp-G) and (PEO-C, PEO-G) coatings indicate that using suspension electrolytes in the PEO process significantly alters the surface morphology of the coatings. Specifically, incorporating particles into the outer porous layer results in a smoother surface texture. This effect is attributed to strontium's enhanced integration within the porous structure, primarily accumulating in the pores and cavities. Compared to PEO coatings made with particle-free electrolytes, this configuration is beneficial as it helps to minimize surface cracks and cavities. Image analysis of cross-section SEM images shows a decrease in the cavity percentage of PEO coatings when using suspension electrolyte (PEOp coatings), as shown in Figure 40. The cavity percentage declined by ~ 20% with an as-diecast initial surface and by ~ 12% with a ground initial surface. The grinding process prior to PEO results in a slight reduction in cavity percentage in the PEO coating, whereas no significant effect is observed for the PEOp coating. This indicates that the integrity of PEO coatings, in terms of cavity percentage, is not much influenced by the initial surface condition, such as grinding or similar treatments.

Table 9 presents EDS results of the HA layers, PEO and PEOp coatings. The major elements in the hard anodized layer are oxygen, aluminum, and silicon, which come from the substrate, and sulfur incorporated from the electrolyte. Figure 40a,b shows the EDS analysis location in different regions for the HA-C and HA-G samples. The results indicate a higher silicon content in the converted Al–Si eutectic regions, while the converted α-Al regions exhibit a lower silicon content.

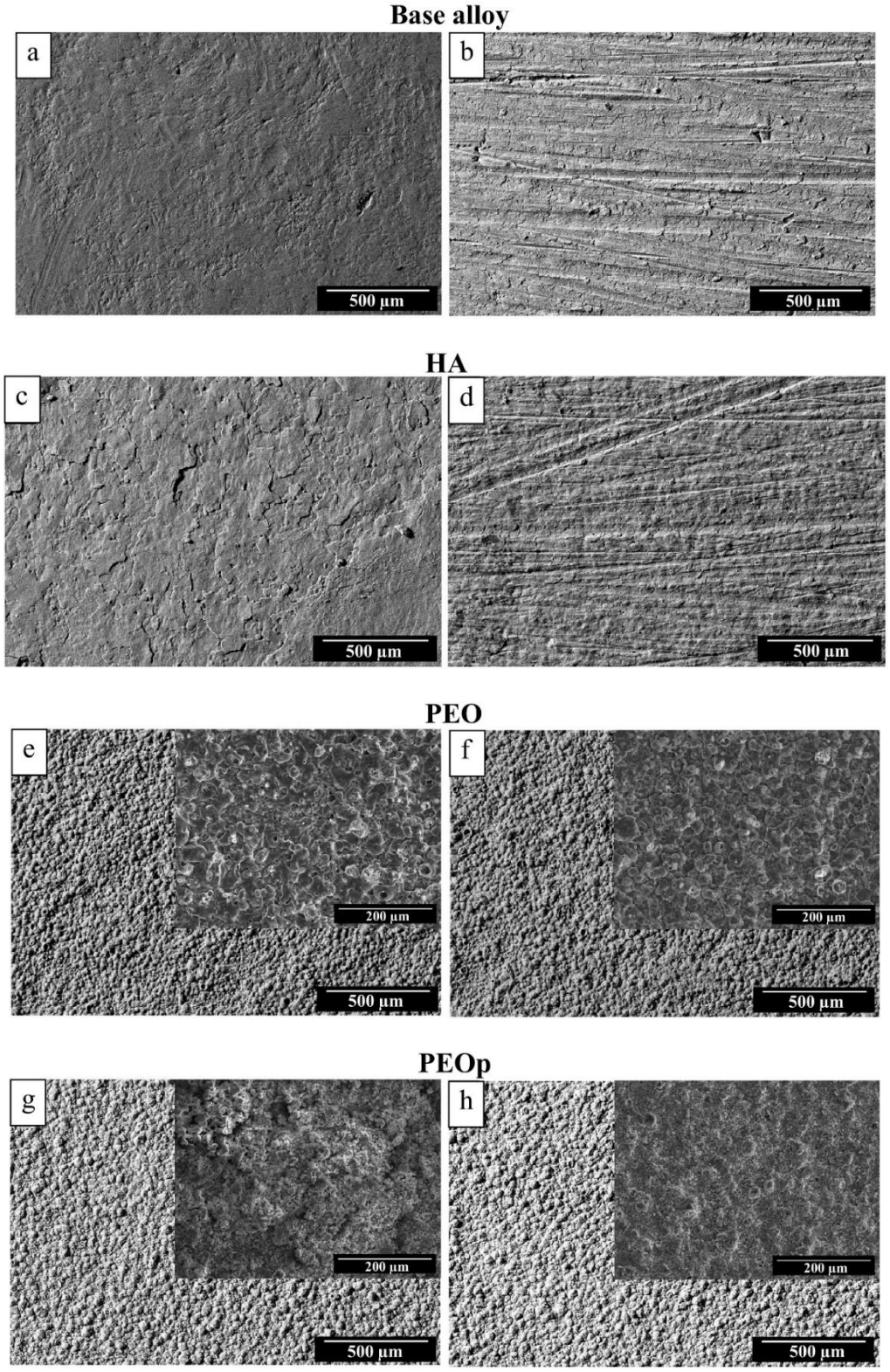

Figure 39. Scanning electron microscopy top-view images of the (a,b) base alloy, (c,d) HA, (e,f) PEO, and (g,h) PEOp. When the initial surface is (a,c,e,g) as-diecast and (b,d,f,h) ground.

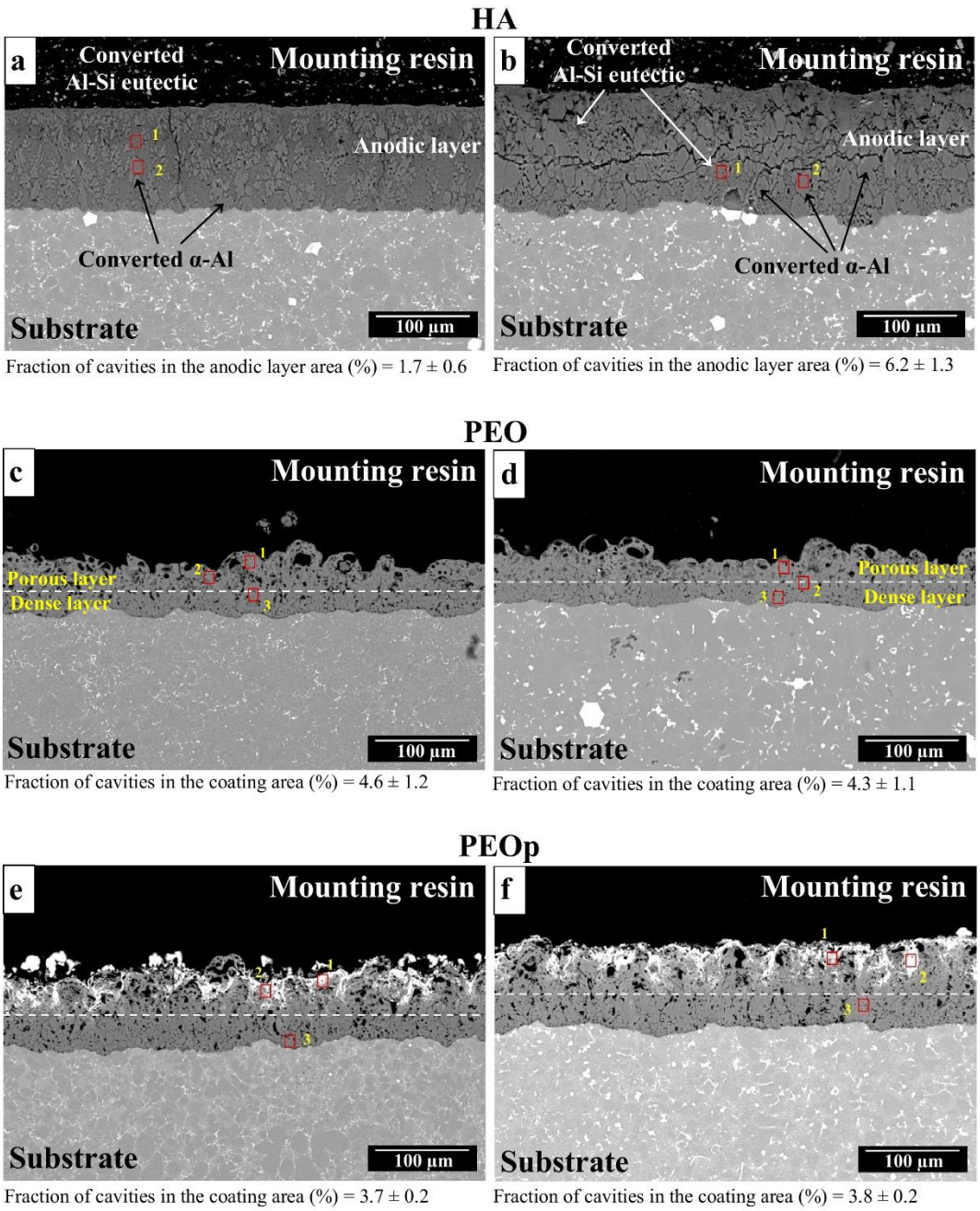

Figure 40. SEM cross-section images of the studied coatings: (a,b) HA, (c,d) PEO, and (e,f) PEOp when the initial surface is (a,c,e) as-diecast and (b,d,f) ground. Numbers indicate the locations of EDS analysis shown in Table 9.

Table 9. EDS analysis (at.%) of HA, PEO and PEOp coatings. Spectrum locations are depicted on the micrographs shown in Figure 40.

Sample	Location	O	Al	Si	Fe	S	Na	K	Sr	Other
PEO-C	1	64.6	16.3	17.6	0.1	-	0.4	1.0	-	-
	2	63.7	13.6	18.2	-	-	1.0	3.3	-	-
	3	62.8	34.1	2.8	0.1	-	-	0.1	-	-
PEO-G	1	64.2	18.6	15.7	-	-	-	1.5	-	-
	2	62.2	29.2	5.9	0.4	-	0.4	1.8	-	-
	3	62.7	22.7	13.4	-	-	-	1.1	-	-
PEOp-C	1	61.2	10.1	11.8	-	-	2.9	3.1	10.9	-
	2	64.1	19.8	10.7	0.1	-	0.8	1.7	2.3	W 0.4
	3	65.1	25.9	7.8		-	-	1.1	-	-
PEOp-G	1	63.5	16.7	10.5	-	-	2.8	3.7	2.8	-
	2	62.3	9.5	11.4	-	-	3.1	3.5	10.1	-
	3	64.7	23.5	10.5	-	-	-	1.2	-	-
HA-C	1	56.4	28.9	9.8	-	4.9	-	-	-	-
	2	54.3	38.4	1.1	-	6.2	-	-	-	-
HA-G	1	53.4	29.4	12.1	-	5.1	-	-	-	
	2	54.5	38.5	1.1	-	5.9	-	-	-	-

For the PEO coatings, the major elements are oxygen, aluminum, and silicon. Additionally, sodium (Na), and potassium (K) are incorporated from the electrolyte, while silicon also derives from the substrate. The PEOp coatings display the same elemental composition as PEO but with the addition of strontium (Sr) in the porous outer layer. EDS line analysis of PEOp-C confirms the presence of Sr in the outer porous zone (Figure 41). Furthermore, the EDS map of the PEOp-G cross-section reveals a non-uniform distribution of Sr within the porous layer (Figure 42). The results also show a decreasing aluminum concentration from the substrate toward the porous surface, while Na and K display heterogeneous distributions, being mainly concentrated in the porous outer layer.

The reactive incorporation of micro-strontium aluminate particles (0.1-10 µm) can happen due to driving the small-size particles into the discharge channels by the strong electric field and being in the area near the microdischarges (Figure 43). For this reason, strontium distribution within the coating is inherently non-uniform, as it depends on the particle's ability to infiltrate discharge channels, availability in the region near the surface, and the type of these channels. The measured zeta potential of the particles (~ –16.4 mV) indicates moderate surface charge, which suggests limited electrostatic stabilization of the suspension. Although this value alone does not allow us to determine the actual dispersion state during processing, it implies electrophoretic motion for the particles towards the specimen and incorporation in the coating during PEO. Smaller particles may enter Type-B channels during the anodic pulse (1.25 ms); however, they are typically still in the outer layer due to their size and short pulse duration. Conversely, the likelihood of strontium aluminate presence is higher in Type-A and Type-C channels, as these are closer to the electrolyte interface. The latter distribution pattern is supported by EDS line analysis (Figure 41), EDS mapping (Figure 42), and SEM cross-sectional image (Figure 40).

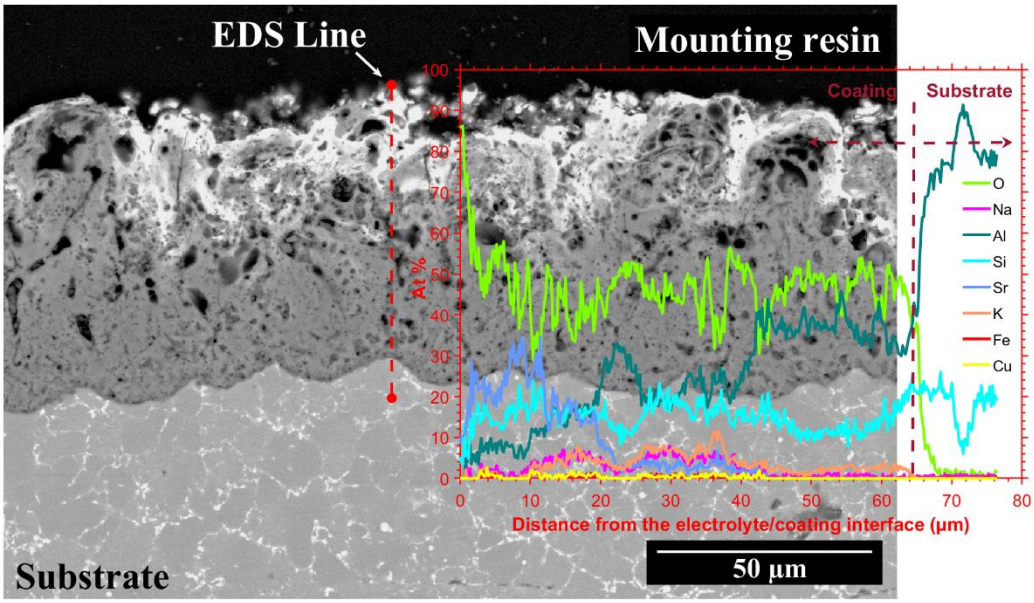

Figure 41. The cross-sectional micrograph with a typical SEM–EDS analysis result of PEOp-C.

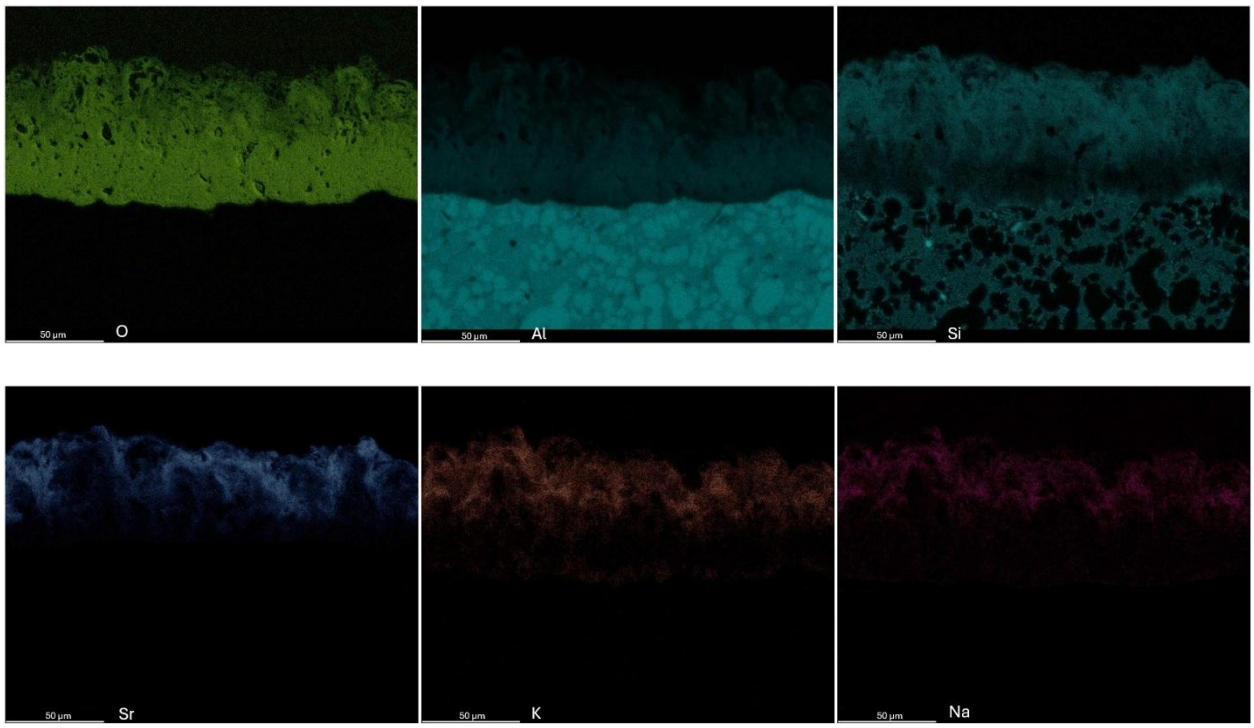

Figure 42. Elemental mapping of PEOp-G coating cross-section.

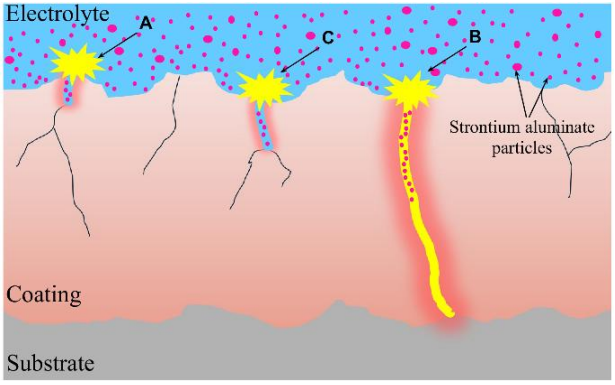

Figure 43. Schematic of the incorporation of strontium aluminate into anodic pulses during the PEO process.

5.5. Microhardness

Measuring the microhardness in the substrate cross-section underlying the oxide layer (PEO coatings and HA) indicates that the microhardness of the treated as-cast surface is 111 ± 20 $HV_{0.025}$. In contrast, the ground surface measures 82 ± 32 $HV_{0.025}$. These differences are attributed to variations in the microstructure of the AlSi12Cu1(Fe) alloy and the changes between the high-silicon eutectic region and the α-Al.

The HA as-cast surface exhibits higher microhardness (392 ± 130 $HV_{0.025}$) than the HA ground surface (291 ± 124 $HV_{0.025}$). The high standard deviation results from cavities and defects in the HA layers.

Rogov et al. [46] studied how SiO_2 influences the microhardness of PEO coatings on SLM Al-12Si alloy. They conducted the PEO process using 50 Hz alternating current (AC) at voltages up to 400 V in a silicate-based electrolyte. The findings indicated that eutectic Si oxidized to SiO_2 during PEO, while the Al matrix mainly formed γ-Al_2O_3 and α-Al_2O_3. Moreover, mixed aluminosilicate phases like mullite also developed. The presence of amorphous silica (SiO_2) resulted in lower hardness in the coatings compared to regions rich in Al_2O_3. In another study, Slonova et al. [161] performed PEO treatment on a hypereutectic AK21 alloy (containing 20–22 wt.% Si) using a silicate-based electrolyte and pulsed bipolar current at 600–750 V. The resulting coatings contained amorphous SiO_2, α-Al_2O_3, γ-Al_2O_3, and mullite. Notably, the identified amorphous SiO_2 phase was key in reducing the coating's microhardness.

Figure 44 shows the cross-sectional microhardness profile of the PEO coatings. Measurements were taken along the coating, starting 20 µm from the substrate/coating (S/C) interface and continuing further into the coating in 20 µm steps. The microhardness decreases from the substrate/coating interface to the coating/electrolyte interface, where the coating structure changes from dense to porous. This is the typical behavior of PEO coatings [162,163]. The higher microhardness values recorded for the PEOp coatings compared to PEO coatings are attributed to the positive effects of Sr_2SiO_4 presence in the coating, especially in the porous outer layer, as indicated by the EDS analysis, where the Sr element was detected in this layer. Microhardness increases for two reasons: (I) The reaction between SiO_2 and Sr species during plasma discharges produces crystalline Sr_2SiO_4 with an orthorhombic structure, as mentioned in section 3.5, which consumes amorphous SiO_2 that negatively impacts PEO microhardness; and (II) Sr_2SiO_4 fills cavities in the porous layer, enhancing coating densification and reducing crack initiation sites. Among all the coatings, PEOp-G exhibits the highest hardness. This results from the favorable initial microstructure of the ground surface, which provides more α-Al for oxide formation, and from the improved incorporation and distribution of Sr_2SiO_4, making the coating denser and enhancing its load-bearing capacity.

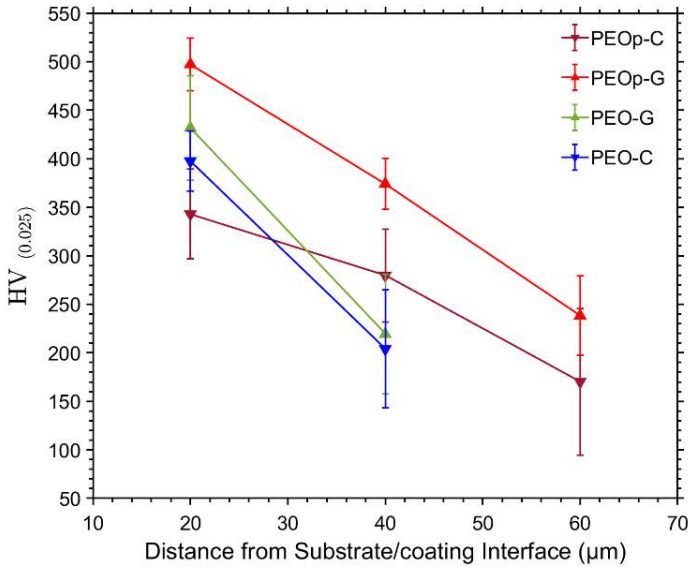

Figure 44. Microhardness profiles across PEO and PEOp coatings.

5.6. Wear test

Figure 45 shows the calculated wear rates of the tested samples. These results demonstrate the benefits of surface treatment in improving the tribological properties of casting products. The wear resistance of treated samples increased significantly compared to the initial as-diecast and ground surfaces of the base alloy. In the as-diecast state, the wear rate decreased by ~ 31% after hard anodizing, 34% after PEO, and 51% after PEOp. Due to high variability in the wear rate of the as-diecast base alloy, these results are not considered statistically significant except for PEOp. Similar trends were observed for ground surfaces, where reductions were ~ 34% after HA, 66% after PEO, and 72% after PEOp, which is statistically significant for HA and extremely statistically significant for PEO and PEOp. These findings indicate that the most pronounced improvement from PEOp occurs when the initial surface is in a ground state. This emphasizes the positive effects of the ceramic coating composite with strontium silicate, which improves the microstructure and enhances properties such as microhardness while reducing cavities and surface cracks.

When comparing the as-diecast surface with the ground surface as the initial surface before the HA, PEO, and PEOp treatments. The ground sample and HA-G exhibit higher wear rates, increased by ~ 65% and 59%, respectively. In contrast, PEO-G and PEOp-G show lower wear rates, decreasing by ~ 15% and 4%, respectively, although there is no statistical significance between the changes in the wear rates of PEOp-C and PEOp-G.

Due to the inhomogeneous microstructure of the cast alloy, whether the initial surface is in as-diecast or ground state, the wear rate data showed some variation, which is normal in tribological testing. However, PEO and PEOp reduced this variation, and the ceramic coating composite containing strontium silicate demonstrates a more consistent and stable wear rate, which is directly linked to the wear mechanism.

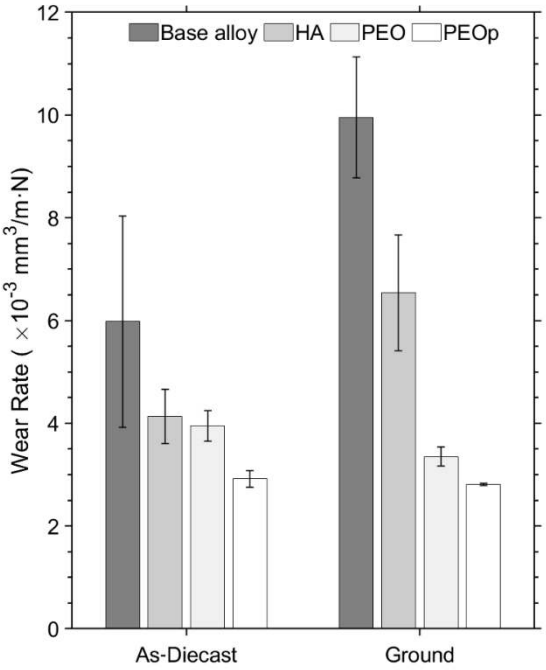

Figure 45. Variation of the wear rate on the as-diecast and ground AlSi12Cu1(Fe) alloy substrates processed with HA, PEO, and PEOp coatings.

Figure 46 shows the surface morphology of the worn tracks. In addition to a high wear rate observed for the casting alloy in different initial surface states (as-diecast and ground), the base alloy undergoes severe wear mechanisms dominated by abrasive ploughing and adhesive transfer. **Figure 46**a,b shows the characteristic features of severe wear on the as-diecast and ground surfaces, where deep grooves are evident due to the use of a hard alumina ball. The presence of wear debris further promotes the development of three-body abrasive wear as well. Under the sliding speed and applied load, adhesive wear also occurs, leading to material transfer from the weaker surface of the base alloy (in both as-diecast and ground states) onto the harder alumina ball. Evidence of this transfer and adhesive interaction can be observed in the worn track morphology.

The initial microstructure of the cast alloy strongly influences the wear depth, as illustrated in Figure 47. The ground surface exhibits a higher wear depth compared to the as-diecast surface, which is attributed to its lower hardness. Material accumulation removed during the wear test is visible along the sides of the wear track (Figure 46a,b) and in the wear track profile (**Figure 47**).

The combination of three-body abrasive and adhesive wear leads to an unstable friction coefficient, as shown in Figure 48. Initially, the friction coefficient is relatively low but gradually increases. This increase in the friction coefficient is related to several factors, including changes on the contacted surfaces of both the base alloy and the alumina ball caused by material transfer, as well as the larger contact area between the alumina ball and the tested surface due to greater wear volume loss.

In the case of hard anodized samples, Figure 46c,d reveals the worn surface of the anodic layers where the wear is controlled by abrasive combined with brittle fracture of the anodic layer. During sliding, the oxide layer fragments are compressed under the applied load and subsequently removed as wear debris from the wear track. This behavior is attributed to the inherent porosity and microcracks of the anodic layer, which promote the spallation of the oxide layer. Wear became more severe for HA-G samples due to several reasons: (I) The increased number of cavities and cracks in the HA-G layer, where the cavities are more than three times greater than those in HA-C, as detailed before. (II) The higher hardness of HA-C than HA-G. Figure 47 shows a broader and deeper wear profile for HA-G compared to HA-C. The as-diecast surface contains a higher Si content than the ground surface, leading to embedded Si in the anodic layer. This Si enrichment increases the hardness of the oxide layer, resulting in a higher friction coefficient for HA-C than HA-G, as illustrated in Figure 48.

The hard anodizing process improves the initial surface's wear resistance by lowering the wear rate, as illustrated in Figure 45. However, the HA-G samples exhibit similar wear resistance to the as-diecast surfaces, despite the latter having lower hardness. This could be due to microstructural differences and the wear mechanism, where high cavities and cracks accelerate material loss. The HA-G shows a consistent wear depth, while the wear track on the as-diecast surface is irregular, featuring deep, wide grooves and uneven scars.

Surface morphology of the worn tracks of PEO-C and PEO-G coatings reveals the formation of a tribolayer (Figure 46e,f). The composition of the tribolayer varies depending on the counter material. The concept of forming a tribolayer can rely on oxidative wear in dry conditions, where the applied load and sliding promote re-oxidation and incorporation of counter body fragments into the tribolayer [128,164]. As previously noted, an alumina ball was selected as the counter body to ensure consistency in assessing the wear behavior of the tested materials.

The average thickness of PEO-C coating is 50 ± 5 µm and the wear depth profile reaches ~ 45 µm (Figure 47). EDS analysis of the tribolayer formed on the PEO-C wear scar indicates a reduction in Si and Na elements predominantly concentrated in the porous outer layer of the coating. The wear rate of PEO-C coating is similar to HA-C as depicted in Figure 45, with both exhibiting a similar wear profile (Figure 47). However, the formation of the tribolayer contributes to lowering the friction coefficient of PEO-C, despite its relatively high surface roughness, as shown in Figure 48.

PEO-G coating shows similar tribolayer formation but superior wear resistance to PEO-C. This improvement is attributed to its higher hardness and lower cavity percentage (Figure 40), resulting in a shallower wear depth (Figure 47). Consequently, PEO-G exhibits a lower wear rate and a reduced friction coefficient relative to PEO-C (Figure 48). Unlike PEO-C, PEO-G also outperforms HA-G, due to its higher hardness and fewer structural defects.

The most enhanced performance is observed in PEOp coatings, which incorporate strontium silicate to form a composite ceramic coating. The tribological enhancement arises from reducing the surface roughness and increasing the coating growth. The wear track morphology of PEOp-C and PEOp-G (Figure 46g,h) shows a more uniform and stable tribolayer. As illustrated in Figure 45, PEOp coatings exhibit the lowest wear rates. The wear depth is also reduced, reaching ~33 µm for PEOp-C, while the alumina counter ball remains within the porous outer layer after testing. EDS line analysis (Figure 41) confirmed the presence of strontium within this region to a depth up to ~42 µm from the surface, while EDS analysis of the worn surface (Figure 46g) further demonstrates the presence of strontium within tribolayer and delaminated regions. For PEOp-G, the wear depth remains limited to the outer porous layer, without reaching the underlying dense layer (Figure 46h). The friction coefficient of PEOp-C is slightly lower than that of PEOp-G (Figure 48).

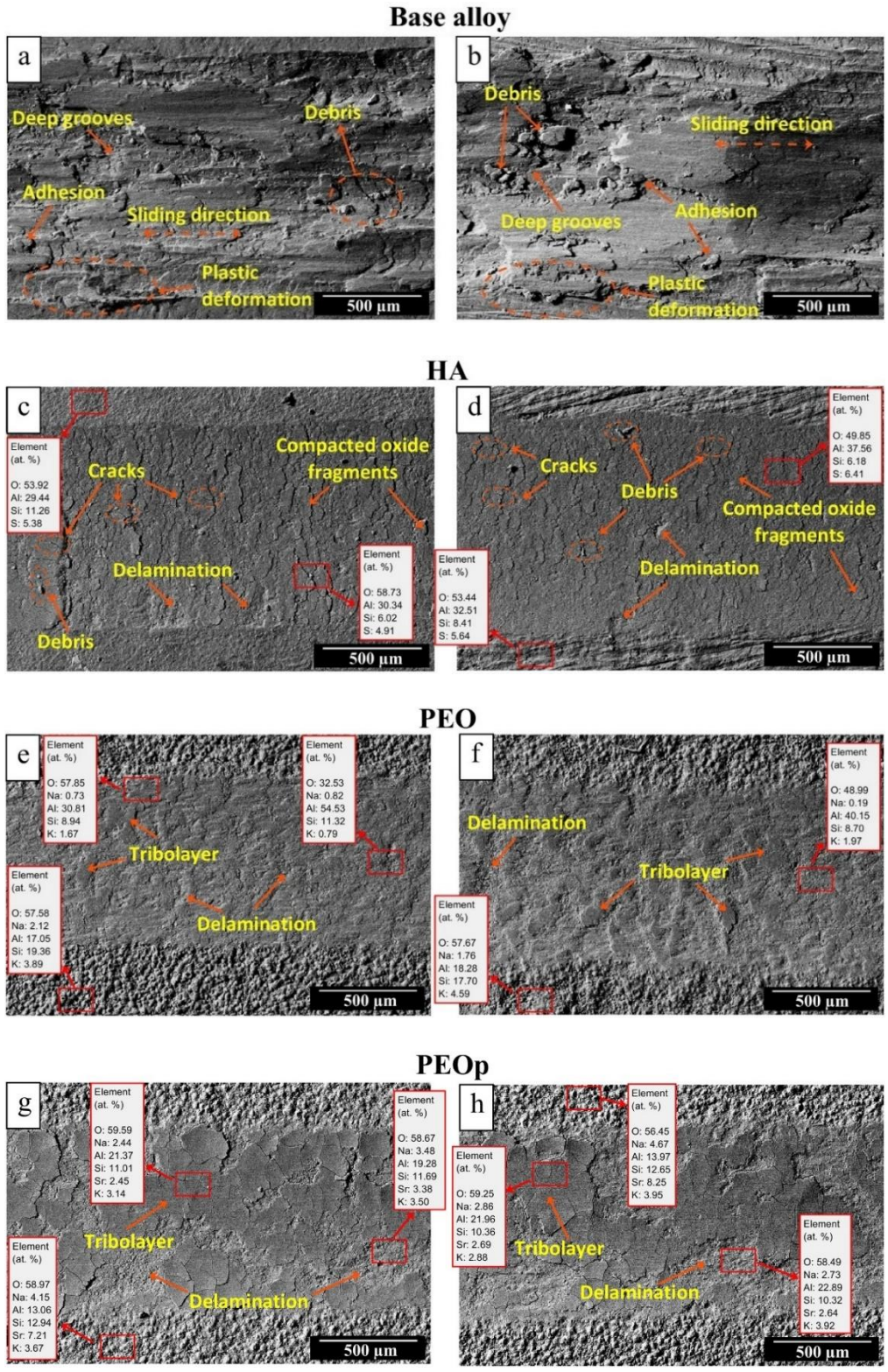

Figure 46. Surface morphology of the worn tracks of (a,b) base alloy, (c,d) HA, (e,f) PEO, and (G,H) PEOp. When the initial surface is (a,c,e,g) as-diecast and (b,d,f,h) ground.

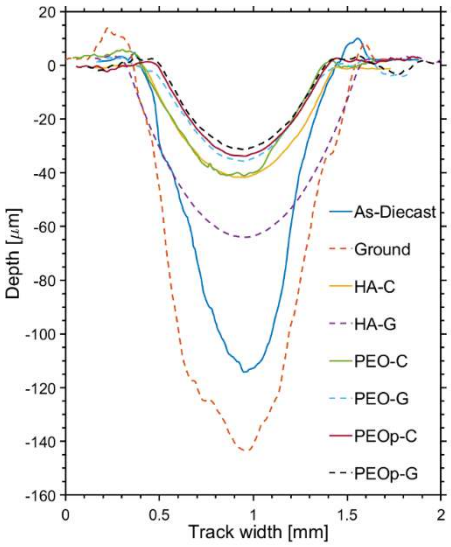

Figure 47. Cross-section wear scar profiles for treated and untreated samples.

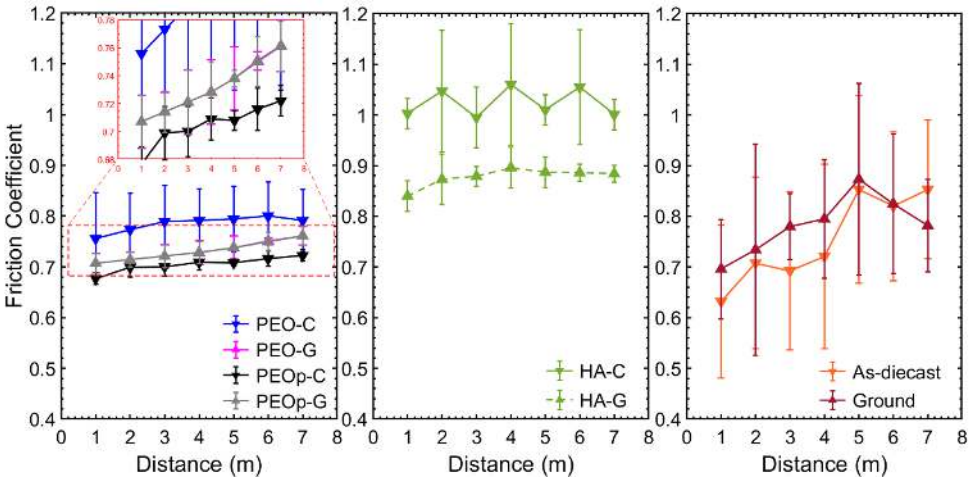

Figure 48. Friction coefficient vs. sliding distance for PEO treated, HA treated and untreated samples.

5.7. Summary

This study systematically investigates the effect of suspended strontium aluminate particles in a silicate-based electrolyte during the PEO process on an AlSi12Cu1(Fe) diecast alloy. Particular attention is given to the in-situ formation of Sr_2SiO_4 phases and how they influence coating growth efficiency, energy consumption, and wear resistance. For comparison, hard anodizing (HA) layers were also produced under controlled conditions. Finally, the role of the initial surface microstructure (as-diecast and ground) is considered to clarify how the substrate condition interacts with HA, PEO, and PEOp processing in determining the final coating performance. The

findings demonstrate that strontium aluminate particles are reactively incorporated into the PEO coating, forming a new phase of strontium silicate and creating a composite ceramic coating (PEOp). The oxide layer growth shows a strong dependence on the initial surface conditions for HA, whereas PEO and PEOp coatings are unaffected by whether the substrate was as-diecast or ground. The higher coating growth rate for PEOp (~3.20) compared to PEO (~2.20) results in thicker PEOp coatings, which help reduce the specific energy consumption of the PEOp process by approximately 20% for as-diecast substrates and about 23% for ground substrates. XRD analysis confirms that conventional PEO coatings mainly consist of γ-Al_2O_3, SiO_2, and Al-rich mullite phases, while PEOp coatings additionally contain Sr2SiO4 phase. The presence of strontium silicate arises from the thermal decomposition of $SrAl_2O_4$ particles during micro-discharges, followed by the reaction of the resulting SrO with silicate species from the electrolyte. The formation of Sr_2SiO_4 phases reduces the amorphous SiO_2 content within the coating, leading to a more crystalline structure that enhances microhardness. This effect is especially notable in PEOp coatings on ground substrates, which exhibit the highest microhardness values among all tested conditions. Scanning electron microscopy shows that the hard anodized layer formed on ground surfaces contains a higher density of cavities and defects compared to that on as-diecast surfaces. Coupled with the lower microhardness of HA-G, this microstructural feature results in inferior wear resistance compared to HA-C.

The successful incorporation of strontium into the porous outer region of PEOp coatings were confirmed by EDS. This incorporation reduces the cavity fraction and decreases cracks and porosity in the outer layer of the PEO coating.

Wear testing consistently reveals that PEOp coatings demonstrate the most favorable wear behavior, including the lowest wear rates compared to the base alloy, HA, and PEO, regardless of whether the initial surface was as-diecast or ground. These improvements in wear rate are statistically significant in all cases. Comparing PEO and PEOp coatings, the reduction in wear rate when strontium silicate is present in the porous outer layer is highly statistically significant, attributed to the development of a stable and protective tribolayer during sliding. Collectively, these results suggest that particle-assisted plasma electrolytic oxidation is an effective strategy for enhancing energy efficiency, coating microstructure—particularly the outer porous layer—and tribological performance.

Chapter 6: Corrosion performance of PEO coatings

6.1. Electrochemical testing of PEO coatings

Generally, Plasma electrolytic oxidation (PEO) surface treatment contributes to enhancing the corrosion resistance of metallic substrates. However, this enhancement may vary depending on the microstructural features of the PEO coatings. The PEO coating has microstructural imperfections, including micropores, microcracks, and discharge-induced channels, which can reduce coating integrity [106]. These defects serve as preferential pathways for aggressive ionic species to pass through the coating to the underlying substrate, which diminishes the long-term protective performance of the coating system.

Open-circuit potential (OCP) measurements are widely used as an initial electrochemical parameter to assess the corrosion tendency of materials exposed to specific corrosive environments. OCP represents the equilibrium potential of the tested material, such as a PEO-coated specimen, relative to a reference electrode under conditions where no external current or polarization is imposed on the electrochemical system [165]. Although OCP measurements provide valuable qualitative information, they are insufficient on their own to demonstrate the corrosion mechanisms and corrosion kinetics [166,167].

Despite this limitation, OCP evaluation remains essential to indicate the relative corrosion susceptibility of PEO-coated samples, with more negative potentials generally indicating a higher tendency toward corrosion. OCP measurements establish a stable reference point for subsequent electrochemical analyses, particularly potentiodynamic polarization (PDP) and electrochemical impedance spectroscopy (EIS), which are among the most frequently applied techniques for investigating the corrosion behavior of PEO coatings [106,168,169]. Consequently, this chapter focuses on the results obtained from PDP and EIS measurements, supplemented by post-corrosion microstructural observations of the samples following a 7-day immersion period during the PDP corrosion testing.

6.2. Electrochemical impedance response

In this method, a low-amplitude perturbation potential (approximately 10 mV) is applied to the PEO-coated electrode over a broad frequency range, and the electrochemical response is recorded. The results can be represented using either Nyquist or Bode formats. Bode plots illustrate the variation of impedance magnitude and phase angle with frequency. The impedance data obtained from both representations can be analysed by fitting them to a suitable equivalent electrical circuit, enabling the determination of time-dependent characteristics of the PEO coating, including capacitance and the resistive contributions of the porous and barrier layers. In this experiment, results include Bode and Nyquist plots, along with an equivalent circuit, to determine the corrosion behaviour of the different PEO samples at different immersion times.

EIS experiments were performed on PEO and PEOp samples with two initial surface conditions: as-diecast and ground. Figure 49 illustrates the results obtained from EIS as a Bode plot (impedance and phase angle as a function of applied frequency) and a Nyquist plot. From the Bode impedance plot (Figure 49a), we can record the impedance at 0.01 Hz, $Z_{0.01}$, which provides a good indication of how PEO-coated samples respond after up to 7 days of immersion. Figure 49a reveals that the $Z_{0.01}$ decreases by increasing the immersion time for all studied cases; however, the PEO samples have a relatively stable $Z_{0.01}$ after 72 h, whereas the PEOp samples have lower $|Z|_{0.01}$ after 7 immersion days. PEOp-G has the higher $Z_{0.01}$ until 72h; after that, the higher $|Z|_{0.01}$ is for PEO coatings. Figure 50 reveals the changes in $Z_{0.01}$ by immersion time. PEO coatings have a lower thickness compared to PEOp coatings. Using suspension electrolyte increases coating thickness by up to ~ 46%. However, the lower $Z_{0.01}$ for PEOp coatings can be attributed to the cavities that exist in the inner layer, even though the total cavity percentage of the PEOp coatings reduced as a result of using suspension electrolyte, where the particles contribute to reducing the cavities in the outer porous layer. Still, we can see from the microstructure in Figure 40 that cavities are present near the substrate/coating interface in PEOp coatings more than in PEO coatings. This is an approximately 88% decrease in impedance for PEOp-C from 1h to 7 days, and a ~ 79% decrease for PEOp-G; the change in $Z_{0.01}$ for PEOp-G and PEOp-C after 7 days immersion is not quite statistically significant. For PEO coatings, $Z_{0.01}$ decreased by ~ 69% after 24h but remained relatively stable after 7 days of immersion.

The results of the EIS quantitative analysis (Table 10) are fitted using the "ZSimpWin" software. EIS data were interpreted using an equivalent circuit consisting of the solution resistance (R_s) in series with three parallel resistance–constant phase element (R‖CPE) pairs, representing the electrochemical responses of the outer porous layer (R_{out}‖CPE_{out}), inner barrier layer (R_{in}‖CPE_{in}), and metal/electrolyte interface (R_{ct}‖CPE_{dl}), Figure 51 reveals the equivalent circuit used to fit the impedance data obtained from the tested specimens. The outer porous layer response appears at high frequencies due to its relatively small time constant, whereas the inner barrier layer exhibits a dominant mid-frequency phase peak associated with its higher resistance and more capacitive nature. The low-frequency response, governed by the R_{ct}‖CPE_{dl} element, corresponds to the formation of the electrical double layer and charge-transfer processes at the metal/coating interface and becomes increasingly influential with immersion time.

For both systems PEO and PEOp, the outer layer exhibits a markedly lower impedance than the inner layer (Table 10), reflecting its higher porosity and weaker barrier properties. In contrast, the inner layer exhibits substantially higher impedance values and serves as the primary protective layer of the coating. A comparison between the two coatings shows that the inner layer of the PEO coatings displays a higher impedance than that of the PEOp coatings. The observed difference can be attributed to microstructural characteristics arising from the higher current density shown in Figure 34. This phenomenon leads to more intense discharge before the transition into the soft-sparking regime.

The PEO coatings exhibit significantly higher R_{ct} than the PEOp coatings, indicating that electron-transfer processes associated with corrosion are more strongly hindered. Consequently, the higher R_{ct} values observed for the PEO coatings suggests that they provide superior protection against corrosion compared with the PEOp coatings.

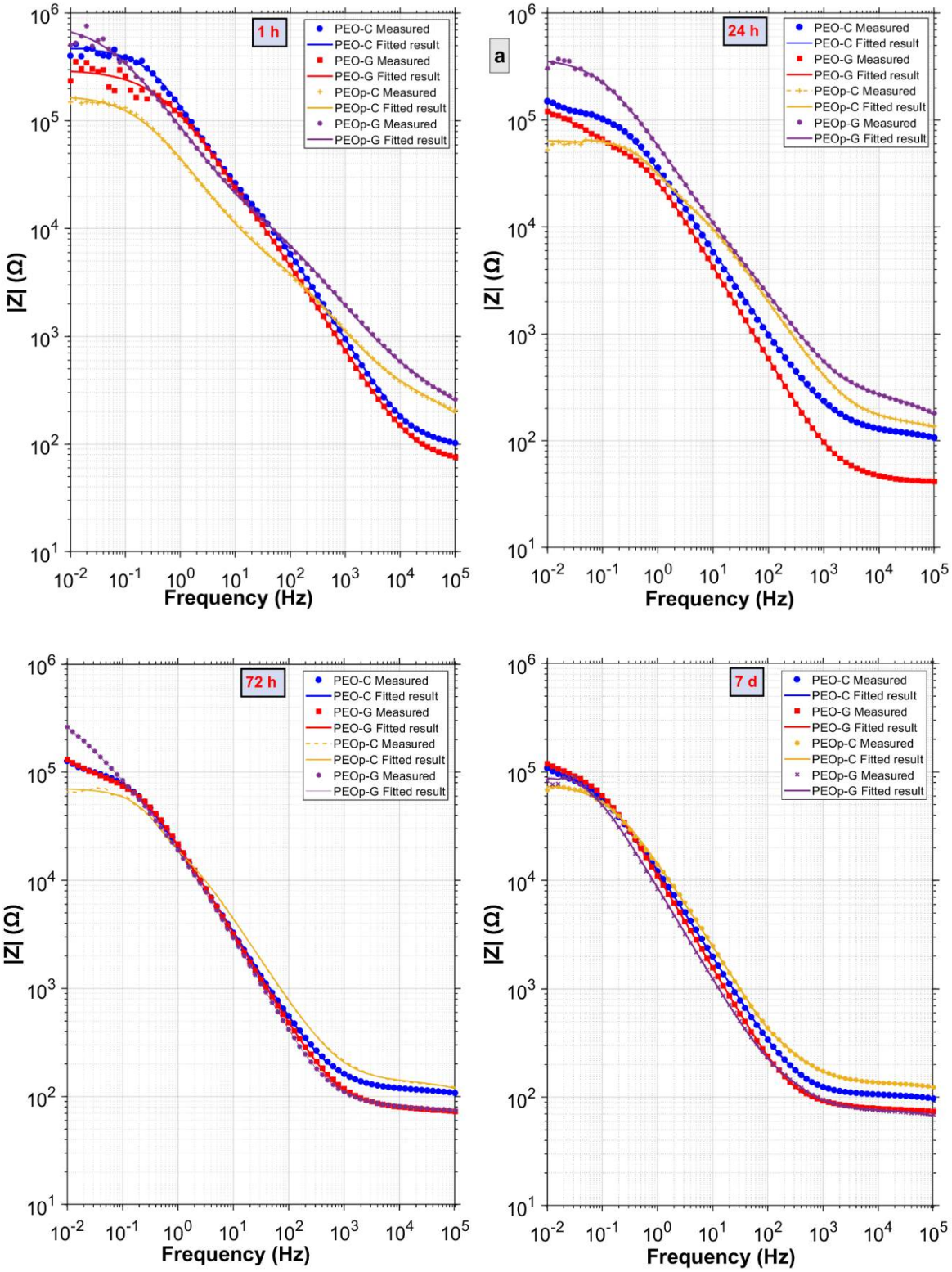
1 h
24 h
a
72 h
7 d
PEO-C Measured
PEO-C Fitted result
PEO-G Measured
PEO-G Fitted result
PEOp-C Measured
PEOp-C Fitted result
PEOp-G Measured
PEOp-G Fitted result
|Z| (Ω)
Frequency (Hz)

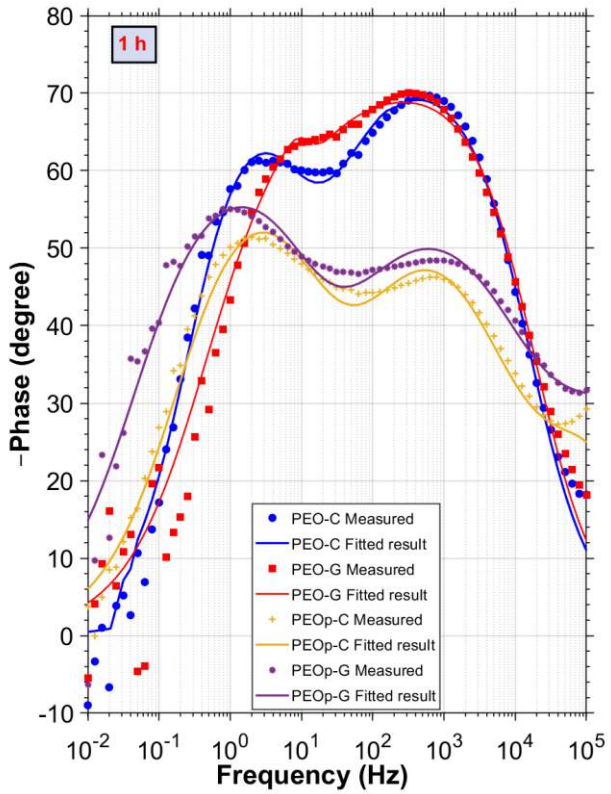
1 h
-Phase (degree)
Frequency (Hz)
PEO-C Measured
PEO-C Fitted result
PEO-G Measured
PEO-G Fitted result
PEOp-C Measured
PEOp-C Fitted result
PEOp-G Measured
PEOp-G Fitted result

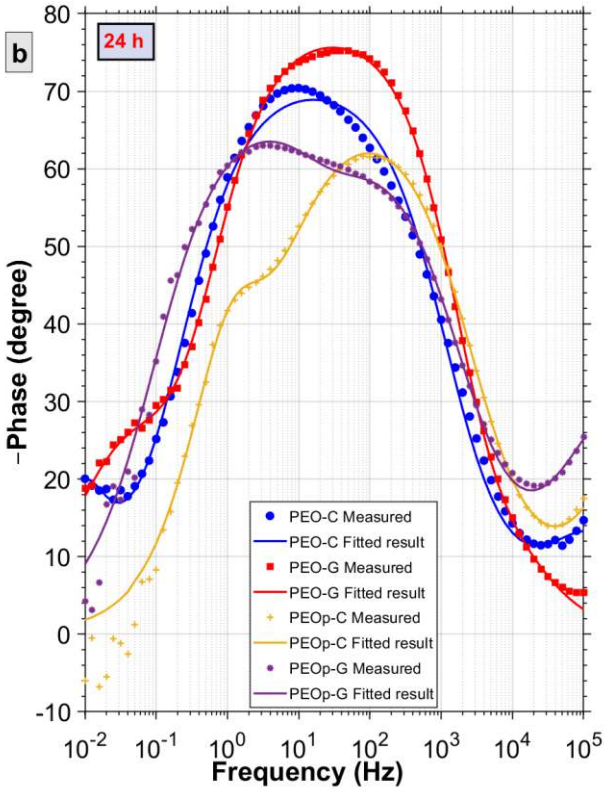
b
24 h
-Phase (degree)
Frequency (Hz)
PEO-C Measured
PEO-C Fitted result
PEO-G Measured
PEO-G Fitted result
PEOp-C Measured
PEOp-C Fitted result
PEOp-G Measured
PEOp-G Fitted result

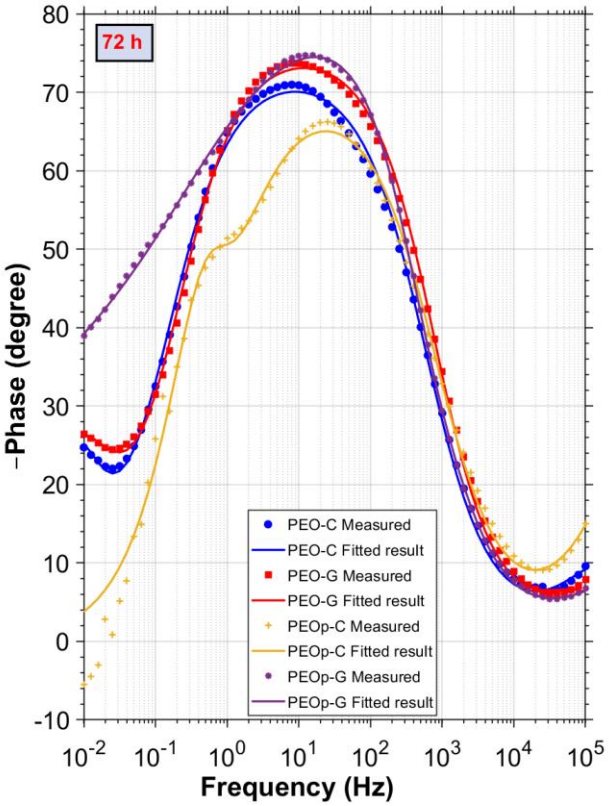
72 h
-Phase (degree)
Frequency (Hz)
PEO-C Measured
PEO-C Fitted result
PEO-G Measured
PEO-G Fitted result
PEOp-C Measured
PEOp-C Fitted result
PEOp-G Measured
PEOp-G Fitted result

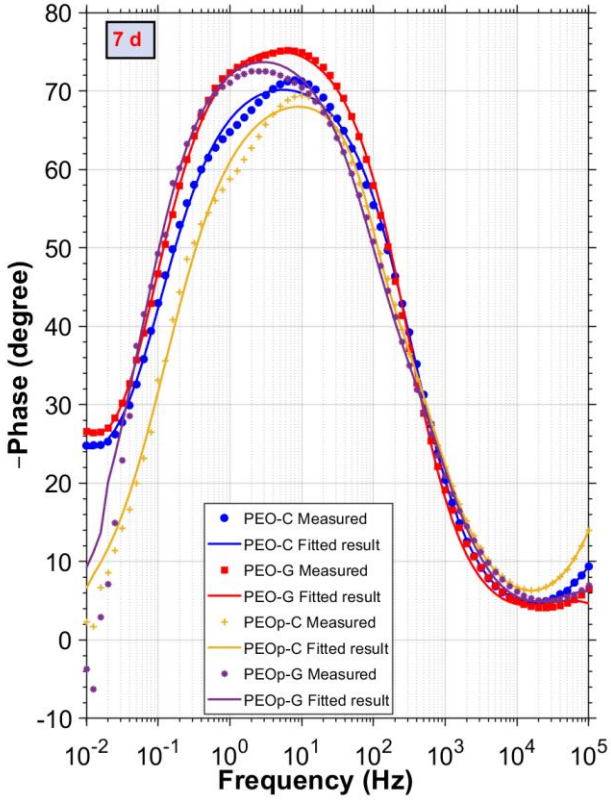
7 d
-Phase (degree)
Frequency (Hz)
PEO-C Measured
PEO-C Fitted result
PEO-G Measured
PEO-G Fitted result
PEOp-C Measured
PEOp-C Fitted result
PEOp-G Measured
PEOp-G Fitted result

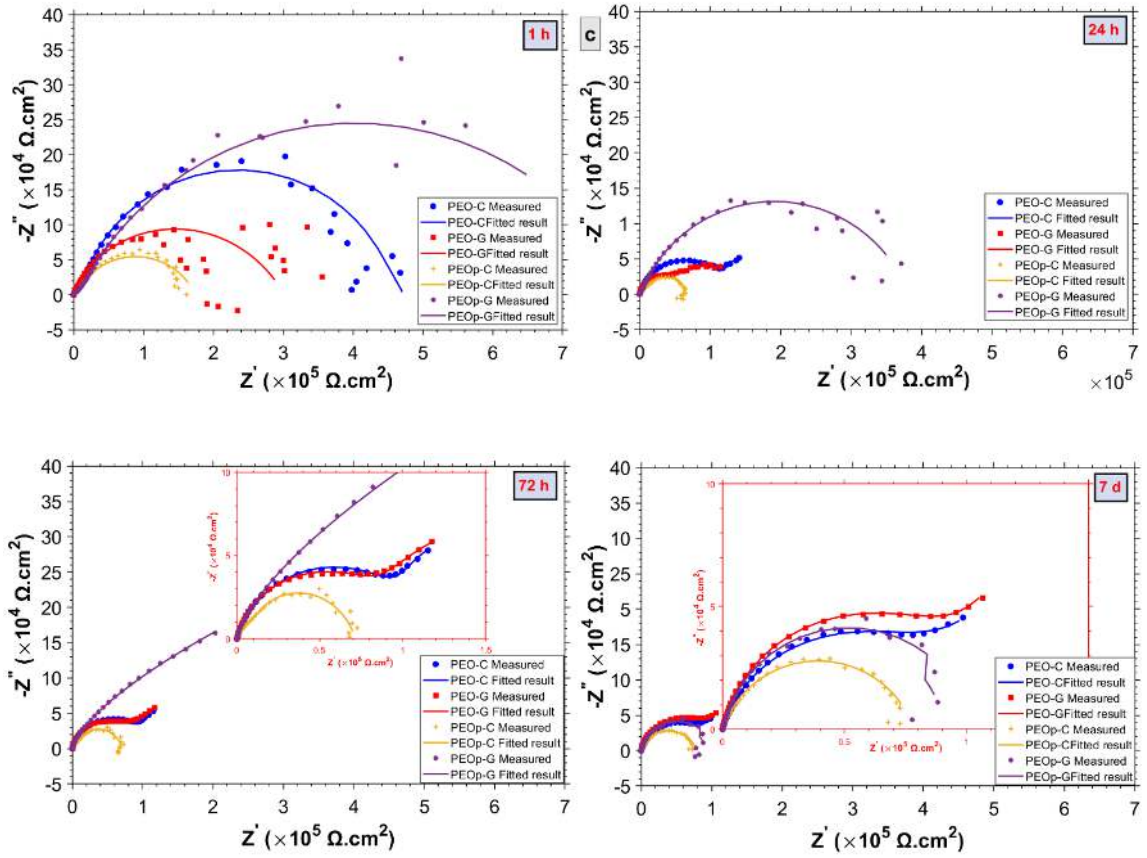

Figure 49. Bode (a,b) and Nyquist (c) diagrams at 1 h, 24 h, 72 h, and 7 d in 3.5% NaCl.

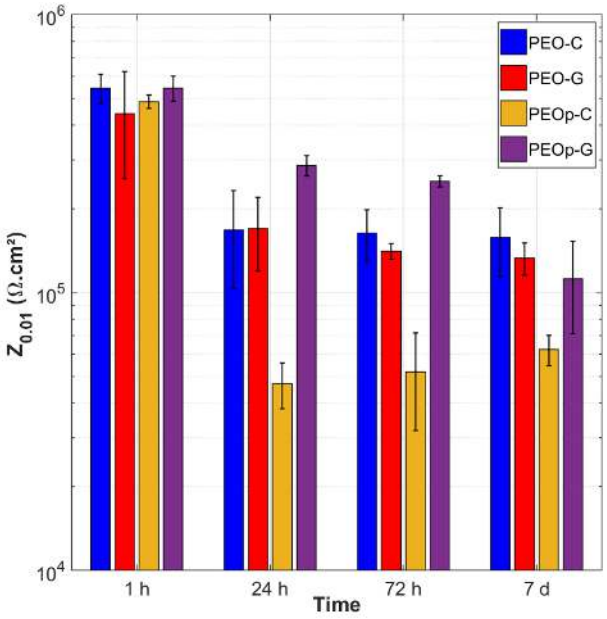

Figure 50. Impedance at 0.01 Hz for PEO and PEOp coatings in various immersion times.

Table 10. Fitting results of the equivalent electrical parameters for PEO and PEOp systems.

		Immersion Time	R_{out} $\Omega.cm^2$	CPE_{out} $\Omega^{-1}.cm^{-2}.s^{\alpha}$	α_{out}	R_{in} $\Omega.cm^2$	CPE_{in} $\Omega^{-1}.cm^{-2}.s^{\alpha}$	α_{in}	R_{ct} $\Omega.cm^2$	CPE_{dl} $\Omega^{-1}.cm^{-2}.s^{\alpha}$	α_{dl}
Electrolyte	C	1 h	1.77E+02 ± 1.52E+01	2.98E-07 ± 3.65E-07	0.89 ± 0.07	7.71E+04 ± 3.89E+03	7.01E-07 ± 4.32E-07	0.79 ± 0.06	2.91E+06 ± 7.08E+05	2.33E-07 ± 3.15E-07	0.89 ± 0.10
		24 h	2.15E+04 ± 5.84E+03	3.19E-06 ± 6.62E-07	0.84 ± 0.02	7.17E+04 ± 5.12E+04	1.99E-06 ± 1.88E-06	0.87 ± 0.06	1.38E+05 ± 1.78E+04	1.15E-04 ± 1.06E-04	0.83 ± 0.08
		72 h	1.70E+03 ± 1.01E+03	4.96E-06 ± 1.43E-06	0.81 ± 0.05	8.22E+04 ± 4.30E+04	4.22E-06 ± 3.17E-06	0.79 ± 0.03	1.48E+05 ± 2.58E+04	1.70E-04 ± 1.05E-04	0.70 ± 0.30
		7 d	5.74E+02 ± 8.78E+01	1.16E-05 ± 2.47E-06	0.82 ± 0.06	1.01E+05 ± 7.18E+03	5.91E-06 ± 3.12E-06	0.88 ± 0.03	1.19E+05 ± 2.16E+04	3.20E-04 ± 2.77E-04	0.90 ± 0.10
	G	1 h	1.34E+02 ± 8.58E+01	5.03E-07 ± 5.17E-07	0.82 ± 0.02	3.09E+04 ± 2.59E+03	5.73E-07 ± 1.83E-07	0.77 ± 0.09	7.70E+05 ± 3.10E+05	2.90E-07 ± 2.62E-07	0.90 ± 0.10
		24 h	8.87E+01 ± 9.95E+00	3.29E-06 ± 2.21E-06	0.83 ± 0.02	1.07E+05 ± 6.76E+04	1.19E-05 ± 1.95E-05	0.71 ± 0.30	3.96E+05 ± 4.19E+04	6.18E-05 ± 2.42E-05	0.87 ± 0.09
		72 h	2.66E+01 ± 9.43E+00	1.47E-06 ± 1.32E-06	0.86 ± 0.02	1.15E+05 ± 4.81E+03	7.74E-06 ± 1.16E-06	0.84 ± 0.02	1.52E+05 ± 4.30E+04	1.59E-04 ± 2.23E-05	0.75 ± 0.21
		7 d	2.08E+01 + 4.38E+00	9.43E-07 ± 3.27E-07	0.86 ± 0.01	1.13E+05 ± 4.17E+02	1.40E-05 ± 2.69E-06	0.86 ± 0.04	1.34E+05 ± 1.74E+04	3.14E-04 ± 4.38E-05	0.90 ± 0.08
Suspension	C	1 h	5.69E+02 ± 1.24E+02	1.48E-06 ± 1.40E-06	0.67 ± 0.02	1.00E+05 ± 7.13E+04	9.36E-07 ± 6.66E-07	0.78 ± 0.11	1.85E+05 ± 1.04E+05	1.06E-06 ± 8.97E-07	0.90 ± 0.01
		24 h	1.25E+02 ± 3.01E+01	1.86E-06 ± 2.07E-06	0.76 ± 0.05	1.58E+04 ± 7.63E+03	3.32E-06 ± 1.71E-06	0.76 ± 0.01	4.24E+04 ± 5.24E+03	1.90E-05 ± 2.83E-05	0.84 ± 0.06
		72 h	4.54E+02 ± 1.15E+02	4.42E-06 ± 1.59E-06	0.81 ± 0.04	1.85E+04 ± 8.35E+03	5.45E-06 ± 3.26E-06	0.80 ± 0.04	4.22E+04 ± 1.05E+04	2.27E-05 ± 2.55E-05	0.90 ± 0.06

	Immersion Time	R_{out} $\Omega.cm^2$	CPE_{out} $\Omega^{-1}.cm^{-2}.s^{\alpha}$	α_{out}	R_{in} $\Omega.cm^2$	CPE_{in} $\Omega^{-1}.cm^{-2}.s^{\alpha}$	α_{in}	R_{ct} $\Omega.cm^2$	CPE_{dl} $\Omega^{-1}.cm^{-2}.s^{\alpha}$	α_{dl}
G	7 d	4.18E+02 ± 1.10E+02	9.87E-06 ± 4.39E-06	0.80 ± 0.07	2.75E+04 ± 3.23E+03	5.10E-06 ± 7.88E-07	0.82 ± 0.06	4.00E+04 ± 6.80E+03	9.71E-06 ± 3.94E-06	0.95 ± 0.07
	1 h	1.60E+02 ± 1.01E+02	6.64E-07 ± 6.84E-07	0.66 ± 0.02	5.85E+05 ± 3.29E+05	2.28E-06 ± 1.98E-06	0.71 ± 0.08	7.15E+05 ± 3.43E+05	1.89E-06 ± 2.30E-06	0.89 ± 0.01
	24 h	3.03E+02 ± 2.38E+02	3.84E-06 ± 4.21E-06	0.78 ± 0.07	1.95E+04 ± 1.93E+03	3.88E-06 ± 3.21E-06	0.81 ± 0.06	2.07E+05 ± 1.45E+05	1.39E-05 ± 2.12E-05	0.85 ± 0.01
	72 h	5.17E+02 ± 3.19E+02	9.42E-06 ± 1.67E-06	0.81 ± 0.06	1.89E+05 ± 2.24E+04	5.70E-06 ± 6.60E-06	0.82 ± 0.04	2.02E+05 ± 1.23E+05	1.74E-05 ± 1.97E-05	0.80 ± 0.20
	7 d	4.86E+02 ± 1.55E+02	7.79E-06 ± 4.81E-06	0.85 ± 0.04	1.82E+04 ± 1.02E+04	6.22E-06 ± 3.52E-06	0.85 ± 0.04	8.32E+04 ± 5.46E+04	7.23E-06 ± 4.22E-06	0.90 ± 0.05

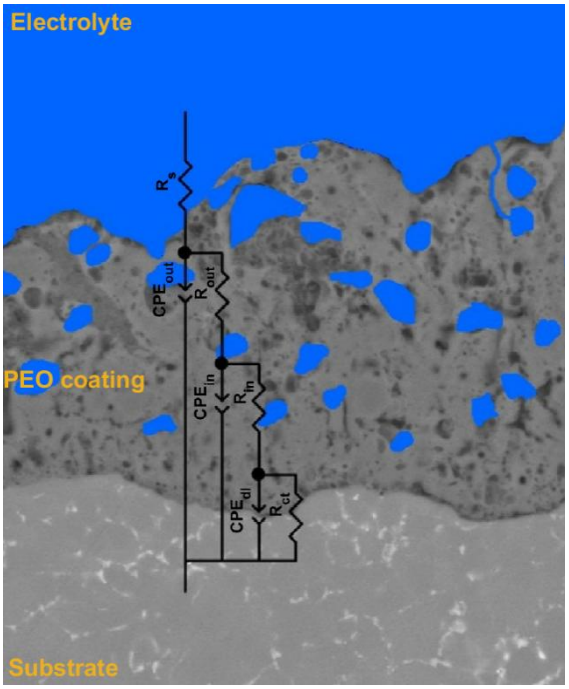

Figure 51. Schematic diagram of the electrochemical equivalent circuit to fit the EIS results.

6.3. Polarization behavior

The potentiodynamic polarization results obtained using the Tafel extrapolation method are summarized in Table 11, which shows the corrosion potentials (E_{corr}), polarization resistances (R_p), and corrosion current densities (i_{corr}) for samples after 1 hour and 7 days of immersion in 3.5% NaCl solution. Figure 52 displays the polarization curves for the PEO coatings on AlSi12Cu1(Fe) alloy after 1 hour of immersion. All coatings had corrosion potentials near −0.60 V vs. Ag/AgCl, indicating similar thermodynamic tendencies toward corrosion, but their polarization behaviors differed. The PEOp-C samples showed a significantly lower corrosion current density (Table 11). Both PEOp-C and PEOp-G coatings exhibited reduced i_{corr} and higher R_p compared to PEO coatings. Incorporating strontium silicate particles in the outer porous layer improved short-term (1h) barrier properties during the first hour of immersion.

Figure 53 demonstrates the polarization curves after 7 days of immersion. Compared to the 1h results, all coatings exhibited a shift in E_{corr} to more negative values, indicating increased surface activation with time exposure. The PEOp coatings showed the most significant changes in corrosion current density (Table 11), along with decreasing polarization resistance. Relative to 1 h, Rp increased by ~ 36% for PEO-C and ~ 171% for PEO-G, likely due to pore blocking by corrosion products. In contrast, the PEOp coatings lost protective performance over time; Rp decreased by ~ 90% for PEOp-C and ~ 82% for PEOp-G between 1 hour and 7 days. This decrease is closely linked to the microstructural characteristics of the PEOp coatings, as confirmed by EIS measurements. From Tafel analysis, the PEO coatings exhibit more stable behavior (Figure 54), with PEO-C showing the lowest corrosion current density among all samples after 7 days of immersion, making it the best long-term corrosion resistance.

Table 11. Potentiodynamic polarization data extrapolated from the Tafel analysis of the results shown in Figure 51 and Figure 52.

Immersion time	Sample	E_{corr} (V vs Ag/AgCl)	i_{corr} (µA.cm^{-2})	R_p (kΩ.cm^2)
1h	PEO-C	-0.594 ± 0.011	0.029 ± 0.017	497 ± 76.4
	PEO-G	-0.622 ± 0.009	0.053 ± 0.028	133 ± 42.8
	PEOp-C	-0.620 ± 0.011	0.009 ± 0.006	1290 ± 708
	PEOp-G	-0.613 ± 0.025	0.026 ± 0.005	708 ± 340
7 days	PEO-C	-0.714 ± 0.035	0.042 ± 0.014	675 ± 186
	PEO-G	-0.773 ± 0.022	0.068 ± 0.007	361 ± 66.1
	PEOp-C	-0.754 ± 0.067	0.169 ± 0.138	123 ± 49.0
	PEOp-G	-0.724 ± 0.031	0.126 ± 0.116	130 ± 42.6

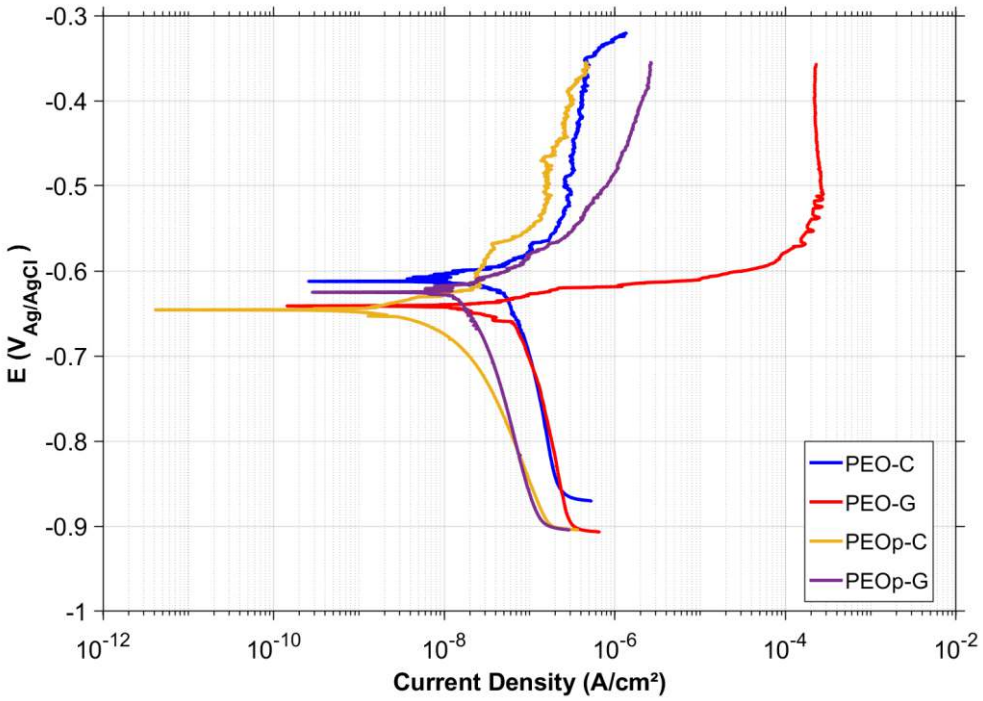

Figure 52. Potentiodynamic polarization curves carried out in a corrosive 3.5% NaCl solution after 1 h.

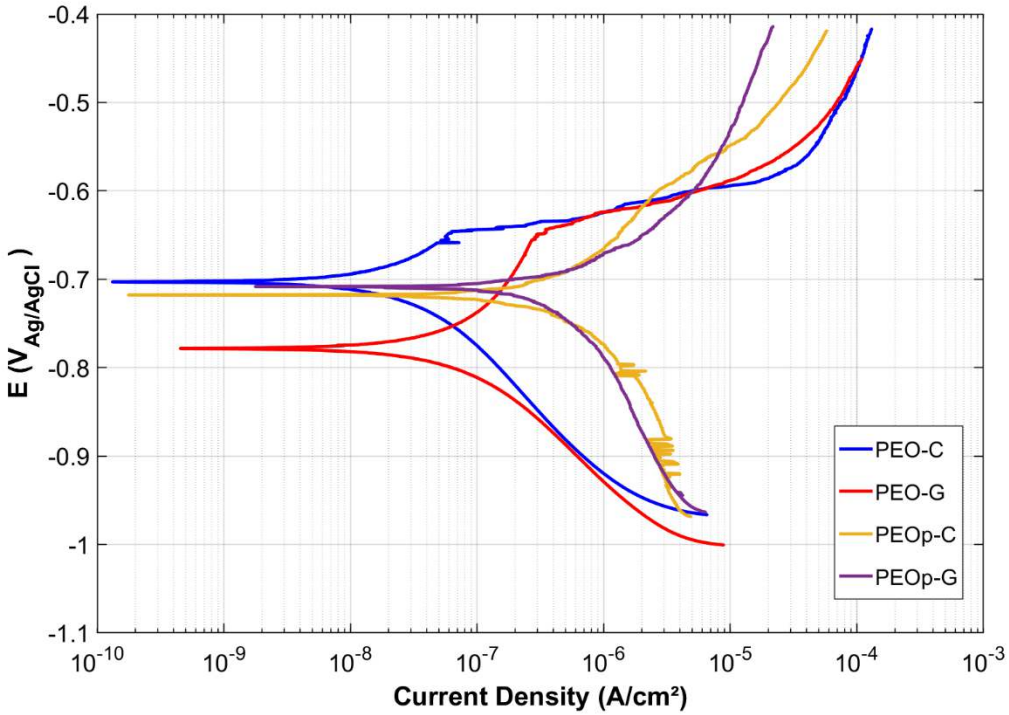

Figure 53. Potentiodynamic polarization curves carried out in a corrosive 3.5% NaCl solution after 7 d.

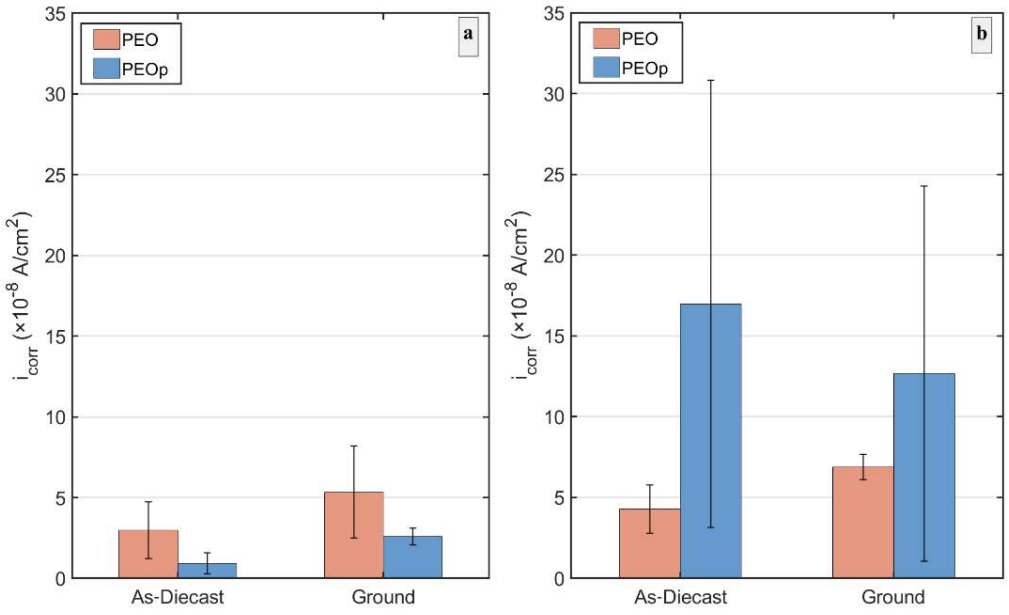

Figure 54. Corrosion Current Density of PEO and PEOp Coatings After (a) 1 h and (b) 7 d of Exposure.

Figure 55 illustrates cross-sections of the coated samples after the PDP corrosion test, performed after 7 days of immersion in 3.5% NaCl. In a NaCl solution, chloride ions penetrate through defects or channels that remain open and reach the coating/substrate interface, where

interfacial corrosion is initiated; subsequently, a localized corrosion cell develops beneath the coating. EDS reveals a higher concentration of Cl in the corrosion cell regions, as illustrated in Figure 55 for the PEO and PEOp coated samples. When the chloride ions reach the coating/substrate interface, the corrosion can progress more depending on the microstructure of the substrate in those regions.

Silicon plays a critical role in how cast Al–Si alloys resist corrosion, with its impact driven more by the shape and continuity of the Si phase than by its amount [170,171]. In NaCl environments, microcracks and pores in the PEO coating allow electrolyte to seep through, reaching the interface between the coating and the underlying substrate. When this interface contains silicon particles or a continuous silicon network in contact with the α-Al matrix, a galvanic cell forms. This happens because α-Al has a much lower electrochemical potential than silicon. In this setup, the α-Al acts as the anode and corrodes, while the silicon serves as the cathode and remains protected. This process leads to the formation of corrosion products such as $Al(OH)_3$, $Al(OH)_2Cl$, $AlOHCl_2$, and $AlCl_3$. Consequently, localized corrosion tends to develop at the α-Al around Si particles [172,173].

Figure 55d illustrates the EDS line analysis; the higher Cl content is observed between points 1 and 2, where the corrosion is clearly visible. At the same time, the region between points 1 and 2 has lower silicon content than the region after point 2. Generally, we can notice that the corrosion cells formed in the underlying substrate contain a higher amount of Cl and a lower amount of Si. The cross-sectional schema of the PEO coatings during the corrosion process is illustrated in Figure 56.

Figure 57 shows the EDS map for the cross-section of the PEOp-G coating. The elemental distributions reveal a localized enrichment of Cl within the localized corrosion cell, following the preferential pathway. This localized corrosion cell is located in the region containing cavities and propagates into the substrate, predominantly within areas enriched in α-Al.

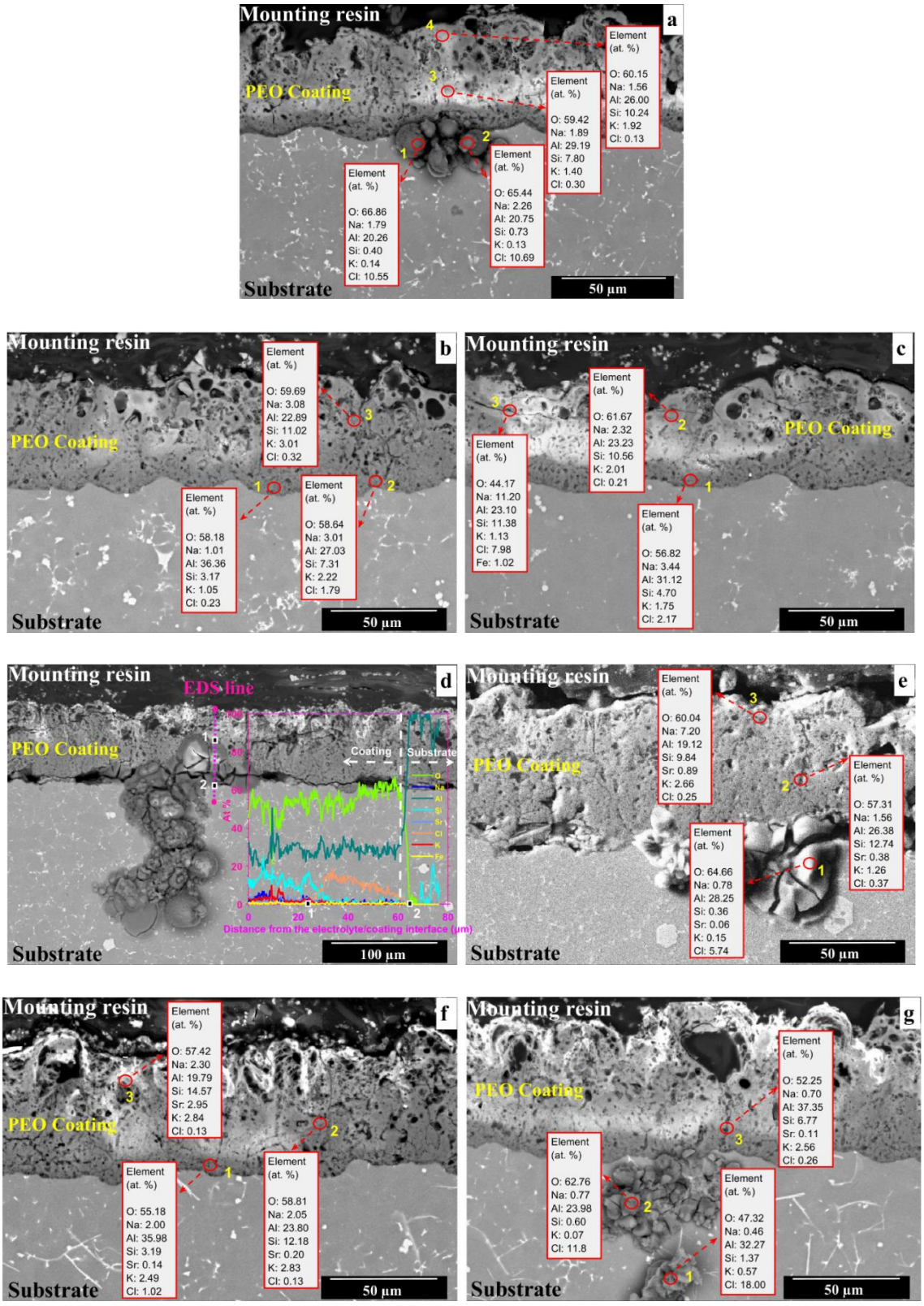

Figure 55. SEM cross-section images of the studied coatings after PDP corrosion test: (a,b,c) PEO and (d,e,f,g) PEOp when the initial surface is (a,b,d,f) as-diecast and (c,e,g) ground.

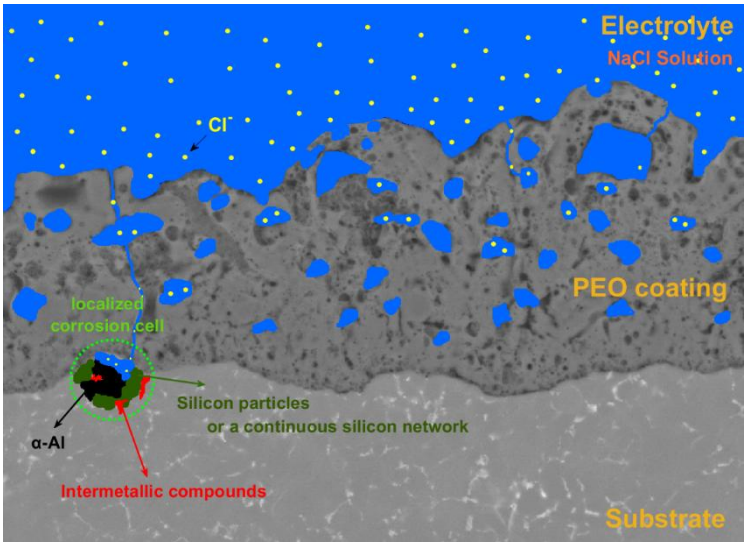

Figure 56. Schematic cross-section illustrates the PEO coating during corrosion and the formation of a localized corrosion cell.

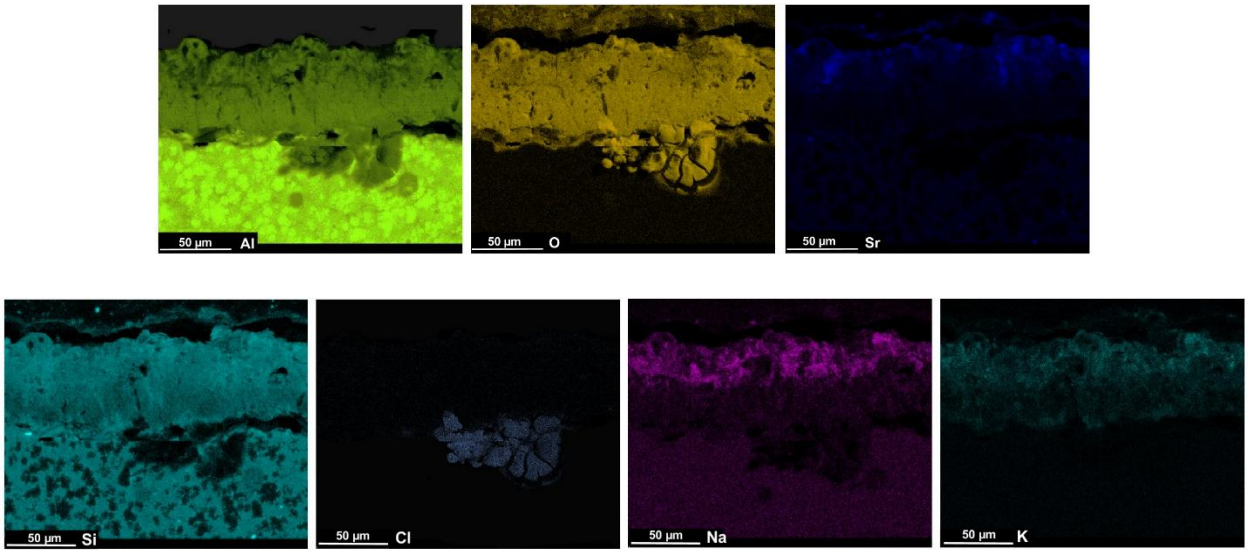

Figure 57. EDS maps showing localized corrosion in the cross-section of PEOp-G coating.

6.4. Summary

This study thoroughly examined the corrosion resistance of PEO and PEOp coatings formed on die-cast AlSi12Cu1(Fe) alloy. The main results can be summarized as follows:

- PEOp coatings have better corrosion performance after 1h immersion in 3.5% NaCl solution and have lower corrosion current density than PEO coatings.
- EIS results indicated that the Resistance of the outer layer (R_{out}) of the PEOp coatings has a higher value than the corresponding PEO coatings for as-diecast and ground surfaces. These results indicate that the presence of Sr_2SiO_4 in the outer layer does not degrade its resistance.
- Presence of suspended strontium aluminate particles in the electrolyte seems to be affect on the process of forming the coating. While the formation of Sr_2SiO_4 enhances wear performance and outer layer integrity, defects and cavities in the inner layer increase. This is witnessed from the cross-section and EIS results, especially the R_{in} resistance.
- After 72h immersion, the $Z_{0.01}$ for PEOp coatings sharply decreases due to penetration of the NaCl solution into the cracks and channels that remain open, as indicated by R_{in} results. In contrast, PEO coatings maintain a relatively stable $Z_{0.01}$ value after 24h, 72h, and 7 days.
- Increasing the corrosion current density of PEOp reveals the important effects of inner layer integrity in protecting the substrate, also raises an open question for trying to enhance the PEO process to combine a good outer and inner layer integrity.

7. Claims

Claim 1. The initial surface microstructure of the HPDC Al12Si1Cu(Fe) alloy affects the growth of the anodic layer and its tribological performance.

1.a. The ground surface with a higher α-Al phase contributed to enhancing the anodic layer thickness. The ground surface, serving as the initial substrate before anodizing, significantly increases the thickness of the anodic layer in both traditional and hard anodizing methods. Despite differences in parameters and anodic layer growth rates during anodizing, the microstructural changes from the as-diecast to the ground state show a significant increase in the α-Al phase. As shown in Figure C1.1, the anodic layer formed through traditional anodizing is about 3 times thicker than that on the anodized as-diecast surface. In contrast, for hard anodizing, the anodic layer is roughly 1.3 times thicker than that on the anodized as-diecast surface. This difference mainly results from the higher silicon content at the as-diecast surface, which hinders oxide layer growth. Additionally, the hard-anodized ground surface exhibits a 36% increase in average coating thickness compared to the hard-anodized as-cast surface, while traditional anodizing shows an impressive 200% increase. These results highlight the crucial role of surface microstructure in enhancing anodic layer thickness.

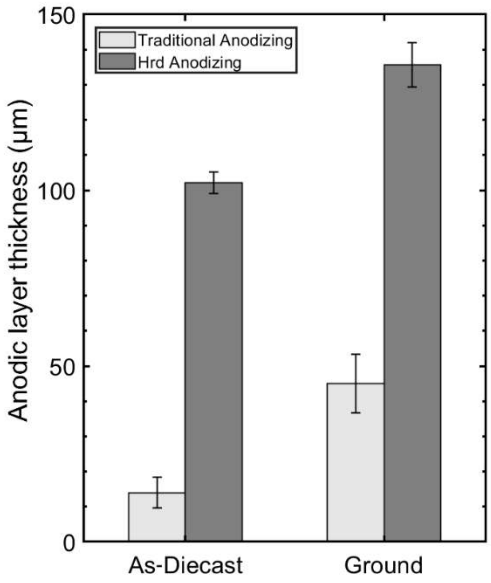

Figure C1.1. Variation of the thickness of the anodized layers.

1.b. Increasing the anodic layer thickness is inversely proportional to the wear rate. The wear resistance of the anodic oxide layer is greatly affected by its microstructure and overall integrity. In this study, the anodized ground surfaces had a thicker anodic layer; however, this layer had a higher density of cavities. These cavities are linked to the surface microstructure before anodizing, as grinding exposes a microstructure with coarser silicon eutectic particles compared to the as-diecast microstructure. Conversely, the as-diecast surface features a finer silicon eutectic structure, which helps the oxide/metal interface during anodic film growth to engulf eutectic Si particles more effectively. This engulfment process becomes less efficient with larger Si particles, leading to the formation of cavities primarily near the Si particles.

Additionally, the uniform distribution of fine silicon eutectic within the anodic layer enhances wear performance. This microstructural feature improves wear resistance and reduces the wear rate, as observed for both hard and conventional anodic layers formed on anodized as-die-cast surfaces.

Claim 2. The initial surface microstructure of the HPDC Al12Si1Cu(Fe) alloy does not significantly affect the growth of the PEO coating; however, it does impact its tribological performance.

2.a. The initial ground surface with a higher α-Al phase exhibits the same PEO coating growth as the as-cast surface. In this study, the average PEO coating growth ($\mu m \cdot min^{-1}$) developed under high frequency (400 Hz) in (7.5 ml $Na_2O(SiO_2)_x.xH_2O$, ≥27% SiO_2 and 2.8 $gr \cdot l^{-1}$ KOH) electrolyte has the same coating growth (~2.1 $\mu m \cdot min^{-1}$) regardless of the initial surface microstructure. pEO treatment reduced the negative effects of silicon in hindering oxide growth, enabling a similar PEO coating thickness on both as-diecast and ground surfaces. This is because the energy supplied by the PEO process was sufficient to oxidize Si eutectic particles.

2.b. The initial microstructure, featuring a higher α-Al phase, contributed to the formation of a better wear-resistant PEO coating. In contrast to the anodizing process, the presence of a higher amount of Si eutectic particles in the initial surface was found to reduce the wear rate in the PEO coatings. This behaviour can be attributed to differences in the initial surface microstructure. Specifically, the ground surface condition, which contains a higher fraction of α-Al, promoted the formation of a coating with increased microhardness. This enhancement is

associated with a higher γ-Al_2O_3 content in the coating, which contributes to improved overall wear resistance. As shown in Figure C2.1, the PEO coating formed on the ground surfaces (PEO-G) exhibited a lower wear rate compared with the coating formed on the as-die-cast surfaces (PEO-C). Furthermore, statistical analysis confirms that the observed difference in wear rate between PEO-C and PEO-G coatings is statistically significant.

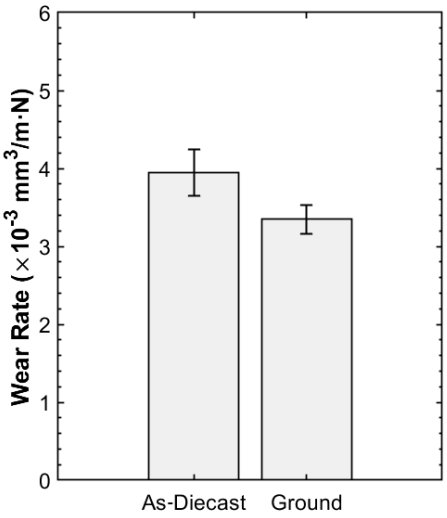

Figure C2.1. Wear rate variation of PEO coating on as-diecast and ground AlSi12Cu1(Fe) alloy substrates.

Claim 3. Strontium aluminate particles suspended in the silicate-based electrolyte are reactively incorporated into the PEO coating.

3.a. Silicate-based electrolyte promotes the formation of the Sr_2SiO_4 phase instead of the $SrAl_2O_4$ phase. $SrAl_2O_4$ underwent thermal decomposition under the high-energy micro-arcs, and due to the process in the silicate electrolyte, the SrO will rapidly react with the silicate: The formation of Sr_2SiO_4 has higher thermodynamic stability than the formation of strontium aluminate ($SrO{\cdot}Al_2O_3$) from SrO and Al_2O_3. XRD patterns confirmed the presence of Sr_2SiO_4 in the PEO coating.

3.b. The Sr_2SiO_4 phase contributed to enhancing the tribological properties of the PEOp coating. The reactive incorporation of $SrAl_2O_4$ particles during the PEO process and the subsequent formation of Sr_2SiO_4 within the outer porous layer significantly enhanced the tribological performance of the PEOp coating compared to the conventional PEO coating. This reactive incorporation also increased the microhardness of the outer porous layer by consuming

SiO_2, thereby reducing its negative impact on coating hardness. As shown in Figure C3.1a, the conventional PEO coating had a greater wear-scar depth than the PEOp coating. This suggests that, under the tested wear conditions, the counter-body penetrated deeper into the PEO coating, while for PEOp coatings, the wear track stayed within the outer porous layer. As a result, PEOp coatings exhibited the lowest wear rates and the most stable friction coefficients. This improved behavior was consistently observed for both initial surface conditions tested, with PEOp coatings showing a reduced wear rate than the corresponding PEO coatings. Furthermore, the decrease in wear rate shown in Figure 4b is very statistically significant.

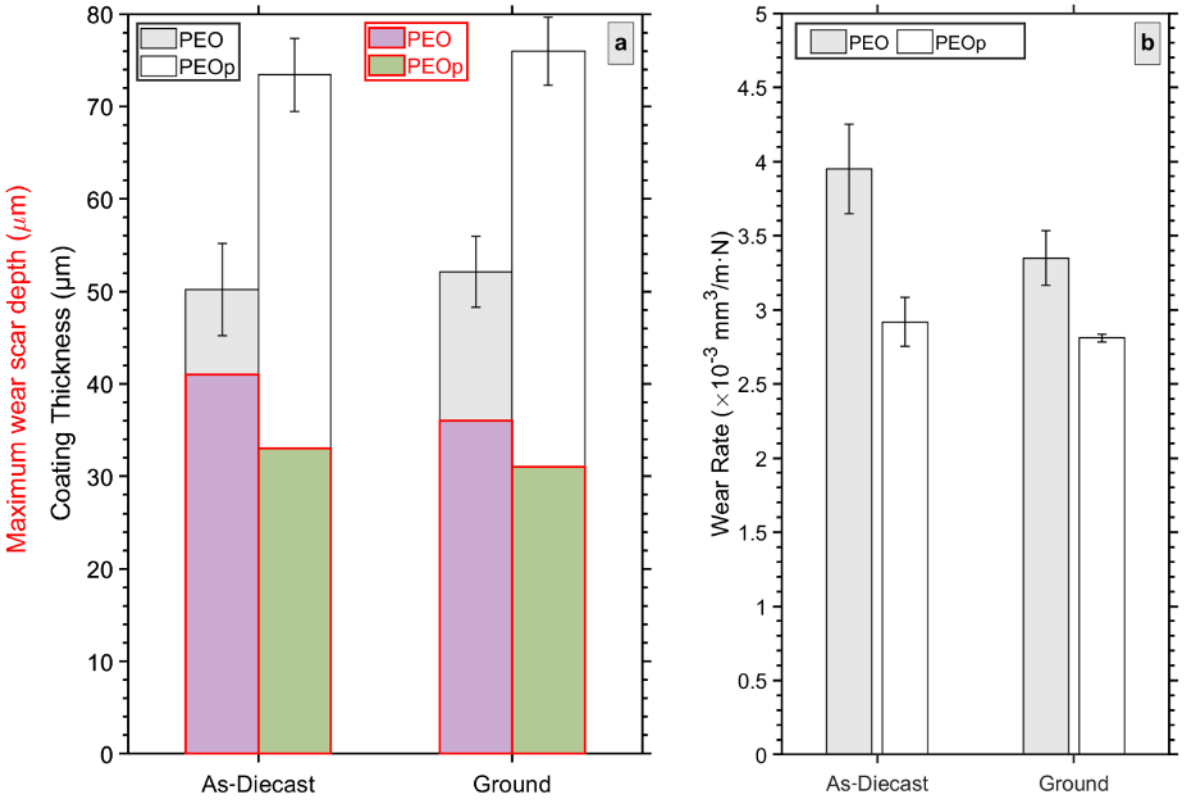

Figure C3.1. PEO and PEOp coatings properties, (a) thickness and wear scar depth and (b) wear rate.

3.c. Minimal Influence of Substrate on PEOp Tribological Performance. The optimized PEOp coatings exhibit excellent wear resistance regardless of whether the substrate surface is as-cast or ground. The difference in wear rate between PEOp-C and PEOp-G coatings is not statistically significant, unlike PEO-C and PEO-G coatings (Figure C3.1).

Claim 4. Corrosion resistance of PEO-coated samples of HPDC AlSi12Cu1(Fe) alloy is governed primarily by the integrity of the PEO coating.

4.a. The outer porous layer does not control the long-term corrosion resistance. At low frequency voltages, the polarization pathway occurs through the resistors, both the electric double layer (EDL) capacitance and coating capacitances behave effectively as open circuits. Therefore, the impedance magnitude at low frequency $Z_{0.01\ Hz}$ can be considered an indicator of the overall resistance to ionic transport through the coating. From the obtained fitting results and the equivalent circuit, R_{out}, R_{in}, and R_{ct} are in series, so we can estimate the contributions of the inner and outer layers to corrosion resistance. The highly porous outer layer does not significantly increase the impedance at low frequency. As shown in Figure C4.1, even when particles are incorporated into the outer layer and porosity is partially reduced, no improvement in overall coating resistance is observed after 7 days of immersion.

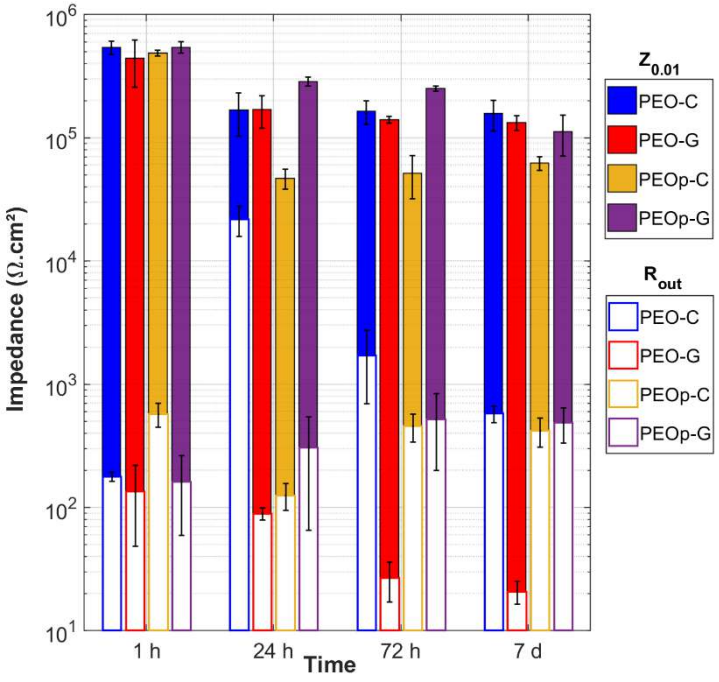

Figure C4.1. Impedance magnitude at 0.01 Hz ($Z_{0.01}$) and outer layer resistance (R_{out}) for PEO and PEOp coatings at different immersion times in 3.5% NaCl.

1.b. The inner layer is the critical barrier layer that controls corrosion resistance. The inner layer serves as the critical barrier, controlling corrosion resistance by restricting transport and limiting electrolyte penetration. Its protective performance evolves with immersion time and

depends strongly on its microstructural integrity. Figure C4.2 indicates that the inner layer resistance is initially higher for particle-modified coatings (PEOp) after 1 h of immersion, likely due to the outer layer contribution in limiting electrolyte penetration. However, after 7 days of immersion, electrolyte ingress reaches the inner layer, leading to a reduction in Rin for PEOp coatings, whereas PEO coatings exhibit a relatively stable performance.

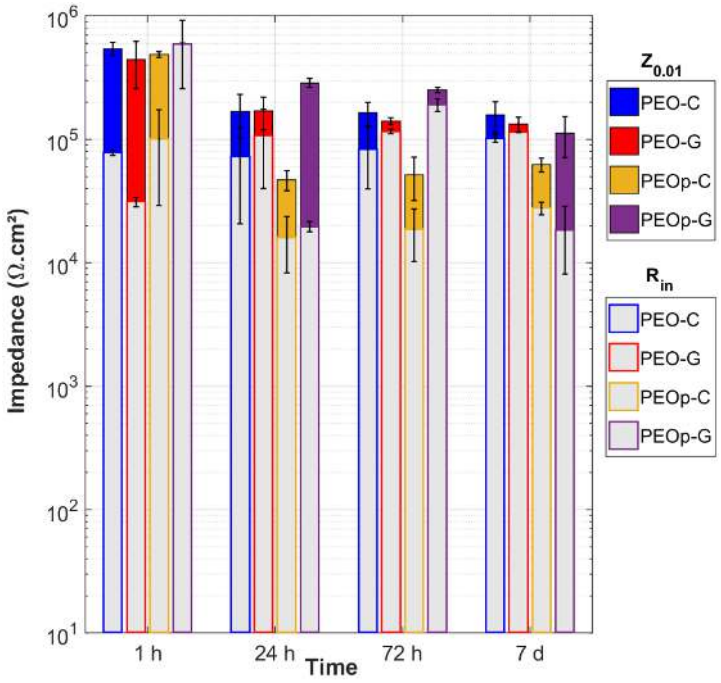

Figure C4.2. Impedance magnitude at 0.01 Hz ($Z_{0.01}$) and inner layer resistance (R_{in}) for PEO and PEOp coatings at different immersion times in 3.5% NaCl.

Claim 5. $SrAl_2O_4$ particles-assisted PEO coatings (PEOp) on HPDC AlSi12Cu1(Fe) alloy have better short-term (1h) corrosion resistance than PEO coatings (without particles).

5.a. Existence of Sr_2SiO_4 in the outer porous layer enhances polarization resistance of the coating. Sr_2SiO_4 partially seals pores and discharge channels, thereby diminishing electrolyte penetration into the inner layer and increasing polarization resistance relative to PEO by as much as 160% when the initial surface is as-diecast and 430% when ground, as illustrated in Figure 16.

5.b. polarization resistance Rp of the PEOp coatings decreases after 7 days of immersion in 3.5% NaCl. Increasing immersion time allows chloride ions to penetrate through remaining microcracks and reach the inner layer and defects near the coating/substrate. This leads to localized

corrosion beneath the coating, breakdown of the inner barrier layer, and a gradual decrease in polarization resistance for PEOp coatings, this difference is considered to be statistically significant. In contrast, PEO coatings exhibit enhanced polarization resistance because the corrosion products seal the pores and cracks, which are smaller than those found in PEOp coatings. this difference is considered to be very statistically significant for PEOp-G and not statistically significant for PEOp-C (Figure C.5.1).

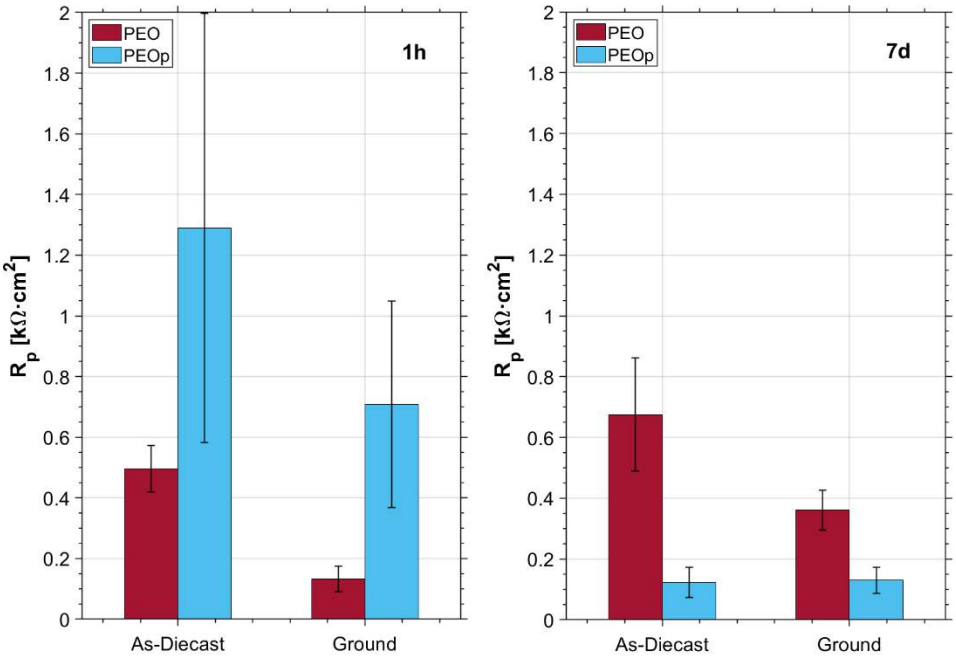

Figure C5.1. Polarization resistance Rp of PEO and PEOp Coatings After 1 h and 7 d of Exposure.

8. Scientific publications

Publications related to the subject of the dissertation

1- Razzouk, Emel, Itziar Hidalgo-González, Dániel Koncz-Horváth, Endzhe Matykina, Raúl Arrabal, and Tamás István Török. "In-situ formation of Sr_2SiO_4 composite PEO coatings on HPDC AlSi12Cu1 (Fe) alloy for enhanced wear resistance and energy efficiency." *Surface and Coatings Technology* (2025): 132790. Independent citation: 1. *Journal Rank: Q1*

2- Razzouk, Emel, Dániel Koncz-Horváth, and Tamás I. Török. "Critical Challenges in the Anodizing Process of Aluminium–Silicon Cast Alloys—A Review." *Crystals* 14, no. 7 (2024): 617. Independent citation: 8. *Journal Rank: Q2*

3- Razzouk, Emel, Dániel Koncz-Horváth, and Tamás I. Török. "Microstructure Effects on Anodizing High-Silicon Aluminium Alloy AlSi12Cu1 (Fe) under Various Surface Conditions and Power Modes." *Crystals* 14, no. 4 (2024): 352. Independent citation: 7. *Journal Rank: Q2*

4- Emel Razzouk, Tamás Kurusta, Ádám Rácz, Dániel Koncz-Horváth, and Tamás I. Török. Fabrication of Strontium Aluminate Suspension and Its Incorporation into PEO Coating on HPDC Al-Si Alloy. Doktorandusz Almanach 2025.

5- Razzouk Emel, Dániel Koncz-Horváth, Tamás I. Török, Influence of Surface Preparation on the Wear Performance and Microstructurl Properties of Anodized Al-Si Die-Cast Alloy. Doktorandusz Almanach 2024.

6- Razzouk Emel, Dániel Koncz-Horváth, Tamás I. Török. Anodizing Challenges in High-Silicon Aluminum Alloy AlSi12Cu1(Fe): Microstructural Impact and Thickness Variation under Different Surface Conditions and Power Modes**.** 27th International Student Day of Metallurgy, Freiberg, Germany (2024).

7- Razzouk Emel, Dániel Koncz-Horváth, Tamás I. Török. Anodic film changes during anodizing commercial pure aluminum, Doktorandusz Almanach 2023 : 1 pp. 34-40. , 7 p. (2023).

8- Emel Razzouk, Tamás I Török. A review of plasma electrolytic oxidation coating characteristics and affecting factors, Doktorandusz Almanach 1 pp. 295-306. 12 p. (2022).

Further Publications

1- Nagy, Mónika Fekete, Dániel Koncz-Horváth, István Kern, Emel Razzouk, and Tamás I. Török. "Coprecipitation and Properties of Conversion Nano-layers Formed on Steel Plates during Iron Phosphating with Molybdate and Magnesium Nitrate Additives." *Journal of Materials Engineering and Performance* (2026): 1-10. *Journal Rank: Q2*

Conference presentations

1- 27th Spring Wind Conference

Oral presentation. Budapest, Hungary (3-5 May 2024).

The Role of Microstructure in Anodizing Behavior of High-Silicon Aluminium Alloy AlSi12Cu1(Fe).

2- 27th International Student Day of Metallurgy

Oral presentation. Freiberg, Germany (10-12 April 2024).

Anodizing Challenges in High-Silicon Aluminum Alloy AlSi12Cu1(Fe): Microstructural Impact and Thickness Variation under Different Surface Conditions and Power Modes.

3- Materials Science Day XXIII for PhD Students

Oral presentation. Pannon Egyetem (20. November. 2023).

Challenges Associated with Anodizing Casting Al-Si Alloy.

4- ESTAL 2023 Congress,

Oral presentation. Budapest (27-29 September 2023).

Anodizing and plasma electrolytic oxidation of casting Al-Si alloys.

5- Hungarian Science Day conference

Oral presentation. Miskolc, Hungary, (10. November. 2022).

A review of plasma electrolytic oxidation coating characteristics and affecting factors.

9. References

[1]- W. Lee and S.-J. Park. "Porous Anodic Aluminum Oxide: Anodization and Templated Synthesis of Functional Nanostructures." *Chemical Reviews* 114, no. 15 (2014): 7487–7556. https://doi.org/10.1021/cr500002z.

[2]- J. M. Runge. The Metallurgy of Anodizing Aluminum. Cham: *Springer International Publishing*, 2018. https://doi.org/10.1007/978-3-319-72177-4.

[3]- B. Zhu and C. Zanella. "Influence of Fe-Rich Intermetallics and Their Segregation on Anodising Properties of Al–Si–Mg Rheocast Alloys." *Surface and Coatings Technology* 422 (2021): 127570. https://doi.org/10.1016/j.surfcoat.2021.127570.

[4]- E. Razzouk, D. Koncz-Horváth, and T. I. Török. "Critical Challenges in the Anodizing Process of Aluminium–Silicon Cast Alloys—A Review." (2024). *Crystals* 14, no. 7 (2024): 617. https://doi.org/10.3390/cryst14070617.

[5]- N. Barati, E. I. Meletis, F. Golestani Fard, A. Yerokhin, S. Rastegari, and M. A. Faghihi-Sani. "Al_2O_3–ZrO_2 Nanostructured Coatings Using DC Plasma Electrolytic Oxidation to Improve Tribological Properties of Al Substrates." *Applied Surface Science* 356 (2015): 927–934. https://doi.org/10.1016/j.apsusc.2015.08.188.

[6]- A.L. Yerokhin, X. Nie, A. Leyland, A. Matthews, and S. J. Dowey. "Plasma Electrolysis for Surface Engineering." *Surface and Coatings Technology* 122, no. 2–3 (1999): 73–93. https://doi.org/10.1016/S0257-8972(99)00441-7.

[7]- X. Lu, M. Mohedano, C. Blawert, E. Matykina, R. Arrabal, K. U. Kainer, and M. L. Zheludkevich. "Plasma Electrolytic Oxidation Coatings with Particle Additions—A Review." *Surface and Coatings Technology* 307 (2016): 1165–1182. https://doi.org/10.1016/j.surfcoat.2016.08.055.

[8]- M. Rizwan, R. Alias, U. Z. Zaidi, R. Mahmoodian, and M. Hamdi. "Surface Modification of Valve Metals Using Plasma Electrolytic Oxidation for Antibacterial Applications: A Review." *Journal of Biomedical Materials Research Part A* 106, no. 2 (2018): 590–605. https://doi.org/10.1002/jbm.a.36259.

[9]- B. L. Jiang and Y. M. Wang. "Plasma Electrolytic Oxidation Treatment of Aluminium and Titanium Alloys." In *Surface Engineering of Light Alloys*, 110–154. Elsevier, 2010. https://doi.org/10.1533/9781845699451.2.110.

[10]- V. F. Henley. *Anodic Oxidation of Aluminium and Its Alloys (The Pergamon Materials Engineering Practice Series).* Amsterdam: Elsevier, 2013.

[11]- J. R. Brown, ed. *Foseco Non-Ferrous Foundryman's Handbook,* 11th ed. Oxford; Boston: Butterworth-Heinemann, 1999.

[12]- J. G. Kaufman and E. L. Rooy. *Aluminum Alloy Castings: Properties, Processes, and Applications.* ASM International, 2004. https://doi.org/10.31399/asm.tb.aacppa.9781627083355.

[13]- T. Bogdanoff, S. Seifeddine, and A. K. Dahle. "The Effect of Si Content on Microstructure and Mechanical Properties of Al–Si Alloy." *La Metallurgia Italiana* 108, no. 6 (2016).

[14]- ASM Handbook. "Volume 15: Casting." Materials Park, OH: ASM International, 2008: 416–522.

[15]- Polmear, D. StJohn, J.-F. Nie, and M. Qian. *Light Alloys: Metallurgy of the Light Metals,* 5th ed. Amsterdam, 2017.

[16]- D. Stanić, Z. Zovko Brodarac, and L. Li. "Influence of Copper Addition in AlSi7MgCu Alloy on Microstructure Development and Tensile Strength Improvement." *Metals* 10, no. 12 (2020): 1623. https://doi.org/10.3390/met10121623.

[17]- M. T. Di Giovanni, et al. "Influence of Cu Addition on the Heat Treatment Response of A356 Foundry Alloy." *Materials Today Communications* 19 (2019): 342–348. https://doi.org/10.1016/j.mtcomm.2019.02.013.

[18]- J. Baskaran, P. Raghuvaran, and S. Ashwin. "Experimental Investigation on the Effect of Microstructure Modifiers and Heat Treatment Influence on A356 Alloy." *Materials Today: Proceedings* 37 (2021): 3007–3010. https://doi.org/10.1016/j.matpr.2020.08.719.

[19]- Y. Xu, Z. Zhang, Z. Gao, Y. Bai, P. Zhao, and W. Mao. "Effect of Main Elements (Zn, Mg and Cu) on the Microstructure, Castability and Mechanical Properties of 7xxx Series Aluminum Alloys with Zr and Sc." *Materials Characterization* 182 (2021): 111559. https://doi.org/10.1016/j.matchar.2021.111559.

[20]- Z. Fan, et al. "Grain Refining Mechanism in the Al/Al–Ti–B System." *Acta Materialia* 84 (2015): 292–304. https://doi.org/10.1016/j.actamat.2014.10.055.

[21]- İ. Öztürk, G. Hapçı Ağaoğlu, E. Erzi, D. Dispinar, and G. Orhan. "Effects of Strontium Addition on the Microstructure and Corrosion Behavior of A356 Aluminum Alloy." *Journal of Alloys and Compounds* 763 (2018): 384–391. https://doi.org/10.1016/j.jallcom.2018.05.341.

[22]- L. Kumar, J. C. Jang, H. Yu, and K. S. Shin. "Effects of Cr and Ti Addition on Mechanical Properties and Thermal Conductivity of Al–7Si–3Mg Die-Casting Alloys." *Metals and Materials International* 29, no. 1 (2023): 204–214. https://doi.org/10.1007/s12540-022-01206-8.

[23]- J. Y. Hwang, H. W. Doty, and M. J. Kaufman. "The Effects of Mn Additions on the Microstructure and Mechanical Properties of Al–Si–Cu Casting Alloys." *Materials Science and Engineering: A* 488, no. 1–2 (2008): 496–504. https://doi.org/10.1016/j.msea.2007.12.026.

[24]- X. Wang, et al. "Effect of Trace Cr Alloying on Centerline Segregations in Sub-Rapid Solidified Al–Mg–Si (AA6061) Alloys Fabricated by Twin-Roll Casting." *Materials Science and Engineering: A* 825 (2021): 141896. https://doi.org/10.1016/j.msea.2021.141896.

[25]- H. Y. Kim, S. W. Han, and H. M. Lee. "The Influence of Mn and Cr on the Tensile Properties of A356–0.20Fe Alloy." *Materials Letters* 60, no. 15 (2006): 1880–1883. https://doi.org/10.1016/j.matlet.2005.12.042.

[26]- A.M. Cardinale, D. Macciò, G. Luciano, E. Canepa, and P. Traverso. "Thermal and Corrosion Behavior of As-Cast Al–Si Alloys with Rare Earth Elements." *Journal of Alloys and Compounds* 695 (2017): 2180–2189. https://doi.org/10.1016/j.jallcom.2016.11.066.

[27]- M. Elmadagli, T. Perry, and A. T. Alpas. "A Parametric Study of the Relationship Between Microstructure and Wear Resistance of Al–Si Alloys." *Wear* 262, no. 1–2 (2007): 79–92. https://doi.org/10.1016/j.wear.2006.03.043.

[28]- F. Wang, Z. Zhang, Y. Ma, and Y. Jin. "Effect of Fe and Mn Additions on Microstructure and Wear Properties of Spray-Deposited Al–20Si Alloy." *Materials Letters* 58, no. 19 (2004): 2442–2446. https://doi.org/10.1016/j.matlet.2004.02.027.

[29]- F. C. Robles Hernandez, J. M. Herrera Ramírez, and R. Mackay. "Al–Si Alloys, Minor, Major, and Impurity Elements." In *Al–Si Alloys*, 1–15. Cham: Springer International Publishing, 2017. https://doi.org/10.1007/978-3-319-58380-8_1.

[30]- D. S.-S. Ahammed, A. A. Khan, A. A. Razin, and M. S. Kaiser. "Impact of Under-, Peak- and Over-Ageing on the Wear Properties of Si-Doped Al-Based Automotive Alloy." *Materials Today: Proceedings* 82 (2023): 300–307. https://doi.org/10.1016/j.matpr.2023.02.006.

[31]- H. R. Kotadia and A. Das. "Modification of Solidification Microstructure in Hypo- and Hyper-Eutectic Al–Si Alloys under High-Intensity Ultrasonic Irradiation." *Journal of Alloys and Compounds* 620 (2015): 1–4. https://doi.org/10.1016/j.jallcom.2014.09.089.

[32]- V. S. Zolotorevskiĭ, N. A. Belov, and M. V. Glazoff. *Casting Aluminum Alloys,* 1st ed. Oxford: Elsevier Science, 2007.

[33]- J. S. Shin, B. H. Kim, and S. M. Lee. "Effects of Physical Melt Treatments on Microstructural Evolution and Anodizing Characteristics of Al–Si Casting Alloys." *Materials Science Forum* 695 (2011): 243–246. https://doi.org/10.4028/www.scientific.net/MSF.695.243.

[34]- A. Advekar, D. Y. Arunkumar, and D. M. S. Srinath. "Simulation of High Pressure Die Casting Process for Identifying and Minimising Defects." *International Journal of Engineering Research* 3, no. 17 (2015).

[35]- J. Campbell. "Casting." In *Complete Casting Handbook*, 821–882. Elsevier, 2015. https://doi.org/10.1016/B978-0-444-63509-9.00016-9.

[36]- H. Zheng, Y. Jiang, F. Liu, and H. Zhao. "Synergistic Effect of Externally Solidified Crystals and Fe-Rich Intermetallic on the Fracture Behavior of HPDC Alloy." *Journal of Materials Research and Technology* 27 (2023): 2822–2832. https://doi.org/10.1016/j.jmrt.2023.10.167.

[37]- X. Y. Jiao, et al. "Characterization of Externally Solidified Crystals in a High-Pressure Die-Cast AlSi10MnMg Alloy and Their Effect on Porosities and Mechanical Properties." *Journal of Materials Processing Technology* 298 (2021): 117299. https://doi.org/10.1016/j.jmatprotec.2021.117299.

[38]- X. Y. Jiao, et al. "Characterization of High-Pressure Die-Cast Hypereutectic Al–Si Alloys Based on Microstructural Distribution and Fracture Morphology." *Journal of Materials Science & Technology* 35, no. 6 (2019): 1099–1107. https://doi.org/10.1016/j.jmst.2018.12.005.

[39]- J. Fu, et al. "Microstructure, Eutectic Si Distribution, and Mechanical Properties of Al–6Si–Mg High Pressure Die Castings with Long Mold Filling Distance." *Journal of Manufacturing Processes* 150 (2025): 391–406. https://doi.org/10.1016/j.jmapro.2025.06.075.

[40]- M. Zhang, K. Liu, J. Han, F. Qian, J. Wang, and S. Guan. "Investigating the Role of Cu, Zr and V on the Evolution of Microstructure and Properties of Al–Si–Mg Cast Alloys." *Materials Today Communications* 26 (2021): 102055. https://doi.org/10.1016/j.mtcomm.2021.102055.

[41]- D. Blondheim and A. Monroe. "Macro Porosity Formation: A Study in High Pressure Die Casting." *International Journal of Metalcasting* 16, no. 1 (2022): 330–341. https://doi.org/10.1007/s40962-021-00602-x.

[42]- Z.-Q. Hu, X.-J. Zhang, and S.-S. Wu. "Microstructure, Mechanical Properties and Die-Filling Behavior of High-Performance Die-Cast Al–Mg–Si–Mn Alloy." *Acta Metallurgica Sinica (English Letters)* 28, no. 11 (2015): 1344–1353. https://doi.org/10.1007/s40195-015-0332-7.

[43]- Z. W. Chen. "Skin Solidification during High Pressure Die Casting of Al–11Si–2Cu–1Fe Alloy." *Materials Science and Engineering: A* (2003). *Materials Science and Engineering: A* 348, no. 1-2 (2003): 145-153. https://doi.org/10.1016/S0921-5093(02)00747-5.

[44]- E. J. Vinarcik. *High Integrity Die Casting Processes.* John Wiley & Sons, 2002.

[45]- L. Pezzato, M. Dabalà, S. Gross, and K. Brunelli. "Effect of Microstructure and Porosity of AlSi10Mg Alloy Produced by Selective Laser Melting on the Corrosion Properties of Plasma Electrolytic Oxidation Coatings." *Surface and Coatings Technology* 404 (2020): 126477. https://doi.org/10.1016/j.surfcoat.2020.126477.

[46]- A. B. Rogov, H. Lyu, A. Matthews, and A. Yerokhin. "AC Plasma Electrolytic Oxidation of Additively Manufactured and Cast AlSi12 Alloys." *Surface and Coatings Technology* 399 (2020): 126116. https://doi.org/10.1016/j.surfcoat.2020.126116.

[47]- B. Zhu and C. Zanella. "Hardness and Corrosion Behaviour of Anodised Al–Si Produced by Rheocasting." *Materials & Design* 173 (2019): 107764. https://doi.org/10.1016/j.matdes.2019.107764.

[48]- H.-H. Lien, J. Mazumder, J. Wang, and A. Misra. "Microstructure Evolution and High Density of Nanotwinned Ultrafine Si in Hypereutectic Al–Si Alloy by Laser Surface Remelting." *Materials Characterization* 161 (2020): 110147. https://doi.org/10.1016/j.matchar.2020.110147.

[49]- H. Mora-Sanchez, et al. "Hard Anodizing and Plasma Electrolytic Oxidation of an Additively Manufactured Al–Si Alloy." *Surface and Coatings Technology* 420 (2021): 127339. https://doi.org/10.1016/j.surfcoat.2021.127339.

[50]- P. Wang, Q. Ma, Q. Yuwen, and J. Li. "The Differences in the Formation Mechanism of PEO and CPED Composited Ceramic Coatings on Al–12Si Alloy." *Journal of Alloys and Compounds* 788 (2019): 61–66. https://doi.org/10.1016/j.jallcom.2019.01.333.

[51]- J. W. Diggle, T. C. Downie, and C. W. Goulding. "Anodic Oxide Films on Aluminum." *Chemical Reviews* 69, no. 3 (1969): 365–405. https://doi.org/10.1021/cr60259a005.

[52]- G. E. Thompson. "Porous Anodic Alumina: Fabrication, Characterization and Applications." *Thin Solid Films* 297, no. 1–2 (1997): 192–201. https://doi.org/10.1016/S0040-6090(96)09440-0.

[53]- J. P. O'Sullivan, G. C. Wood. "The Morphology and Mechanism of Formation of Porous Anodic Films on Aluminium." *Proceedings of the Royal Society of London. Series A* 317, no. 1531 (1970): 511–543. https://doi.org/10.1098/rspa.1970.0129.

[54]- J. Asensio-Lozano, B. Suárez-Peña, and G. Vander Voort. "Effect of Processing Steps on the Mechanical Properties and Surface Appearance of 6063 Aluminium Extruded Products." *Materials* 7, no. 6 (2014): 4224–4242. https://doi.org/10.3390/ma7064224.

[55]- J. Runge and L. Chesterfield. "Connecting Theory to Practice: The Science of Successfully Anodizing Aluminum Die Castings." (2010). *Aluminium International Today* 22, no. 6 (2010): 25.

[56]- J. Chen, et al. "The Microstructure and Property of Al–Si Alloy Improved by the Sc-Microalloying and Y2O3 Nano-Particles." *Science and Technology of Advanced Materials* 22, no. 1 (2021): 205–217. https://doi.org/10.1080/14686996.2021.1891841.

[57]- J.-M. Huang, H.-D. Zhao, and Z.-M. Chen. "Microstructure and Properties of A356 Alloy Wheels Fabricated by Low-Pressure Die Casting with Local Squeeze." *Journal of Materials Engineering and Performance* 28, no. 4 (2019): 2137–2146. https://doi.org/10.1007/s11665-019-03993-5.

[58]- J. Konieczny, L. A. Dobrzański, K. Labisz, and J. Duszczyk. "The Influence of Cast Method and Anodizing Parameters on Structure and Layer Thickness of Aluminium Alloys." *Journal of Materials Processing Technology* 157–158 (2004): 718–723. https://doi.org/10.1016/j.jmatprotec.2004.07.130.

[59]- Tsangaraki-Kaplanoglou, S. Theohari, Th. Dimogerontakis, Y.-M. Wang, H.-H. Kuo, and S. Kia. "Effect of Alloy Types on the Anodizing Process of Aluminum." *Surface and Coatings Technology* 200, no. 8 (2006): 2634–2641. https://doi.org/10.1016/j.surfcoat.2005.07.065.

[60]- R. Arrabal, B. Mingo, A. Pardo, M. Mohedano, E. Matykina, and I. Rodríguez. "Pitting Corrosion of Rheocast A356 Aluminium Alloy in 3.5 wt.% NaCl Solution." *Corrosion Science* 73 (2013): 342–355. https://doi.org/10.1016/j.corsci.2013.04.023.

[61]- B. Mingo, R. Arrabal, A. Pardo, E. Matykina, and P. Skeldon. "3D Study of Intermetallics and Their Effect on the Corrosion Morphology of Rheocast Aluminium Alloy." *Materials Characterization* 112 (2016): 122–128. https://doi.org/10.1016/j.matchar.2015.12.006.

[62]- L. E. Fratila-Apachitei, J. Duszczyk, and L. Katgerman. "Vickers Microhardness of AlSi(Cu) Anodic Oxide Layers Formed in H_2SO_4 at Low Temperature." *Surface and Coatings Technology* 165, no. 3 (2003): 309–315. https://doi.org/10.1016/S0257-8972(02)00750-8.

[63]- F. Zhang, C. Örnek, J.-O. Nilsson, and J. Pan. "Anodisation of Aluminium Alloy AA7075 – Influence of Intermetallic Particles on Anodic Oxide Growth." *Corrosion Science* 164 (2020): 108319. https://doi.org/10.1016/j.corsci.2019.108319.

[64]- L. E. Fratila-Apachitei, F. D. Tichelaar, G. E. Thompson, H. Terryn, P. Skeldon, J. Duszczyk, and L. Katgerman. "A Transmission Electron Microscopy Study of Hard Anodic Oxide Layers on AlSi(Cu) Alloys." *Electrochimica Acta* 49, no. 19 (2004): 3169–3177. https://doi.org/10.1016/j.electacta.2004.02.030.

[65]- B. Zhu, S. Seifeddine, P. O. Å. Persson, A. E. W. Jarfors, P. Leisner, and C. Zanella. "A Study of Formation and Growth of the Anodised Surface Layer on Cast Al–Si Alloys Based on Different Analytical Techniques." *Materials & Design* 101 (2016): 254–262. https://doi.org/10.1016/j.matdes.2016.04.013.

[66]- E. Razzouk, D. Koncz-Horváth, and T. I. Török. "Microstructure Effects on Anodizing High-Silicon Aluminium Alloy AlSi12Cu1(Fe) under Various Surface Conditions and Power Modes." *Crystals* 14, no. 4 (2024): 352. https://doi.org/10.3390/cryst14040352.

[67]- L. E. Fratila-Apachitei, J. Duszczyk, and L. Katgerman. "Voltage Transients and Morphology of AlSi(Cu) Anodic Oxide Layers Formed in H_2SO_4 at Low Temperature." *Surface and Coatings Technology* 157, no. 1 (2002): 80–94. https://doi.org/10.1016/S0257-8972(02)00144-5.

[68]- C. W.Meyers, K. H. Hinton, and J-S. Chou. "Towards the Optimization of Heat Treatment in Aluminum Alloys." *Materials Science Forum* 72 (1992): 102–104. https://doi.org/10.4028/www.scientific.net/MSF.102-104.75.

[69]- A. K. Dahle, K. Nogita, S. D. McDonald, C. Dinnis, and L. Lu. "Eutectic Modification and Microstructure Development in Al–Si Alloys." *Materials Science and Engineering: A* 413–414 (2005): 243–248. https://doi.org/10.1016/j.msea.2005.09.055.

[70]- S.-L. Xu, H.-L. Jia, M. Zha, X.-L. Zhou, D. Gao, P.-K. Ma, and D. Wang. "The Effect of B and Sb on the Corrosion Behavior of T6-Treated Al–Si–Mg Alloys." *Journal of Materials Research and Technology* (2024). 3611-3621. https://doi.org/10.1016/j.jmrt.2024.04.083.

[71]- F. Riddar, S. Hogmark, and Å. K. Rudolphi. "Comparison of Anodised Aluminium Surfaces from Four Fabrication Methods." *Journal of Materials Processing Technology* 212, no. 11 (2012): 2272–2281. https://doi.org/10.1016/j.jmatprotec.2012.06.007.

[72]- L. Chauke, K. Mutombo, and G. Govender. "Corrosion Behaviour of the Anodised A356 Aluminium Alloy Produced by the Rheo-High Pressure Die Casting Process." *Advanced Materials Research* 1019 (2014): 67–73. https://doi.org/10.4028/www.scientific.net/AMR.1019.67.

[73]- S. Menargues, J. A. Picas, E. Martin, M. T. Baile, M. Campillo, and A. Forn. "Surface Finish Effect on the Anodizing Behaviour of Al–Si Components Obtained by Sub-Liquidus Casting Process." *International Journal of Material Forming* 3, no. S1 (2010): 767–770. https://doi.org/10.1007/s12289-010-0883-0.

[74]- L. Ceschini, I. Boromei, A. Morri, S. Seifeddine, and I. L. Svensson. "Effect of Fe Content and Microstructural Features on the Tensile and Fatigue Properties of the Al–Si10–Cu2 Alloy." *Materials & Design* 36 (2012): 522–528. https://doi.org/10.1016/j.matdes.2011.11.047.

[75]- M. Jariyaboon, P. Møller, R. E. Dunin-Borkowski, and R. Ambat. "FIB-SEM Investigation of Trapped Intermetallic Particles in Anodic Oxide Films on AA1050 Aluminium." *Anti-Corrosion Methods and Materials* 58, no. 4 (2011): 173–178. https://doi.org/10.1108/00035591111148885.

[76]- L. E. Fratila-Apachitei, H. Terryn, P. Skeldon, G. E. Thompson, J. Duszczyk, and L. Katgerman. "Influence of Substrate Microstructure on the Growth of Anodic Oxide Layers." *Electrochimica Acta* 49, no. 7 (2004): 1127–1140. https://doi.org/10.1016/j.electacta.2003.10.024.

[77]- A. K. Mukhopadhyay and A. K. Sharma. “Influence of Fe-Bearing Particles and Nature of Electrolyte on the Hard Anodizing Behaviour of AA7075 Extrusion Products.” *Surface and Coatings Technology* 92, no. 3 (1997): 212–220. https://doi.org/10.1016/S0257-8972(97)00102-3.

[78]- K. Shimizu, G. M. Brown, K. Kobayashi, P. Skeldon, G. E. Thompson, and G. C. Wood. “Ultramicrotomy—A Route towards the Enhanced Understanding of the Corrosion and Filming Behaviour of Aluminium and Its Alloys.” *Corrosion Science* 40, no. 7 (1998): 1049–1072. https://doi.org/10.1016/S0010-938X(98)00006-7.

[79]- F. Zhang, J.-O. Nilsson, and J. Pan. “In Situ and Operando AFM and EIS Studies of Anodization of Al 6060: Influence of Intermetallic Particles.” *Journal of The Electrochemical Society* 163, no. 9 (2016): C609–C618. https://doi.org/10.1149/2.0061610jes.

[80]- H. Wu, et al. “Effect of Iron-Containing Intermetallic Particles on Film Structure and Corrosion Resistance of Anodized AA2099 Alloy.” *Journal of The Electrochemical Society* 165, no. 9 (2018): C573–C581. https://doi.org/10.1149/2.1361809jes.

[81]- A. M. A. Mohamed and F. H. Samuel. “A Review on the Heat Treatment of Al–Si–Cu/Mg Casting Alloys.” In: F. Czerwinski (Ed.), *Heat Treatment - Conventional and Novel Applications.* InTech, 2012. https://doi.org/10.5772/50282.

[82]- Z. Li, A. M. Samuel, F. H. Samuel, C. Ravindran, and S. Valtierra. “Effect of Alloying Elements on the Segregation and Dissolution of $CuAl_2$ Phase in Al–Si–Cu 319 Alloys.” *Journal of materials science* 38, no. 6 (2003): 1203-1218. https://doi.org/10.1023/A:1022857703995.

[83]- G. Scampone and G. Timelli. “Anodizing Al–Si Foundry Alloys: A Critical Review.” *Advanced Engineering Materials* 24, no. 4 (2022): 2101480. https://doi.org/10.1002/adem.202101480.

[84]- A. M. Samuel and F. H. Samuel. “Modification of Iron Intermetallics by Magnesium and Strontium in Al–Si Alloys.” *International Journal of Cast Metals Research* 10, no. 3 (1997): 147–157. https://doi.org/10.1080/13640461.1997.11819229.

[85]- B. Gastón-García, E. García-Lecina, M. Díaz-Fuentes, J. A. Díez, and C. Müller. “Sulphuric Acid Anodising of EN AC-46500 Cast Aluminium Alloy.” *Transactions of the IMF* 89, no. 6 (2011): 312–319. https://doi.org/10.1179/174591911X13167804921037.

[86]- Q. Meng and G. S. Frankel. “Effect of Cu Content on Corrosion Behavior of 7xxx Series Aluminum Alloys.” *Journal of The Electrochemical Society* 151, no. 5 (2004): B271. https://doi.org/10.1149/1.1695385.

[87]- M. Saenz De Miera, M. Curioni, P. Skeldon, and G. E. Thompson. “Preferential Anodic Oxidation of Second-Phase Constituents during Anodising of AA2024-T3 and AA7075-T6 Alloys.” *Surface and Interface Analysis* 42, no. 4 (2010): 241–246. https://doi.org/10.1002/sia.3191.

[88]- N. Birbilis, M. K. Cavanaugh, and R. G. Buchheit. “Electrochemical Behavior and Localized Corrosion Associated with Al7Cu2Fe Particles in Aluminum Alloy 7075-T651.” *Corrosion Science* 48, no. 12 (2006): 4202–4215. https://doi.org/10.1016/j.corsci.2006.02.007.

[89]- K. Labisz, L. A. Dobrzański, and J. Konieczny. "Anodization of Cast Aluminium Alloys Produced by Different Casting Methods." *Archives of Foundry Engineering* 8 (2008): 45–50.

[90]- D. Caliari, G. Timelli, B. Zabala, and A. Igartua. "Microstructural and Tribological Investigations of Diecast and Hard Anodized AlSiCu Alloys." *Surface and Coatings Technology* 352 (2018): 462–473. https://doi.org/10.1016/j.surfcoat.2018.07.084.

[91]- L. Chauke, H. Möller, U. A. Curle, and G. Govender. "Anodising of Al–Mg–Si–(Cu) Alloys Produced by R-HPDC." *Materials Science Forum* 765 (2013): 658–662. https://doi.org/10.4028/www.scientific.net/MSF.765.658.

[92]- J. S. Shin, B. H. Kim, and S. M. Lee. "A Study on Surface Oxidation Coating Characteristic of Al–Si Casting Alloys." *Materials Science Forum* 724 (2012): 173–177. https://doi.org/10.4028/www.scientific.net/MSF.724.173.

[93]- D.-I. N. V. Mandich and B. Road. "Surface Preparation of Metals Prior to Plating." (2002): 16–22.

[94]- L. Chauke, H. Möller, and G. Govender. "Anodising of Aluminium Alloy Plates from Different Series Produced by Rheo-High Pressure Die Casting." *Solid State Phenomena* 217–218 (2014): 247–252. https://doi.org/10.4028/www.scientific.net/SSP.217-218.247.

[95]- Y. Gao, A. Yerokhin, and A. Matthews. "DC Plasma Electrolytic Oxidation of Biodegradable cp-Mg: In-Vitro Corrosion Studies." *Surface and Coatings Technology* 234 (2013): 132–142. https://doi.org/10.1016/j.surfcoat.2012.11.035.

[96]- R. H. U. Khan, A. Yerokhin, X. Li, H. Dong, and A. Matthews. "Surface Characterisation of DC Plasma Electrolytic Oxidation Treated 6082 Aluminium Alloy: Effect of Current Density and Electrolyte Concentration." *Surface and Coatings Technology* 205, no. 6 (2010): 1679–1688. https://doi.org/10.1016/j.surfcoat.2010.04.052.

[97]- Y. Gu, C. Chen, S. Bandopadhyay, C. Ning, Y. Zhang, and Y. Guo. "Corrosion Mechanism and Model of Pulsed DC Microarc Oxidation Treated AZ31 Alloy in Simulated Body Fluid." *Applied Surface Science* 258, no. 16 (2012): 6116–6126. https://doi.org/10.1016/j.apsusc.2012.03.016.

[98]- Y. Guan, Y. Xia, and G. Li. "Growth Mechanism and Corrosion Behavior of Ceramic Coatings on Aluminum Produced by Autocontrol AC Pulse PEO." *Surface and Coatings Technology* 202, no. 19 (2008): 4602–4612. https://doi.org/10.1016/j.surfcoat.2008.03.031.

[99]- S. Wang, Y. Xia, L. Liu, and N. Si. "Preparation and Performance of MAO Coatings Obtained on AZ91D Mg Alloy under Unipolar and Bipolar Modes in a Novel Dual Electrolyte." *Ceramics International* 40, no. 1 (2014): 93–99. https://doi.org/10.1016/j.ceramint.2013.05.108.

[100]- X. Guo, K. Du, Y. Wang, Y. Shao, and F. Wang. "A New Nanoparticle Penetrant Used for Plasma Electrolytic Oxidation Film Coated on AZ31 Mg Alloy in Service Environment." *Surface and Coatings Technology* 206, no. 23 (2012): 4833–4839. https://doi.org/10.1016/j.surfcoat.2012.05.063.

[101]- A. Lugovskoy and M. Zinigrad. "Plasma Electrolytic Oxidation of Valve Metals." *Materials Science – Advanced Topics* 1 (2013): 85–102.

[102]- S. Wang, X. Liu, X. Yin, and N. Du. "Influence of Electrolyte Components on the Microstructure and Growth Mechanism of Plasma Electrolytic Oxidation Coatings on 1060 Aluminum Alloy." *Surface and Coatings Technology* 381 (2020): 125214. https://doi.org/10.1016/j.surfcoat.2019.125214.

[103]- X. Nie, E. I. Meletis, J. C. Jiang, A. Leyland, A. L. Yerokhin, and A. Matthews. "Abrasive Wear/Corrosion Properties and TEM Analysis of Al_2O_3 Coatings Fabricated Using Plasma Electrolysis." *Surface and Coatings Technology* 149, no. 2-3 (2002): 245-251. https://doi.org/10.1016/S0257-8972(01)01453-0.

[104]- K. R. Shin, Y. G. Ko, and D. H. Shin. "Effect of Electrolyte on Surface Properties of Pure Titanium Coated by Plasma Electrolytic Oxidation." *Journal of Alloys and Compounds* 509 (2011): S478–S481. https://doi.org/10.1016/j.jallcom.2011.02.056.

[105]- A. Nominé, S. C. Troughton, A. V. Nominé, G. Henrion, and T. W. Clyne. "High Speed Video Evidence for Localised Discharge Cascades during Plasma Electrolytic Oxidation." *Surface and Coatings Technology* 269 (2015): 125–130. https://doi.org/10.1016/j.surfcoat.2015.01.043.

[106]- M. Kaseem, S. Fatimah, N. Nashrah, and Y. G. Ko. "Recent Progress in Surface Modification of Metals Coated by Plasma Electrolytic Oxidation: Principle, Structure, and Performance." *Progress in Materials Science* 117 (2021): 100735. https://doi.org/10.1016/j.pmatsci.2020.100735.

[107]- V. Dehnavi. *Surface Modification of Aluminum Alloys by Plasma Electrolytic Oxidation.* The University of Western Ontario (Canada), 2014.

[108]- L. Wang and X. Nie. "Silicon Effects on Formation of EPO Oxide Coatings on Aluminum Alloys." *Thin Solid Films* 494, no. 1–2 (2006): 211–218. https://doi.org/10.1016/j.tsf.2005.07.184.

[109]- M. M. S. Al Bosta, K.-J. Ma, and H.-H. Chien. "The Effect of MAO Processing Time on Surface Properties and Low Temperature Infrared Emissivity of Ceramic Coating on Aluminium 6061 Alloy." *Infrared Physics & Technology* 60 (2013): 323–334. https://doi.org/10.1016/j.infrared.2013.06.006.

[110]- G. Sundararajan and L. Rama Krishna. "Mechanisms Underlying the Formation of Thick Alumina Coatings through the MAO Coating Technology." *Surface and Coatings Technology* 167, no. 2–3 (2003): 269–277. https://doi.org/10.1016/S0257-8972(02)00918-0.

[111]- S. Moon and Y. Jeong. "Generation Mechanism of Microdischarges during Plasma Electrolytic Oxidation of Al in Aqueous Solutions." *Corrosion Science* 51, no. 7 (2009): 1506–1512. https://doi.org/10.1016/j.corsci.2008.10.039.

[112]- E. V. Parfenov, A. Yerokhin, R. R. Nevyantseva, M. V. Gorbatkov, C.-J. Liang, and A. Matthews. "Towards Smart Electrolytic Plasma Technologies: An Overview of Methodological Approaches to Process Modelling." *Surface and Coatings Technology* 269 (2015): 2–22. https://doi.org/10.1016/j.surfcoat.2015.02.019.

[113]- G. Li, Y. Wang, L. Qiao, R. Zhao, S. Zhang, R. Zhang, C. Chen, X. Li, and Y. Zhao. "Preparation and Formation Mechanism of Copper Incorporated Micro-Arc Oxidation Coatings

Developed on Ti–6Al–4V Alloys." *Surface and Coatings Technology* 375 (2019): 74–85. https://doi.org/10.1016/j.surfcoat.2019.06.096.

[114]- Y. Zhang, Y. Wu, D. Chen, R. Wang, D. Li, C. Guo, G. Jiang, D. Shen, S. Yu, and P. Nash. "Micro-Structures and Growth Mechanisms of Plasma Electrolytic Oxidation Coatings on Aluminium at Different Current Densities." *Surface and Coatings Technology* 321 (2017): 236–246. https://doi.org/10.1016/j.surfcoat.2017.04.064.

[115]- R. O. Hussein, D. O. Northwood, and X. Nie. "Coating Growth Behavior during the Plasma Electrolytic Oxidation Process." *Journal of Vacuum Science & Technology A: Vacuum, Surfaces, and Films* 28, no. 4 (2010): 766–773. https://doi.org/10.1116/1.3429583.

[116]- R. H. U. Khan, A. L. Yerokhin, T. Pilkington, A. Leyland, and A. Matthews. "Residual Stresses in Plasma Electrolytic Oxidation Coatings on Al Alloy Produced by Pulsed Unipolar Current." *Surface and Coatings Technology* 200, no. 5–6 (2005): 1580–1586. https://doi.org/10.1016/j.surfcoat.2005.08.092.

[117]- R. O. Hussein, P. Zhang, X. Nie, Y. Xia, and D. O. Northwood. "The Effect of Current Mode and Discharge Type on the Corrosion Resistance of Plasma Electrolytic Oxidation (PEO) Coated Magnesium Alloy AJ62." *Surface and Coatings Technology* 206, no. 7 (2011): 1990–1997. https://doi.org/10.1016/j.surfcoat.2011.08.060.

[118]- A. L. Yerokhin, A. Shatrov, V. Samsonov, P. Shashkov, A. Pilkington, A. Leyland, and A. Matthews. "Oxide Ceramic Coatings on Aluminium Alloys Produced by a Pulsed Bipolar Plasma Electrolytic Oxidation Process." *Surface and Coatings Technology* 199, no. 2–3 (2005): 150–157. https://doi.org/10.1016/j.surfcoat.2004.10.147.

[119]- F. Xu, Y. Xia, and G. Li. "The Mechanism of PEO Process on Al–Si Alloys with the Bulk Primary Silicon." *Applied Surface Science* 255, no. 23 (2009): 9531–9538. https://doi.org/10.1016/j.apsusc.2009.07.090.

[120]- K. Li, W. Li, G. Zhang, W. Zhu, F. Zheng, D. Zhang, and M. Wang. "Effects of Si Phase Refinement on the Plasma Electrolytic Oxidation of Eutectic Al–Si Alloy." *Journal of Alloys and Compounds* 790 (2019): 650–656. https://doi.org/10.1016/j.jallcom.2019.03.217.

[121]- S. Stojadinović, R. Vasić, M. Petković, Z. Nedić, B. Kasalica, I. Belča, Lj. Zeković. "Luminescence Properties of Oxide Films Formed by Anodization of Aluminum in 12-Tungstophosphoric Acid." *Electrochimica Acta* 55, no. 12 (2010): 3857–3863. https://doi.org/10.1016/j.electacta.2010.02.011.

[122]- S. Fatimah, M. P. Kamil, J. H. Kwon, M. Kaseem, and Y. G. Ko. "Dual Incorporation of SiO_2 and ZrO_2 Nanoparticles into the Oxide Layer on 6061 Al Alloy via Plasma Electrolytic Oxidation: Coating Structure and Corrosion Properties." *Journal of Alloys and Compounds* 707 (2017): 358–364. https://doi.org/10.1016/j.jallcom.2016.11.098.

[123]- M. Mohedano, C. Blawert, and M. L. Zheludkevich. "Silicate-Based Plasma Electrolytic Oxidation (PEO) Coatings with Incorporated CeO_2 Particles on AM50 Magnesium Alloy." *Materials & Design* 86 (2015): 735–744. https://doi.org/10.1016/j.matdes.2015.07.132.

[124]- M. Aliofkhazraei, A. Sabour Rouhaghdam, and T. Shahrabi. “Abrasive Wear Behaviour of Si_3N_4/TiO_2 Nanocomposite Coatings Fabricated by Plasma Electrolytic Oxidation.” *Surface and Coatings Technology* 205 (2010): S41–S46. https://doi.org/10.1016/j.surfcoat.2010.03.052.

[125]- G. Yeshmanova, C. Blawert, M. Serdechnova, M. Starykevich, T. Wu, U. Kakimov, V. Kasneryk, T. Shulha, D. Smagulov, and M. L. Zheludkevich. “Influence of Different Si Sources on Plasma Electrolytic Oxidation Coating Formation, Morphology and Composition.” *Journal of Alloys and Compounds* 1036 (2025): 181845. https://doi.org/10.1016/j.jallcom.2025.181845.

[126]- U. Malayoglu, K. C. Tekin, U. Malayoglu, and S. Shrestha. “An Investigation into the Mechanical and Tribological Properties of Plasma Electrolytic Oxidation and Hard-Anodized Coatings on 6082 Aluminum Alloy.” *Materials Science and Engineering: A* 528, no. 24 (2011): 7451–7460. https://doi.org/10.1016/j.msea.2011.06.032.

[127]- E. Matykina, R. Arrabal, P. Skeldon, and G. E. Thompson. “Incorporation of Zirconia Nanoparticles into Coatings Formed on Aluminium by AC Plasma Electrolytic Oxidation.” *Journal of Applied Electrochemistry 38, no. 10 (2008): 1375-1383.* https://doi.org/10.1007/s10800-008-9575-6.

[128]- E. López-Martínez, M. Mohedano, E. Matykina, and R. Arrabal. "PEO of additively manufactured Al10SiMg alloy: Effects of α-Al_2O_3 particles on energy consumption and wear behavior." *Journal of Materials Research and Technology* 31 (2024): 1786-1796. https://doi.org/10.1016/j.jmrt.2024.06.171.

[129]- M. Nadimi, C. Dehghanian, and A. Etemadmoghadam. “Influence of SiO_2 Nanoparticles Incorporating into Ceramic Coatings Generated by PEO on Aluminium Alloy: Morphology, Adhesion, Corrosion, and Wear Resistance.” *Materials Today Communications* 31 (2022): 103587. https://doi.org/10.1016/j.mtcomm.2022.103587.

[130]- C.-J. Hu and M.-H. Hsieh. “Preparation of Ceramic Coatings on an Al–Si Alloy by the Incorporation of ZrO_2 Particles in Microarc Oxidation.” *Surface and Coatings Technology* 258 (2014): 275–283. https://doi.org/10.1016/j.surfcoat.2014.09.012.

[131]- M. Shokouhfar and S. R. Allahkaram. “Formation Mechanism and Surface Characterization of Ceramic Composite Coatings on Pure Titanium Prepared by Micro-Arc Oxidation in Electrolytes Containing Nanoparticles.” *Surface and Coatings Technology* 291 (2016): 396–405. https://doi.org/10.1016/j.surfcoat.2016.03.013.

[132]- C.-Y. Liu, D.-S. Tsai, J.-M. Wang, J. T. J. Tsai, and C.-C. Chou. “Particle Size Influences on the Coating Microstructure through Green Chromia Inclusion in Plasma Electrolytic Oxidation.” *ACS Applied Materials & Interfaces* 9, no. 26 (2017): 21864–21871. https://doi.org/10.1021/acsami.7b03113.

[133]- M. O’Hara, S. C. Troughton, R. Francis, and T. W. Clyne. “The Incorporation of Particles Suspended in the Electrolyte into Plasma Electrolytic Oxidation Coatings on Ti and Al Substrates.” *Surface and Coatings Technology* 385 (2020): 125354. https://doi.org/10.1016/j.surfcoat.2020.125354.

[134]- X. Lu, C. Blawert, M. L. Zheludkevich, and K. U. Kainer. "Insights into Plasma Electrolytic Oxidation Treatment with Particle Addition." *Corrosion Science* 101 (2015): 201–207. https://doi.org/10.1016/j.corsci.2015.09.016.

[135]- M. Mohedano, E. Lopez, B. Mingo, S. Moon, E. Matykina, and R. Arrabal. "Energy Consumption, Wear and Corrosion of PEO Coatings on Preanodized Al Alloy: The Influence of Current and Frequency." *Journal of Materials Research and Technology* 21 (2022): 2061–2075. https://doi.org/10.1016/j.jmrt.2022.10.049.

[136]- K. Auzins, A. Zolotarjovs, I. Bite, K. Laganovska, V. Vitola, K. Smits, and D. Millers. "Production of Phosphorescent Coatings on 6082 Aluminum Using $Sr_{0.95}Eu_{0.02}Dy_{0.03}Al_2O_4$-δ Powder and Plasma Electrolytic Oxidation." *Coatings* 9, no. 12 (2019): 865. https://doi.org/10.3390/coatings9120865.

[137]- I. Bite, G. Krieke, A. Zolotarjovs, K. Laganovska, V. Liepina, K. Smits, K. Auzins, L. Grigorjeva, D. Millers, and L. Skuja. "Novel Method of Phosphorescent Strontium Aluminate Coating Preparation on Aluminum." *Materials & Design* 160 (2018): 794–802. https://doi.org/10.1016/j.matdes.2018.10.021.

[138]- G. Scampone and G. Timelli. "Effect of Surface Roughness and Eutectic Segregation on Anodising of Al–Si–Cu Alloys." *Materials Science and Technology* 40, no. 17 (2024): 1245–1254. https://doi.org/10.1177/02670836241245205.

[139]- D. Caliari, G. Timelli, T. Salata, G. Cavagnini, S. Maestri, and A. Manfredini. "Influence of Microstructure and Surface Finishing on the Hard Anodizing of Diecast Al–Si–Cu Alloys." *Light Metals* (2019).

[140]- "Surface Defects of Anodized HPDC Al Alloy Components." (n.d.). https://www.research.unipd.it/handle/11577/3232463 (accessed April 24, 2024).

[141]- K. Davis. "Material Review: Alumina (Al_2O_3)." *School of Doctoral Studies European Union Journal* 2 (2010).

[142]- Oxide - Al_2O_3 - A Refractory Ceramic Oxide, Accessed date: 20 April 2025. https://www.azom.com/properties.aspx?ArticleID=52. (2018).

[143]- M. Bononi, M. Conte, R. Giovanardi, and A. Bozza. "Hard Anodizing of AA2099-T8 Aluminum-Lithium-Copper Alloy: Influence of Electric Cycle, Electrolytic Bath Composition and Temperature." *Surface and Coatings Technology* 325 (2017): 627–635. https://doi.org/10.1016/j.surfcoat.2017.07.028.

[144]- A. Bozza, R. Giovanardi, T. Manfredini, and P. Mattioli. "Pulsed Current Effect on Hard Anodizing Process of 7075-T6 Aluminium Alloy." *Surface and Coatings Technology* 270 (2015): 139–144. https://doi.org/10.1016/j.surfcoat.2015.03.010.

[145]- M.M. Makhlouf and D. Apelian. *Casting Characteristics of Aluminum Die Casting Alloys*. Final Report, No. DOE/ID-13716. Worcester Polytechnic Institute, 2002. https://doi.org/10.2172/792701.

[146]- V. Dehnavi, B. L. Luan, X. Y. Liu, D. W. Shoesmith, and S. Rohani. "Correlation between Plasma Electrolytic Oxidation Treatment Stages and Coating Microstructure on Aluminum under

Unipolar Pulsed DC Mode." *Surface and Coatings Technology* 269 (2015): 91–99. https://doi.org/10.1016/j.surfcoat.2014.11.007.

[147]- D.-S. Tsai and C.-C. Chou. "Influences of Growth Species and Inclusions on the Current–Voltage Behavior of Plasma Electrolytic Oxidation: A Review." *Coatings* 11, no. 3 (2021): 270. https://doi.org/10.3390/coatings11030270.

[148]- E. Matykina, R. Arrabal, M. Mohedano, B. Mingo, J. Gonzalez, A. Pardo, and M. C. Merino. "Recent Advances in Energy Efficient PEO Processing of Aluminium Alloys." *Transactions of Nonferrous Metals Society of China* 27, no. 7 (2017): 1439–1454. https://doi.org/10.1016/S1003-6326(17)60166-3.

[149]- S. P. Sah, E. Tsuji, Y. Aoki, and H. Habazaki. "Cathodic Pulse Breakdown of Anodic Films on Aluminium in Alkaline Silicate Electrolyte—Understanding the Role of the Cathodic Half-Cycle in AC Plasma Electrolytic Oxidation." *Corrosion Science* 55 (2012): 90–96. https://doi.org/10.1016/j.corsci.2011.10.007.

[150]- A. Nominé, J. Martin, G. Henrion, and T. Belmonte. "Effect of Cathodic Micro-Discharges on Oxide Growth during Plasma Electrolytic Oxidation (PEO)." *Surface and Coatings Technology* 269 (2015): 131–137. https://doi.org/10.1016/j.surfcoat.2015.01.076.

[151]- Li, G. Zhang, A. Yi, W. Zhu, Z. Liao, K. Chen, W. Li, and Z. Luo. "Effects of Matrix Silicon Content on the Plasma Electrolytic Oxidation of Al–Si Alloys Using Different Power Modes." *Crystals* 12, no. 1 (2022): 123. https://doi.org/10.3390/cryst12010123.

[152]- T. W. Clyne and S. C. Troughton. "A Review of Recent Work on Discharge Characteristics during Plasma Electrolytic Oxidation of Various Metals." *International Materials Reviews* 64, no. 3 (2019): 127–162. https://doi.org/10.1080/09506608.2018.1466492.

[153]- E. Bousser, A. Rogov, P. Shashkov, A. Gholinia, N. Laugel, T. J. A. Slater, P. J. Withers, A. Matthews, and A. Yerokhin. "Phase Transitions in Alumina Films during Post-Sparking Anodising of Al Alloys." *Acta Materialia* 244 (2023): 118587. https://doi.org/10.1016/j.actamat.2022.118587.

[154]- Materials Data on Al10Si2O19 by Materials Project. United States: N. p., (2020). Web. https://doi.org/10.17188/1202597.

[155]- U. Mark. "Characterization of Ibere and Oboro clay deposits in Abia state, Nigeria for refractory applications." *International Journal of Natural and Applied Sciences* 6, no. 3 (2010): 296-305.

[156]- K. Tang, L. K. Jakobsson, and K. Hildal. "Thermodynamic Evaluation of Sr-Containing Si Metals and Silicate Melts for Si-Sr Alloy Production." *Journal of the Southern African Institute of Mining and Metallurgy* 118, no. 6 (2018). https://doi.org/10.17159/2411-9717/2018/v118n6a7.

[157]- *HSC Chemistry 5.1.* Outokumpu. (2002).

[158]- E. Matykina, R. Arrabal, P. Skeldon, and G. E. Thompson. "Investigation of the Growth Processes of Coatings Formed by AC Plasma Electrolytic Oxidation of Aluminium." *Electrochimica Acta* 54, no. 27 (2009): 6767–6778. https://doi.org/10.1016/j.electacta.2009.06.088.

[159]- J. Martin, A. Nominé, F. Brochard, J.-L. Briançon, C. Noël, T. Belmonte, T. Czerwiec, and G. Henrion. "Delay in Micro-Discharges Appearance during PEO of Al: Evidence of a Mechanism of Charge Accumulation at the Electrolyte/Oxide Interface." *Applied Surface Science* 410 (2017): 29–41. https://doi.org/10.1016/j.apsusc.2017.03.088.

[160]- J. Jovović, S. Stojadinović, N. M. Šišović, and N. Konjević. "Spectroscopic Study of Plasma during Electrolytic Oxidation of Magnesium- and Aluminium-Alloy." *Journal of Quantitative Spectroscopy and Radiative Transfer* 113, no. 15 (2012): 1928–1937. https://doi.org/10.1016/j.jqsrt.2012.06.008.

[161]- A. I. Slonova, O. P. Terleeva, V. I. Belevantsev, and A. B. Rogov. "Formation of Microplasma Coatings on High-Silicon Aluminum Alloy and Their Characteristics." *Protection of Metals and Physical Chemistry of Surfaces* 48, no. 1 (2012): 86–96. https://doi.org/10.1134/S207020511201011X.

[162]- M. Mohedano, E. Matykina, R. Arrabal, B. Mingo, and A. Pardo. "PEO of Pre-Anodized Al–Si Alloys: Corrosion Properties and Influence of Sealings." *Applied Surface Science* 346 (2015): 57–67. https://doi.org/10.1016/j.apsusc.2015.03.206.

[163]- J. M. Wheeler, J. A. Curran, and S. Shrestha. "Microstructure and Multi-Scale Mechanical Behavior of Hard Anodized and Plasma Electrolytic Oxidation (PEO) Coatings on Aluminum Alloy 5052." *Surface and Coatings Technology* 207 (2012): 480–488. https://doi.org/10.1016/j.surfcoat.2012.07.056.

[164]- P.B. Srinivasan, C. Blawert, and W. Dietzel. "Dry Sliding Wear Behaviour of Plasma Electrolytic Oxidation Coated AZ91 Cast Magnesium Alloy." *Wear* 266, no. 11–12 (2009): 1241–1247. https://doi.org/10.1016/j.wear.2009.03.013.

[165]- M. Alanazi, A. Leyland, A. L. Yerokhin, and A. Matthews. "Substitution of Hexavalent Chromate Conversion Treatment with a Plasma Electrolytic Oxidation Process to Improve the Corrosion Properties of Ion Vapour Deposited AlMg Coatings." *Surface and Coatings Technology* 205, no. 6 (2010): 1750–1756. https://doi.org/10.1016/j.surfcoat.2010.09.017.

[166]- H. Fan, K. Liang, R. Bai, C. Wang, J. Zhang, and L. Wang. "Enhanced Corrosion Resistance of PEO Coating on AZ31B Mg Alloys with Delayed Corrosion and Slow Diffusion." *Surface and Coatings Technology* 496 (2025): 131630. https://doi.org/10.1016/j.surfcoat.2024.131630.

[167]- M. Esmaily, J. E. Svensson, S. Fajardo, N. Birbilis, G. S. Frankel, S. Virtanen, R. Arrabal, S. Thomas, and L. G. Johansson. "Fundamentals and Advances in Magnesium Alloy Corrosion." *Progress in Materials Science* 89 (2017): 92–193. https://doi.org/10.1016/j.pmatsci.2017.04.011.

[168]- Y. Yürektürk, B. Şenyurt, C. Çeltik, B. Küçükelyas, and N. Akçamlı. "Si3N4 Reinforced Al-Si-Mg Matrix Composites: Powder Metallurgy Fabrication, PEO Coating and Characterization." *Applied Surface Science* 690 (2025): 162622. https://doi.org/10.1016/j.apsusc.2025.162622.

[169]- P. Fernández-López, S. A. Alves, A. López-Ortega, J. T. San José-Lombera, and R. Bayón. "High Performance Tribological Coatings on a Secondary Cast Al–Si Alloy Generated by

Plasma Electrolytic Oxidation." *Ceramics International* 47, no. 22 (2021): 31238–31250. https://doi.org/10.1016/j.ceramint.2021.07.300.

[170]- F. Zhang, Z. Liu, C. Pan, Y. Deng, D.-H. Xia, and B. Tribollet. "Effect of Si Network Continuity on the Localized Corrosion of AlSi10Mg Alloy Fabricated by Selective Laser Melting." *Corrosion Science* 257 (2025): 113336. https://doi.org/10.1016/j.corsci.2025.113336.

[171]- C. Liu, Q. Wang, X. Cao, L. Cha, R. Ye, and C. S. Ramachandran. "Significance of Plasma Electrolytic Oxidation Treatment on Corrosion and Sliding Wear Performances of Selective Laser Melted AlSi10Mg Alloy." *Materials Characterization* 181 (2021): 111479. https://doi.org/10.1016/j.matchar.2021.111479.

[172]- Y. Rao, Q. Wang, D. Oka, and C. S. Ramachandran. "On the PEO Treatment of Cold Sprayed 7075 Aluminum Alloy and Its Effects on Mechanical, Corrosion and Dry Sliding Wear Performances Thereof." *Surface and Coatings Technology* 383 (2020): 125271. https://doi.org/10.1016/j.surfcoat.2019.125271.

[173]- Y. Shi, H. Tan, L. Xie, M. Wang, and B. Zhou. "Effect of silicon content on the mechanical and corrosion behavior of additively manufactured aluminum–silicon alloys via selective laser melting." Anti-Corrosion Methods and Materials (2025). https://doi.org/10.1108/ACMM-06-2025-3302.